



저작자표시-비영리-변경금지 2.0 대한민국

이용자는 아래의 조건을 따르는 경우에 한하여 자유롭게

- 이 저작물을 복제, 배포, 전송, 전시, 공연 및 방송할 수 있습니다.

다음과 같은 조건을 따라야 합니다:



저작자표시. 귀하는 원저작자를 표시하여야 합니다.



비영리. 귀하는 이 저작물을 영리 목적으로 이용할 수 없습니다.



변경금지. 귀하는 이 저작물을 개작, 변형 또는 가공할 수 없습니다.

- 귀하는, 이 저작물의 재이용이나 배포의 경우, 이 저작물에 적용된 이용허락조건을 명확하게 나타내어야 합니다.
- 저작권자로부터 별도의 허가를 받으면 이러한 조건들은 적용되지 않습니다.

저작권법에 따른 이용자의 권리는 위의 내용에 의하여 영향을 받지 않습니다.

이것은 [이용허락규약\(Legal Code\)](#)을 이해하기 쉽게 요약한 것입니다.

[Disclaimer](#)

공학박사 학위논문

**Prediction of Failure with or without  
Strain Localization of Advanced High  
Strength Hot-rolled Steel Sheets**

초고강도 열연 강판의 변형률 집중 동반 유무에  
따른 파단 예측

2017년 2월

서울대학교 대학원

재료공학부

김 원 재

## **Abstract**

# **Prediction of Failure with or without Strain Localization of Advanced High Strength Hot-rolled Steel Sheets**

Wonjae Kim

Department of Materials Science and Engineering  
The Graduate School  
Seoul National University

Numerical analysis is commonly applied to predict failure and optimize forming process in the industrial sheet metal forming. In most of typical sheet forming processes at room temperature, the metal sheets fail to deform after strain localization in the thinning mode. This strain localization is a result of the boundary value problem of the force equilibrium condition, which is strongly affected by the following three mechanical properties: the hardening behavior, yield function and strain-rate sensitivity. However, some rather brittle metals fail without strain localization. It would be determined by the fracture criterion in principle, which is one of mechanical properties. Ultimately, failure is a result of competition between two sets of properties, the first set is the fracture criterion, which directly controls failure and the other consists of the three properties, which affect strain localization. The main object of this work is to predict failure of rather thick advanced high strength hot-rolled steel sheets depending on the existence of strain localization. As for the failure with strain localization, a new numerical procedure to evaluate the formability of rather thick advanced high strength hot-rolled steel sheets was developed in this work. The new procedure differs from the practice commonly applied for rather thin cold-rolled metal sheets with four main features: employing 3-D continuum elements, non-quadratic yield functions such as Yoshida and Hosford yield functions and hardening with its deterioration (or ultimate softening) beyond uniform deformation limit as well as directly monitoring strain

localization to determine failure without employing any forming limit criterion (unlike the common practice for cold-rolled sheets, which typically employs shell elements, Hill's quadratic yield function, extrapolated hardening and forming limit criterion). The characterization of material properties for the new procedure involves the simple tension, disk compression and hemispherical dome stretching tests. In case of failure without localization, to properly predict the formability, the strain rate effect and fracture criterion, which is dependent on stress triaxiality and strain rate, were considered. The stress triaxiality and strain rate dependent fracture criterion was characterized based on tensile tests of four different shape specimens to cover the wide range of deformation mode with various strain rates. From the experiments, the numerical and experimental punch force and displacement results were compared and the effective fracture strain was determined. For application and validation, advanced high strength hot-rolled steel sheets, HB780 and DP780 with the thickness of 2.9 mm for failure with strain localization and TWIP980 with the thickness of 3.1mm for failure without strain localization, were considered for the circular cup drawing test.

**Keywords: Advanced high strength hot-rolled steel sheets, Sheet formability, Non-quadratic yield function, Fracture criterion**

**Student Number: 2010-20585**

# Contents

1 Introduction .....	1
2 Theory .....	9
2.1 Yield function .....	9
2.1.1 Hill1948 yield function .....	9
2.1.2 Hosford yield function .....	10
2.1.3 Yoshida yield function.....	12
2.2 Fracture criterion .....	17
3 Material Characterization .....	18
3.1 Failure with strain localization .....	18
3.1.1 Simple tension test .....	18
3.1.2 Disk compression test.....	26
3.1.3 Yield function .....	28
3.1.4 Inverse calibration of hardening deterioration with the simple tension .....	34
3.1.5 Hemispherical dome stretching test .....	41
3.2 Failure without strain localization .....	59
3.2.1 Simple tension test .....	59
3.2.2 Strain rate sensitivity .....	66
3.2.3 Fracture test .....	72
3.2.4 Triaxiality and strain rate dependent fracture criterion .	75

4 Validation .....	93
5 Conclusions .....	124
Bibliography .....	127
Korean Abstract .....	131

## List of Tables

Table 1 Mechanical (engineering) properties of HB780 and DP780 ....	20
Table 2 Hardening behavior in the uniform deformation range with strain rate sensitivity.....	22
Table 3 Material parameters for three yield functions of HB780 and DP780.....	29
Table 4 The material parameters of the urethane pad .....	45
Table 5 Mechanical (engineering) properties of TWIP980.....	63
Table 6 Hardening behavior with strain rate sensitivity.....	63
Table 7 Material parameters for Hill 1948 yield function of TWIP980	65
Table 8 Hardening coefficients for the new developed empirical constitutive law.....	69
Table 9 Coefficients of the stress triaxiality dependent fracture criterion.....	92

## List of Figures

Figure 1 Hosford isotropic yield function (a) $1.0 \leq M \leq 2.0$ (b) $4.0 \leq M \leq \infty$ (c) $2.0 \leq M \leq 4.0$ .....	12
Figure 2 Drucker isotropic yield function: (a) $\pi$ -diagram (b) plane stress condition .....	14
Figure 3 Dimensions of the ASTM E8M standard specimen.....	19
Figure 4 Engineering stress–engineering strain curves: (a) HB780 (b) DP780.....	20
Figure 5 Comparison between hardening fitting curves and experiment results: (a) HB780 (b) DP780.....	23
Figure 6 Measured R-values: (a) HB780 (b) DP780.....	24
Figure 7 Strain rate sensitivity variation for four strain rates: (a) HB780 (b) DP780.....	26
Figure 8 Measured R-values in the balanced biaxial stress mode: (a) HB780 (b) DP780.....	27
Figure 9 Comparison of Hill1948, Hosford and Yoshida yield functions: (a) HB780 (b) DP780 .....	31
Figure 10 Variation of the normalized uni-axial yield stress with respect to the loading direction: (a) HB780 (b) DP780.....	32
Figure 11 Variation of the R-value with respect to the loading direction: (a) HB780 (b) DP780 .....	33
Figure 12 Comparison of hardening curves of HB780: (a) effective stress–effective plastic strain curves (b) engineering stress–engineering strain curves.....	36
Figure 13 Comparison of hardening curves of DP780: (a) effective stress–effective plastic strain curves (b) engineering stress–engineering strain curves.....	37
Figure 14 The critical and its neighboring elements for the simple tension test .....	38
Figure 15 Simple tension simulation results of HB780: (a) effective strain ratio between the critical and neighboring elements (b) strain-based FLD.....	39
Figure 16 Simple tension simulation results of DP780: (a) effective strain ratio between the critical and neighboring elements (b) strain-based FLD.....	40
Figure 17 Schematic view of the hemispherical dome stretching test with dimensions: (a) tool geometry (b) the spiral bead.....	42
Figure 18 Specimen geometry of the hemispherical dome stretching test .....	42

Figure 19 Measured forming limit diagram: (a) HB780 (b) DP780 .....	43
Figure 20 The critical and neighboring elements for the hemispherical dome stretching test of blanks with the width of (a) 25mm (b) 75mm (c) 130mm (d) 200mm .....	47
Figure 21 FLD simulation results of HB780 for the 25mm blank: (a) effective strain ratio between the critical and neighboring elements (b) strain-based FLD (c) force-displacement curve .....	48
Figure 22 FLD simulation results of DP780 for the 25mm blank: (a) effective strain ratio between the critical and neighboring elements (b) strain-based FLD (c) force-displacement curve .....	49
Figure 23 FLD simulation results of HB780 for the 75mm blank: (a) effective strain ratio between the critical and neighboring elements (b) strain-based FLD (c) force-displacement curve .....	50
Figure 24 FLD simulation results of DP780 for the 75mm blank: (a) effective strain ratio between the critical and neighboring elements (b) strain-based FLD (c) force-displacement curve .....	51
Figure 25 FLD simulation results of HB780 for the 130mm blank: (a) effective strain ratio between the critical and neighboring elements (b) strain-based FLD (c) force-displacement curve .....	52
Figure 26 FLD simulation results of DP780 for the 130mm blank: (a) effective strain ratio between the critical and neighboring elements (b) strain-based FLD (c) force-displacement curve .....	53
Figure 27 FLD simulation results of HB780 for the 200mm blank: (a) effective strain ratio between the critical and neighboring elements (b) strain-based FLD (c) force-displacement curve .....	54
Figure 28 FLD simulation results of DP780 for the 200mm blank: (a) effective strain ratio between the critical and neighboring elements (b) strain-based FLD (c) force-displacement curve .....	55
Figure 29 Engineering stress-engineering strain and true stress-true strain curves in the rolling direction (0°).....	60
Figure 30 Engineering stress-engineering strain and true stress-true strain curves in-between direction (45°).....	61
Figure 31 Engineering stress-engineering strain and true stress-true strain curves in transverse direction (90°).....	62
Figure 32 Comparison between hardening fitting curves and experiment results for TWIP980 .....	64
Figure 33 Measured R-values for TWIP980 .....	65
Figure 34 Comparison of Hill1948 and von Mises yield functions .....	66
Figure 35 Strain rate sensitivity variation for four strain rates for TWIP980 .....	67
Figure 36 Engineering stress-engineering strain with four tensile	

speeds in the rolling direction (0°) for TWIP980 .....	67
Figure 37 (a) The power law type hardening with various strain rates (b) comparison the experiment and simulation results .....	70
Figure 38 (a) The new developed hardening with various strain rates (b) comparison the experiment and simulation results .....	71
Figure 39 The dimension of specimens (unit: mm): (a) round notch I (b) round notch II (c) shear .....	73
Figure 40 The experiment punch force and displacement data for round notch I .....	73
Figure 41 The experiment punch force and displacement data for round notch II .....	74
Figure 42 The experiment punch force and displacement data for shear .....	74
Figure 43 Fractured specimens .....	75
Figure 44 Punch force and displacement for four fracture tests at 0.001 /sec: (a) simple tension (b) round notch I (c) round notch II (d) shear .....	77
Figure 45 Punch force and displacement for four fracture tests at 0.01 /sec: (a) simple tension (b) round notch I (c) round notch II (d) shear .....	79
Figure 46 Punch force and displacement for four fracture tests at 0.1 /sec: (a) simple tension (b) round notch I (c) round notch II (d) shear .....	81
Figure 47 Punch force and displacement for four fracture tests at 1.0 /sec: (a) simple tension (b) round notch I (c) round notch II (d) shear .....	83
Figure 48 Deformation histories of critical elements for the fracture tests simulation: (a) 0.001/sec (b) 0.01/sec (c) 0.1/sec (d) 1.0/sec .....	87
Figure 49 Stress triaxiality–dependent fracture criterion: (a) 0.001/sec (b) 0.01/sec (c) 0.1/sec (d) 1.0/sec.....	91
Figure 50 Stress triaxiality and strain dependent fracture criterion....	92
Figure 51 Schematic view of the cylindrical cup drawing test with dimensions .....	94
Figure 52 Circular cup drawing test results: (a) HB780 (b) DP780 .....	95
Figure 53 Circular cup drawing simulation results of HB780 with 102.5 mm diameter: (a) effective strain ratio between the critical and neighboring elements (b) strain-based FLD (c) force–displacement curve .....	99
Figure 54 Circular cup drawing simulation results of DP780 with 102.5 mm diameter: (a) effective strain ratio between the critical and	

neighboring elements (b) strain-based FLD (c) force-displacement curve .....	101
Figure 55 Circular cup drawing simulation results of HB780 with 105.0 mm diameter: (a) effective strain ratio between the critical and neighboring elements (b) strain-based FLD (c) force-displacement curve .....	103
Figure 56 Circular cup drawing simulation results of DP780 with 105.0 mm diameter: (a) effective strain ratio between the critical and neighboring elements (b) strain-based FLD (c) force-displacement curve .....	105
Figure 57 The experiment and simulation shapes of the successfully completed cups with 102.5 mm diameter: (a) HB780 (b) DP780.	106
Figure 58 Comparison of the experiment and simulation earing profiles: (a) HB780 (b) DP780 .....	107
Figure 59 The experiment and simulation shapes of the failed cups with 105.0 mm diameter: (a) HB780 (b) DP780.....	108
Figure 60 Circular cup drawing test results for TWIP980: (a) 20 mm/min (b) 100 mm/min (c) 170 mm/min .....	111
Figure 61 Simulation results for the 112.5 mm diameter with 20 mm/min punch speed: (a) Punch force and displacement (b) Effective strain and effective strain rate in log scale (c) Fracture criterion and deformation history.....	113
Figure 62 Simulation results for the 115.0 mm diameter with 20 mm/min punch speed: (a) Punch force and displacement (b) Effective strain and effective strain rate in log scale (c) Fracture criterion and deformation history.....	115
Figure 63 Simulation results for the 112.5 mm diameter with 100 mm/min punch speed: (a) Punch force and displacement (b) Effective strain and effective strain rate in log scale (c) Fracture criterion and deformation history.....	117
Figure 64 Simulation results for the 115.0 mm diameter with 100 mm/min punch speed: (a) Punch force and displacement (b) Effective strain and effective strain rate in log scale (c) Fracture criterion and deformation history.....	119
Figure 65 Simulation results for the 110.0 mm diameter with 170 mm/min punch speed: (a) Punch force and displacement (b) Effective strain and effective strain rate in log scale (c) Fracture criterion and deformation history.....	121
Figure 66 Simulation results for the 110.0 mm diameter with 170 mm/min punch speed: (a) Punch force and displacement (b) Effective strain and effective strain rate in log scale (c) Fracture	

criterion and deformation history..... 123

# Chapter 1. Introduction

In the manufacturing process of metal sheets, several rolling processes which are important processes to obtain the uniform thickness and reduce the thickness are conducted. The initial breakdown of ingots is generally conducted by hot-rolling at high temperature, which is usually above recrystallization temperature. The microstructure and mechanical property of the hot-rolled sheet are affected by heating and cooling temperatures (Ghosh et al., 2005; Kim, 2000; Zhao et al., 2002), cooling rates (Rodrigues et al., 2000) and the amount of plastic work (Jahazi and Egbali, 2000). For the application, the hot-rolled steel sheets are applied for structural members in construction as well as automotive parts such as wheels and disks. In recent years, the hot-rolled aluminum and magnesium sheets were used for automotive and advanced air-craft structural parts due to their lightweight advantage. Hot-rolled metal sheets may be further cold-rolled at room temperature to achieve sheets with reduced thickness and clean surface for automotive applications such as outer panels as well as home appliances. In general, through the cold-rolling process, the sheet is hardened and its grains are controlled to have favorable anisotropic property (Mateo et al., 2003; Zhang et al., 2010).

Since most of cold-rolled sheets are subjected to further forming operations to fabricate final products in automotive applications and home appliances, the proper evaluation of their performance during forming in terms of failure as well as springback and wrinkling is so important that various numerical methods to evaluate those

performances have been developed and applied to optimize industrial sheet metal forming processes. On the contrary, as for hot-rolled metal sheets, with their limited application for further forming operations, researches on their performance including the failure of advanced high strength hot-rolled steel sheets are rare and most of their researches have been mainly focused on metallurgical aspects. In a rare attempt to evaluate formability of hot-rolled sheets, Date and Padmanabhan (1992) measured the forming limit diagram for two hot-rolled low-carbon steel sheets used for low-pressure gas (LPG) cylinders and analyzed fracture surfaces using SEM. Also, Zhao et al. (2002) investigated the drawability of hot-rolled interstitial-free steels measuring average R-values but without addressing systematic procedures to evaluate formability in their forming in general.

Failure of sheets during forming operations would be determined by the fracture criterion in principle, which is one of mechanical properties. However, in most of typical sheet forming processes at room temperature such as stamping operations, either hot-rolled or cold-rolled sheets are subjected to more or less two dimensional plane stress condition with moderate bending (unlike the hole-expansion operation (Chung et al., 2011b) and processes involving sharp bending (Kim et al., 2011)) and fails to deform after strain localization in the thinning mode. This strain localization is a result of the boundary value problem of the force equilibrium condition, which is strongly affected by the following three mechanical properties: the hardening behavior, yield function and strain-rate sensitivity (Chung et al., 2014a; Chung et al., 2014b). Ultimately, failure is a result of competition between two sets of properties, the first set is the fracture criterion, which directly controls failure and the other consists of the

three properties, which affect strain localization. The objective of this paper is to predict the formability of rather thick advanced high strength hot-rolled steel sheets depending on the existence of the strain localization (failure with or without strain localization).

For most of automotive sheets including low carbon and advanced high strength steel sheets, fracture limit is so large compared to the deformation limit set by the strain localization that they fail by strain localization. For such a case, measuring the fracture criterion becomes so much involved and might be less important, while properly measuring the three properties becomes more vital for proper evaluation of failure. Considering that most of automotive sheets fail by strain localization, four main features were introduced in the new procedure to properly address strain localization, referring to the procedure developed by (Chung et al., 2014b): employing 3-D continuum elements with fine meshes, non-quadratic yield functions such as Yoshida and Hosford yield functions and hardening with its deterioration (or ultimate softening) beyond uniform deformation limit as well as directly monitoring strain localization to determine failure without employing any forming limit criterion. These features differ from those of the practice commonly applied for thin cold-rolled sheets, which typically employs shell elements, Hill's quadratic yield function, extrapolated hardening and forming limit criterion.

For typical sheet metal forming operations such as stamping processes, either hot-rolled or cold-rolled sheets deform more or less under the plane stress mode. However, the shell element promotes premature (too early) strain localization for rather thick hot-

rolled sheets since the shell element lacks the geometric continuity constraint for inhomogeneous thickness distributions unlike the 3-D continuum element. Therefore, 3-D continuum elements were applied with fine meshes here. Coarse meshes delay strain localization. The promotion and delay of the strain localization by the shell element and coarse meshes were briefly reviewed in this work.

Regarding the mechanical properties, three properties mentioned above strongly affect strain localization. As for the hardening behavior, as its stiffness (typically noted as the  $n$ -value) is subsided, strain localization is promoted. The standard procedure to characterize the hardening behavior is to perform curve fitting only up to the UTS (ultimate tensile strength) point as the uniform deformation limit in the simple tension test and then extrapolate it beyond the UTS point. Some performed the bulge test to obtain hardening, which has about twice larger uniform deformation range compared to the simple tension test (Atkinson, 1997; Gutscher et al., 2004; Young et al., 1981). However, micro-voids develop in sheets in general before failure so that hardening may deteriorate (or soften) after UTS, as captured by the GTN fracture (Tvergaard and Needleman, 1984) and Lemaitre damage models (Lemaitre, 1992). As a way to simplify those sophisticated models, hardening deterioration after UTS was characterized in this work, employing the inverse numerical method for the simple tension test under the prevalent assumption of the isotropic hardening. Along this effort, the strain rate sensitivity was also characterized with the simple tension test since it significantly subdues strain localization.

Yield function shapes significantly affect strain localization. As the yield function

shape is more bulged out in the plane strain mode (between the simple tension and the balanced biaxial deformation modes under the plane stress condition), as the shape evolves from such as that of the Tresca (Tresca, 1864) to that of the von Mises yield function (Von-Mises, 1913), strain localization delays in the biaxial stretching mode. Therefore, a proper choice of the yield function is important to properly simulate strain localization in the biaxial stretching mode. Among several yield functions for 3-D continuum elements, Hosford isotropic (Hosford, 1972) and Yoshida anisotropic (Yoshida et al., 2013) yield functions were employed here. The Hosford yield function has one particular material parameter, which determines the shape of yield surface and directly affects the strain localization in the biaxial stretching mode. Among many anisotropic yield functions for 3-D continuum elements, the Yoshida yield function was originally developed particularly for its convenient application for sheet forming; therefore, it has a fewer number of anisotropic coefficients compared to others. Besides, it has one particular material parameter, which also directly affects the strain localization in the biaxial stretching mode as the one for the Hosford function does. Hill's anisotropic yield function (Hill, 1948) was also employed here for comparison purposes. Those particular material parameters of the Hosford and Yoshida yield functions affecting strain localization were characterized considering their performance in predicting strain localization in the hemispherical dome stretching test, which is routinely utilized to measure forming limit diagrams in the biaxial stretching mode. In addition to the hemispherical dome stretching test, the disk compression test was conducted to obtain R-value in the balanced biaxial stress mode. In all, the three material properties important for strain localization were characterized utilizing the simple tension, disk compression and hemispherical dome stretching tests in this work.

As for the last of the four features, the forming limit diagram (FLD) is commonly utilized to determine failure by strain localization. Note that FLD is applied to the critical element which fails in the common practice, assuming that FLD is a material property replacing the fracture criterion for failure by strain localization. However, the FLD data, when experimentally measured, is the deformation of a small group of material elements (or a grid) which neighbors and deforms together with the critical element during forming but then survives when the critical one fails by severe strain localization in the end. Therefore, applying the FLD for the critical element in the numerical procedure may lead to premature failure by strain localization, which was also briefly reviewed. In this work, instead of utilizing FLD, failure by strain localization was determined by directly monitoring strain localization, for which relative deformation in terms of the effective strain at the critical element and its small group of neighbors (with the size of one grid used for the FLD experiment) was traced throughout forming. This new feature is virtually the numerical mimic of the FLD test.

Failure by fracture without strain localization is the case of Hot-rolled TWIP (twinning induced plasticity) steel sheet, for which the strain localization limit is significantly larger than those of typical automotive steel sheets with its stiff hardening behavior associated with twinning mechanism for plastic deformation. Most of researches have been mainly focused on the modeling of microstructure or evolution of texture (Allain et al., 2004; Bouaziz and Guelton, 2001; Grässel et al., 2000). In a rare attempt to evaluate formability of TWIP sheet, (Chung et al., 2011b) had researched the mechanical properties and formability of cold-rolled TWIP sheet. In this work, the

predict of failure of hot-rolled TWIP steel sheets with rather thick thickness was conducted considering the strain rate effect and the fracture criteria, which is dependent on the triaxiality and strain rate, was developed.

As for the strain rate sensitivity in hardening behavior, there are numerous constitutive equations (Hosford and Caddell, 1983; Sung et al., 2010; Wagoner, 1981). Among them, the power law type with the average  $m$ -value (Hosford and Caddell, 1983) to represent the strain rate sensitivity is commonly utilized due to its simplicity. The strain rate sensitivity is measured by conducting the simple tension tests with various tensile speeds or strain rate jump tests. Based on the experimentally obtained hardening data, the strain rate sensitivity (the average  $m$ -value) is calculated. Unlike most of steel sheets, TWIP sheet shows the negative average  $m$ -value (Chung et al., 2011a). Also, in that work, the numerical simulation was implemented without considering strain rate sensitivity. In this work, a new constitutive equation for TWIP considering strain rate effect was developed and the numerical analysis with hardening including strain rate sensitivity was conducted.

For the fracture model, numerous fracture models have been researched on ductile fracture model in terms of nucleation, growth and coalescence of micro-voids such as the Gurson (Gurson, 1977) and GTN models (Tvergaard and Needleman, 1984) as well as the damage model (Lemaitre, 1992). Moreover, more sophisticated fracture criteria based on stress triaxiality and Lode angle was proposed by extending the modified Mohr-Coulomb stress based fracture criterion without explicit expression of the softening behavior (Bai and Wierzbicki, 2008, 2009; Bao and Wierzbicki, 2004).

Recently, (Chung et al., 2011b) has developed an inverse calibration method to describe the hardening deterioration and the triaxiality-dependent fracture criterion was developed. In this work, based on the procedure developed by (Chung et al., 2011b), triaxiality and strain rate dependent fracture criterion was characterized.

For application and validation, the numerical procedure developed here for failure with strain localization of hot-rolled sheets, two advanced high strength hot-rolled steel sheets, HB780 and DP780 with the thickness of 2.9 mm, were considered. The main mechanical properties were characterized based on the simple tension, disk compression and hemispherical dome stretching tests in along with a brief review of Hill, Hosford and Yoshida yield functions. The procedure was validated for the circular cup drawing test, in which the performances of shell elements with coarse meshes and directly employing the FLD criterion to determine failure were also briefly examined. For the failure without strain localization, to describe the hardening behavior, the new constitutive equation as a function of strain, strain rate was developed and implemented in the numerical simulation utilizing 3D continuum elements based on simple tension tests with various strain rates. Also, as for the fracture criterion, triaxiality and strain rate dependent fracture criterion was characterized based on tensile tests with various strain rates of four different shape specimens to cover the wide range of deformation mode. For validation of the characterized fracture criterion, the circular cup drawing tests with different punch speeds were conducted.

## Chapter 2. Theory

### 2.1 Yield function

Three yield functions, the quadratic anisotropic Hill1948, non-quadratic isotropic Hosford and non-quadratic anisotropic Yoshida yield functions, were briefly reviewed here.

#### 2.1.1 Hill1948 yield function: Quadratic anisotropic yield function

The quadratic anisotropic yield function proposed by Hill (1948) is defined by

$$F(\sigma_{yy} - \sigma_{zz})^2 + G(\sigma_{zz} - \sigma_{xx})^2 + H(\sigma_{xx} - \sigma_{yy})^2 + 2L\sigma_{yz}^2 + 2M\sigma_{zx}^2 + 2N\sigma_{xy}^2 = \bar{\sigma}^2 \quad (2.1.1)$$

with

$$d\bar{\varepsilon}^2 = (G+H) \left[ \frac{Fd\varepsilon_{xx}^2 + Gd\varepsilon_{yy}^2 + Hd\varepsilon_{zz}^2}{FG+GH+HF} + \frac{2d\varepsilon_{yz}^2}{L} + \frac{2d\varepsilon_{zx}^2}{M} + \frac{2d\varepsilon_{xy}^2}{N} \right] \quad (2.1.2)$$

where x, y and z are rolling, transverse and thickness directions. Here, F, G, H, L, M and N are anisotropic coefficients, which were calibrated using three R-values ( $R_0, R_{45}, R_{90}$ ) with assuming that  $L=M=1.5$ :

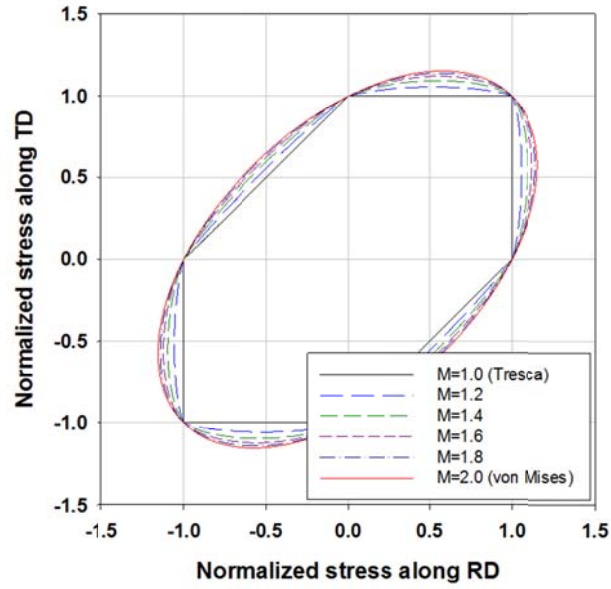
$$F = \frac{R_0}{R_{90}(1+R_0)}, G = \frac{1}{1+R_0}, H = \frac{R_0}{1+R_0}, N = \frac{(R_0 + R_{90})(2R_{45} + 1)}{2R_{90}(1+R_0)} \quad (2.1.3)$$

### 2.1.2 Hosford yield function: Non-quadratic isotropic yield function

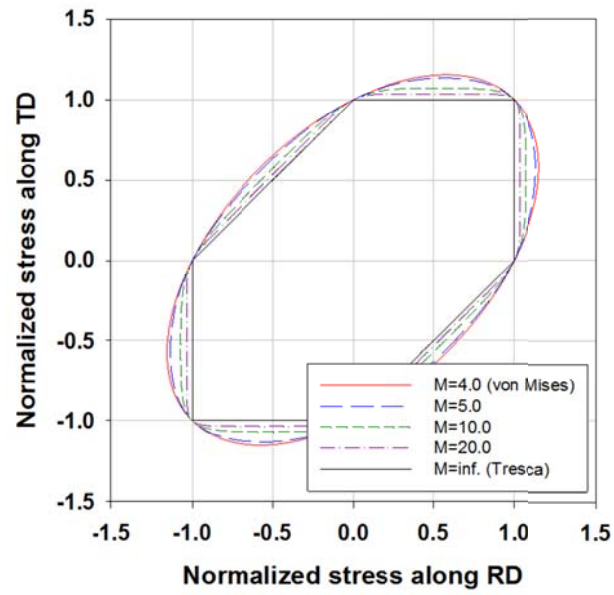
The non-quadratic isotropic yield function proposed by Hosford (1972) is defined by

$$|\sigma_1 - \sigma_2|^M + |\sigma_3 - \sigma_1|^M + |\sigma_2 - \sigma_3|^M = 2\bar{\sigma}^M \quad (2.1.4)$$

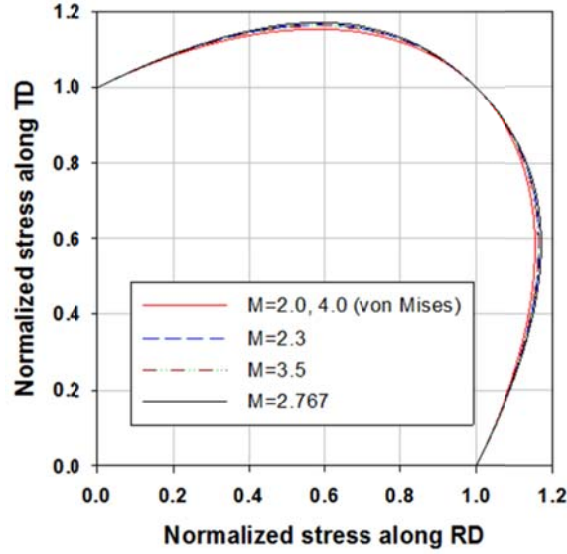
where  $\sigma_1$ ,  $\sigma_2$  and  $\sigma_3$  are the principal stresses and M is a material-dependent exponent which determines the yield function shape. Unlike the Hill1948 yield function, the Hosford yield function does not have an explicit analytical expression for its conjugate effective strain increment. For  $M \geq 1.0$ , the yield surface is convex as shown in Figure 1. In particular, as the M value increases from 1.0 to 2.0 or decreases from  $\infty$  to 4.0, the yield surface transforms from the Tresca to von Mises yield function as shown in Figure 1 (a) and (b). Between M =2.0 and 4.0, the yield function is bulged out beyond the shape of the von Mises yield function as the M values increases from 2.0 to 2.767 and then decreases back to 4.0 as shown in Figure 1 (c).



(a)



(b)



(c)

Figure 1 Hosford isotropic yield function (a)  $1.0 \leq M \leq 2.0$  (b)  $4.0 \leq M \leq \infty$  (c)  $2.0 \leq M \leq 4.0$

### 2.1.3 Yoshida yield function: Non-quadratic anisotropic yield function

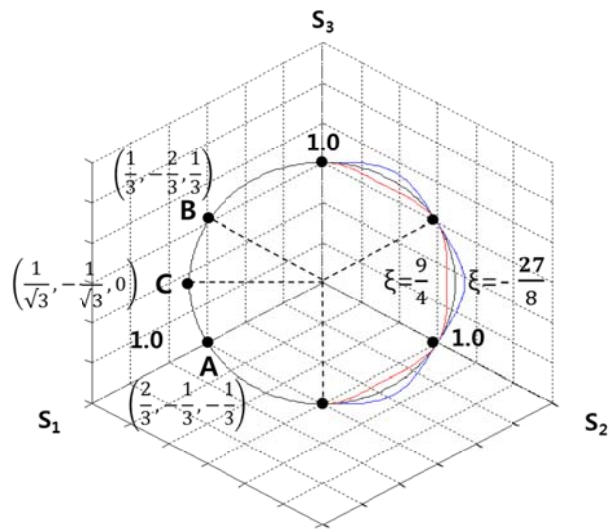
The non-quadratic polynomial anisotropic yield function proposed by Yoshida et al. (2013) is the extended version of the Cazacu/Barlat anisotropic yield function (Cazacu and Barlat, 2001) and the Drucker isotropic yield function (Drucker, 1949). Therefore, the main feature of the Yoshida yield function is reviewed here, considering the following the Drucker yield function:

$$J_2^3 - \xi J_3^2 = \frac{1}{3^6} (27 - 4\xi) \bar{\sigma}^6 \quad (2.1.5)$$

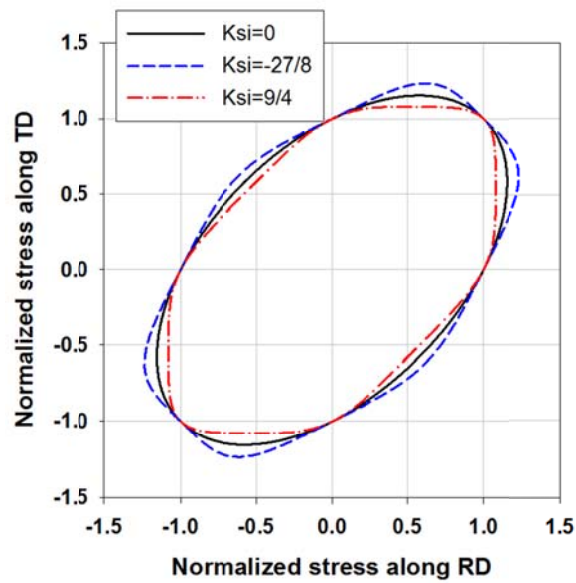
where  $J_2$  and  $J_3$  are the second and third invariants of the deviatoric stress tensor, s:

$J_2 = \frac{1}{2}(s_{ij}s_{ij})$  and  $J_3 = \frac{1}{3}(s_{ij}s_{jk}s_{ki}) (= s_1s_2s_3)$  (multiplication of three principal deviatoric stresses). Note that  $J_2^3 = \frac{1}{3^3}\bar{\sigma}^6$  is the von Mises yield function (with  $\xi = 0.0$ ) as shown in the  $\pi$ -diagram, (a) (normalized by  $\bar{\sigma}$ ).

The second term is the modifier of the von Mises yield function; i.e.,  $J_3^2 = \frac{4}{3^6}\bar{\sigma}^6$  is commonly valid for the simple tension and balanced biaxial stress states, which were marked with six solid dots along with A and B, respectively, in the  $\pi$ -diagram; therefore, these six states stay on the von Mises yield function regardless of the  $\xi$  value. Now, note that the value of  $J_3^2$  gradually and symmetrically decreases to zero as the stress states moves from A and B to C, the pure shear stress state (plane strain mode). Therefore, the shape of the yield function flattens between A and B as the positive  $\xi$  increases and C moves inward, while it bulges out as the negative  $\xi$  decreases and C moves outward. The yield function shape remains convex for  $-\frac{27}{8} \leq \xi \leq \frac{9}{4}$  and the shape between A and B, which is symmetric with respect to C, is repeated six times for the rest in the  $\pi$ -diagram as shown in Figure 2 (a). The yield function shape under the plane stress condition normalized by  $\bar{\sigma}$  is shown in Figure 2 (b), which demonstrates that the effect of the value on the Drucker yield function shape is similar with that of the M value on the Hosford yield function (therefore, both are dubbed here as the non-quadratic yield function parameters).



(a)



(b)

Figure 2 Drucker isotropic yield function: (a)  $\pi$ -diagram (b) plane stress condition

The Yoshida yield function is defined, as

$$f(s) = \frac{1}{n} \sum_{m=1}^n \phi(\tilde{s}^{(m)}) = \frac{27}{n} \sum_{m=1}^n \left\{ \left( \tilde{J}_2^{(m)} \right)^3 - \xi_m \left( \tilde{J}_3^{(m)} \right)^2 \right\} = \bar{\sigma}^6 \quad (2.1.6)$$

where  $\xi_m$  is the (non-quadratic) parameter for the shape of the yield function and  $\tilde{J}_2, \tilde{J}_3$  are the second and third invariants of the linearly transformed deviatoric stress tensor,  $\tilde{s}$ ; i.e.,

$$\tilde{J}_2 = \frac{1}{2} \tilde{s}_{ij} \tilde{s}_{ij}, \quad \tilde{J}_3 = \frac{1}{3} \tilde{s}_{ij} \tilde{s}_{jk} \tilde{s}_{ki} \quad (= \tilde{s}_1 \tilde{s}_2 \tilde{s}_3) \quad (2.1.7)$$

For the linear transformation,  $\tilde{s} = \mathbf{L}\boldsymbol{\sigma}$ , where  $\mathbf{L}$  is represented with anisotropic coefficients as

$$\mathbf{L} = \frac{1}{3} \begin{bmatrix} b_m + c_m & -c_m & -b_m & 0 & 0 & 0 \\ -c_m & c_m + a_m & -a_m & 0 & 0 & 0 \\ -b_m & -a_m & a_m + b_m & 0 & 0 & 0 \\ 0 & 0 & 0 & 3g_m & 0 & 0 \\ 0 & 0 & 0 & 0 & 3h_m & 0 \\ 0 & 0 & 0 & 0 & 0 & 3k_m \end{bmatrix} \quad (2.1.8)$$

The Yoshida yield function is expressed explicitly in terms of the Cauchy stress:

$$\begin{aligned}
f = & C_1(\sigma_{xx} - \sigma_{zz})^6 - 3C_2(\sigma_{xx} - \sigma_{zz})^5(\sigma_{yy} - \sigma_{zz}) + 6C_3(\sigma_{xx} - \sigma_{zz})^4(\sigma_{yy} - \sigma_{zz})^2 \\
& - 7C_4(\sigma_{xx} - \sigma_{zz})^3(\sigma_{yy} - \sigma_{zz})^3 + 6C_5(\sigma_{xx} - \sigma_{zz})^2(\sigma_{yy} - \sigma_{zz})^4 \\
& - 3C_6(\sigma_{xx} - \sigma_{zz})(\sigma_{yy} - \sigma_{zz})^5 + C_7(\sigma_{yy} - \sigma_{zz})^6 + 9\{C_8(\sigma_{xx} - \sigma_{zz})^4 \\
& - 2C_9(\sigma_{xx} - \sigma_{zz})^3(\sigma_{yy} - \sigma_{zz}) + 3C_{10}(\sigma_{xx} - \sigma_{zz})^2(\sigma_{yy} - \sigma_{zz})^2 - 2C_{11}(\sigma_{xx} - \sigma_{zz}) \\
& (\sigma_{yy} - \sigma_{zz})^3 + C_{12}(\sigma_{yy} - \sigma_{zz})^4\}\sigma_{xy}^2 + 27\{C_{13}(\sigma_{xx} - \sigma_{zz})^2 - C_{14}(\sigma_{xx} - \sigma_{zz})(\sigma_{yy} - \sigma_{zz}) \\
& + C_{15}(\sigma_{yy} - \sigma_{zz})^2\}\sigma_{xy}^4 + 27C_{16}(\sigma_{xy}^6 + \sigma_{yz}^6 + \sigma_{xz}^6) = \bar{\sigma}^6 = C_1\bar{\sigma}^6
\end{aligned} \tag{2.1.9}$$

where  $C_1 \sim C_{16}$  are material parameters, which are the function of anisotropic coefficients,  $a_m$ ,  $b_m$ ,  $c_m$  and  $g_m$  as well as  $\xi_m$ . Note that  $C_1 = 1.0$ . In (2.1.9), it was assumed that  $g_m = h_m = k_m$  and the terms involving  $\sigma_{yz}$  and  $\sigma_{zx}$  were ignored except the last term on the left hand side, for its convenient application for sheet forming. When  $n = 1$ , the Yoshida yield function becomes the Cazacu/Barlat yield function, the anisotropic version of (2.1.5), while, when anisotropic coefficients are equal to 1.0 and  $\xi_m$  is zero, it reduces to the von Mises yield function. Since the linear transformation for anisotropy does not affect convexity, the convexity condition for the Yoshida yield function remains the same with that of the Drucker.

## 2.2 Fracture criteria

### 2.2.1 Stress triaxiality-dependent fracture criterion

In this work, based on the effective fracture strain,  $\bar{\varepsilon}_F (= \int d\bar{\varepsilon})$ , the fracture criterion was characterized.

$$\omega = \int d\omega = \int \frac{d\bar{\varepsilon}}{\bar{\varepsilon}_F(\eta)} \quad (2.1.10)$$

where  $\omega$  is the damage parameter and  $\eta = (\sigma_1 + \sigma_2 + \sigma_3) / 3\bar{\sigma}$  is the stress triaxiality with three principal stresses. When  $\omega$  is 1.0, the moment of the macro crack occur for fracture. Here,  $\bar{\varepsilon}_F$  is the accumulative effective fracture strain under the uniform stress triaxiality condition. Based on (2.1.10), the deformation path change (or triaxiality) can be properly accounted. The apparent effective fracture strain,  $\bar{\varepsilon}_F^*$ , under the non-uniform stress triaxiality condition can be calculated by considering the deformation path change effect ((Chung et al., 2011b) for details); i.e.

$$\bar{\varepsilon}_F^*(\tilde{\eta}) = \bar{\varepsilon}_F(\tilde{\eta}) + \left( \int d\bar{\varepsilon} - \omega \cdot \bar{\varepsilon}_F(\tilde{\eta}) \right) \quad (2.1.11)$$

where  $\bar{\varepsilon}_F(\tilde{\eta})$  and  $\bar{\varepsilon}_F^*(\tilde{\eta})$  are current values at  $\eta = \tilde{\eta}$ , while two terms in a parenthesis are the accumulative quantities based on the previous path change history.

Under uniform deformation path,  $\bar{\varepsilon}_F^*(\tilde{\eta}) = \bar{\varepsilon}_F(\tilde{\eta})$ .

## **Chapter 3. Material characterization**

### **3.1 Failure with strain localization**

As for failure with strain localization, two kinds of advanced high strength hot-rolled steel sheets produced by POSCO, HB780 (hyper burring) and DP780 (dual phase) steel sheets with the thickness of 2.9 mm, were considered. Their main mechanical properties, the hardening with deterioration, strain rate sensitivity and the non-quadratic yield function parameter, were characterized based on the simple tension, disk compression and hemispherical dome stretching tests as summarized here. Moreover, the numerical analysis for the prediction of failure with strain localization was conducted based on the experimental results. (Kim et al., 2016)

#### **3.1.1 Simple tension test (for hardening behavior below UTS, R-values and strain rate sensitivity)**

The simple tension tests were conducted utilizing the ASTM E8M standard specimen prepared by the wire cutting process along the rolling direction as shown in Figure 3. As for material anisotropy, simple tension tests were conducted along the rolling ( $0^\circ$ ), transverse ( $90^\circ$ ) and in-between ( $45^\circ$ ) directions. Tensile speed was 0.05 mm/s, which corresponds to the strain rate of approximately 0.001 /s when deformation is uniform within the gauge length of 50.0 mm. The particular strain rate was considered as the reference strain rate to describe the strain rate sensitivity. Figure 4 shows typical engineering stress-engineering strain curves measured for three directions. The

measured mechanical properties of HB780 and DP780, averaged for three tests repeated per each direction, were summarized in Table 1.

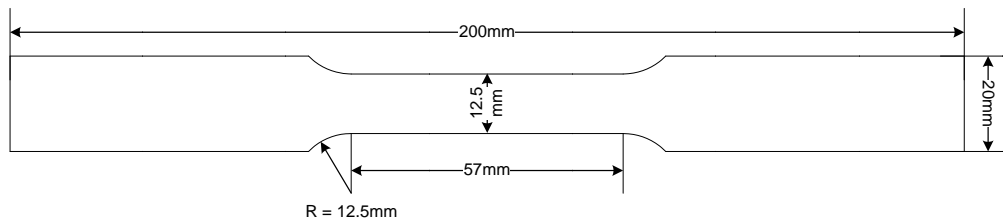
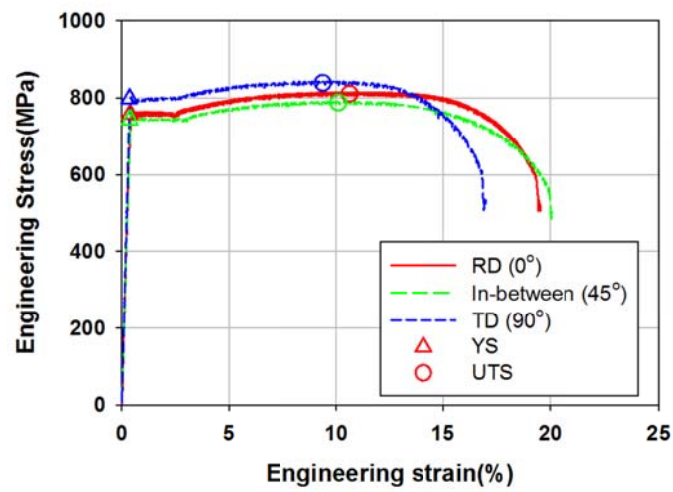
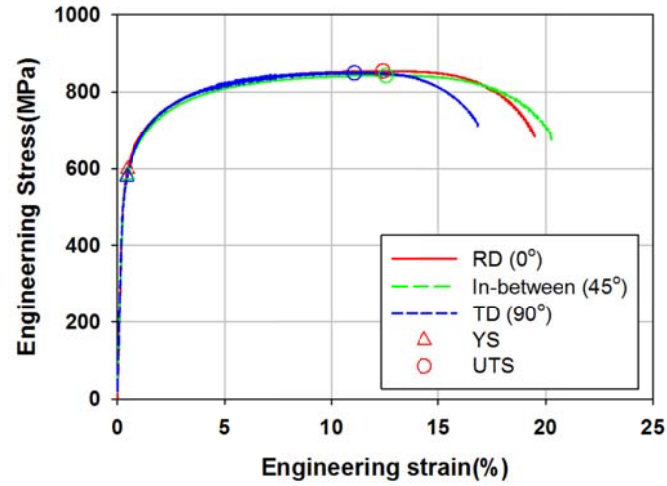


Figure 3 Dimensions of the ASTM E8M standard specimen



(a)



(b)

Figure 4 Engineering stress-engineering strain curves: (a) HB780 (b) DP780

Table 1 Mechanical (engineering) properties of HB780 and DP780

Direction	E (GPa)	YS (MPa)	UTS (MPa)	Elongation (%)		R-value	
				Uniform	Total		
HB780	RD (0°)	196.4	757.4	815.3	10.89	19.46	0.7255
	In-between (45°)	190.5	743.4	787.3	10.10	19.58	1.2171
	TD (90°)	212.3	798.1	840.9	9.470	17.31	0.7927
DP780	RD (0°)	203.5	596.0	853.2	12.30	19.54	0.6426
	In-between (45°)	198.4	576.0	836.2	12.45	20.36	1.0104
	TD (90°)	209.5	575.1	848.3	11.13	16.84	0.6963

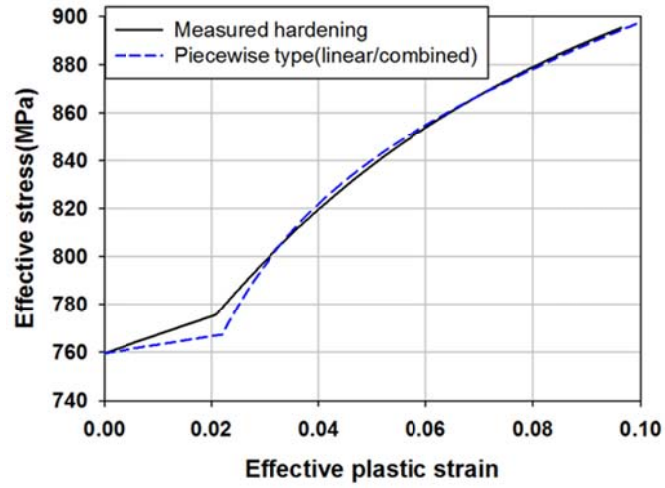
As for the hardening behavior, simple tension test data along the rolling direction was considered as the reference state for the isotropic hardening law. For HB780, a slight yield point phenomenon, which may have the upper and lower bounds of yield stress, was shown in the engineering stress-engineering strain curve without obvious Portevin-Le Chatelier bands. To describe the hardening behavior in the uniform deformation range below UTS, the piecewise type (the linear type + the combined type) fitting law was applied by utilizing the least square method and resulting fitting constants were listed in Table 2. As for DP780, the hardening behavior below UTS was fit to the combined Voce-Swift hardening type law, utilizing the least square method, and resulting fitting constants were listed in Table 2. The hardening fitting curves well matched with the experiments for both samples as shown in Figure 5 up to UTS.

To measure the R-value (the ratio of the transverse strain increment with respect to the thickness strain increment in simple tension), the transverse strain was measured using the strain gage attached perpendicular to the tensile direction in the simple tension test and the thickness strain was calculated assuming the constant volume condition. Measured R-values of the three directions were plotted in Figure 6 and summarized in Table 1.

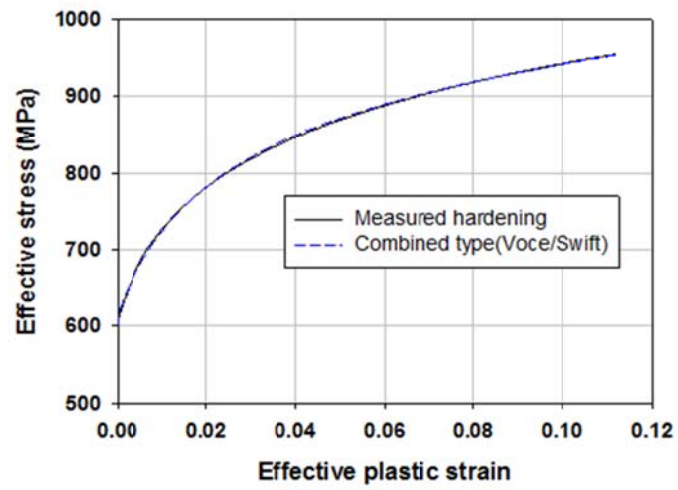
Table 2 Hardening behavior in the uniform deformation range with strain rate sensitivity

		$\text{If } \bar{\varepsilon} \leq 0.0215: \bar{\sigma} = (A_{HB}\bar{\varepsilon} + B_{HB}) \left( \frac{\dot{\bar{\varepsilon}}}{\dot{\bar{\varepsilon}}_o} \right)^{m_{HB}}$					
Piecewise type:		$\text{otherwise: } \bar{\sigma} = [C_{HB}(\bar{\varepsilon} + \bar{\varepsilon}_{0,HB})^{D_{HB}} + E_{HB}(1 - e^{-F_{HB}\bar{\varepsilon}})] \left( \frac{\dot{\bar{\varepsilon}}}{\dot{\bar{\varepsilon}}_o} \right)^{m_{HB}}$					
		$A_{HB}$	$B_{HB}$	$m_{HB}$	$\dot{\bar{\varepsilon}}_o$		
HB780	(MPa)	(MPa)					
		356.4	759.6	0.0048	0.001		
		$C_{HB}$	$D_{HB}$	$E_{HB}$	$F_{HB}$	$\bar{\varepsilon}_{0,HB}$	
		(MPa)		(MPa)			
	1038.8	0.222	193.8	68.2	0.0739		
		$\text{Combined type: } \bar{\sigma} = [A_{DP}(\bar{\varepsilon} + \bar{\varepsilon}_{0,DP})^{B_{DP}} + C_{DP}(1 - e^{-D_{DP}\bar{\varepsilon}})] \left( \frac{\dot{\bar{\varepsilon}}}{\dot{\bar{\varepsilon}}_o} \right)^{m_{DP}}$					
DP780	$A_{DP}$	$B_{DP}$	$C_{DP}$	$D_{DP}$	$\bar{\varepsilon}_{0,DP}$	$m_{DP}$	$\dot{\bar{\varepsilon}}_o$
	(MPa)		(MPa)				
	1167.1	0.125	61.9	60.6	$6.07 \times 10^{-3}$	0.0045	0.001

( $\bar{\sigma}$ : the effective stress,  $\dot{\bar{\varepsilon}}$ : the effective plastic strain rate,  $\bar{\varepsilon} = \int \dot{\bar{\varepsilon}} d\tau$  where  $\tau$  is time)

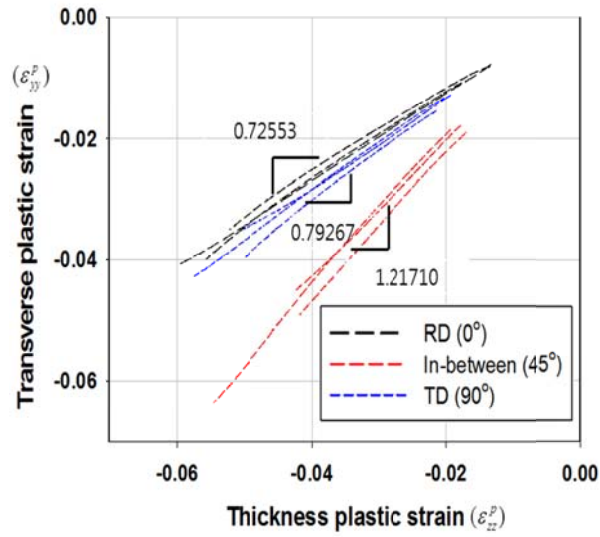


(a)

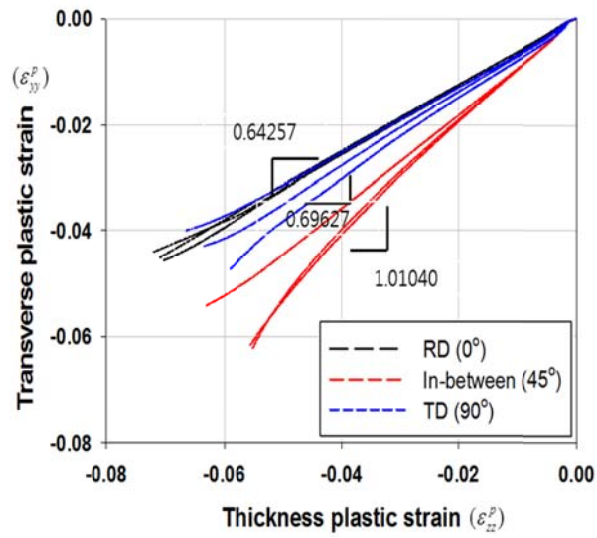


(b)

Figure 5 Comparison between hardening fitting curves and experiment results: (a) HB780 (b) DP780



(a)



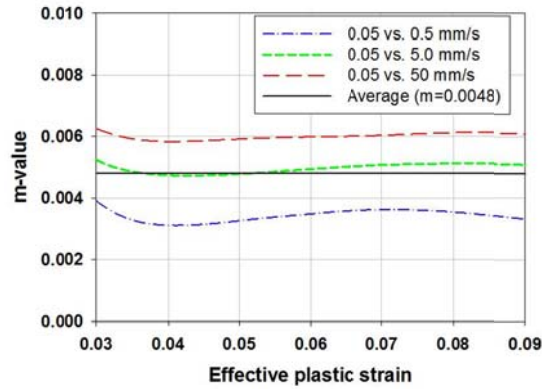
(b)

Figure 6 Measured R-values: (a) HB780 (b) DP780

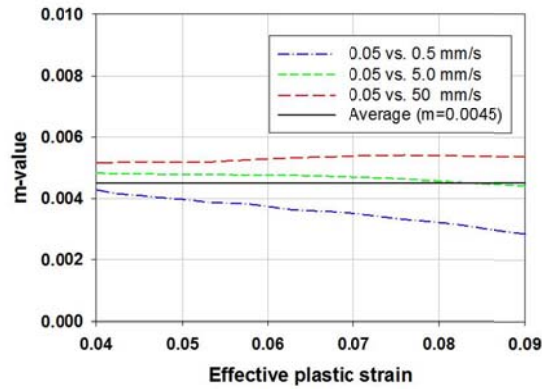
As for strain rate sensitivity, the strain rate sensitivity exponent (the m-value) of the power law type was measured through the simple tension test along the rolling direction with four tensile speeds, 0.05, 0.5, 5.0 and 50.0 mm/s, which were approximately assumed to be strain rates of 0.001, 0.01, 0.1 and 1.0 /s, respectively, considering the 50.0 mm gage length. Based on measured hardening curves, the strain rate sensitivity exponent was calculated as

$$m(\bar{\varepsilon}, \dot{\bar{\varepsilon}}) = \frac{\ln\left(\frac{\bar{\sigma}(\bar{\varepsilon}, \dot{\bar{\varepsilon}})}{\bar{\sigma}(\bar{\varepsilon}, \dot{\bar{\varepsilon}}_0 = 0.001)}\right)}{\ln\left(\frac{\dot{\bar{\varepsilon}}}{\dot{\bar{\varepsilon}}_0(\bar{\varepsilon}) = 0.001}\right)} \quad (3.1.1)$$

where  $\bar{\sigma}$  and  $\dot{\bar{\varepsilon}}$  are the effective stress and the effective plastic strain rate. Strain rate sensitivity variations for the four strain rates were plotted in Figure 7 and the average strain rate sensitivity exponents of two samples, which were used for computation in this work, were listed in Table 2.



(a)

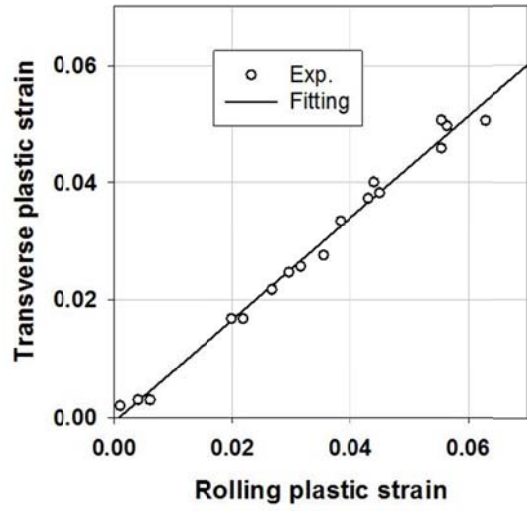


(b)

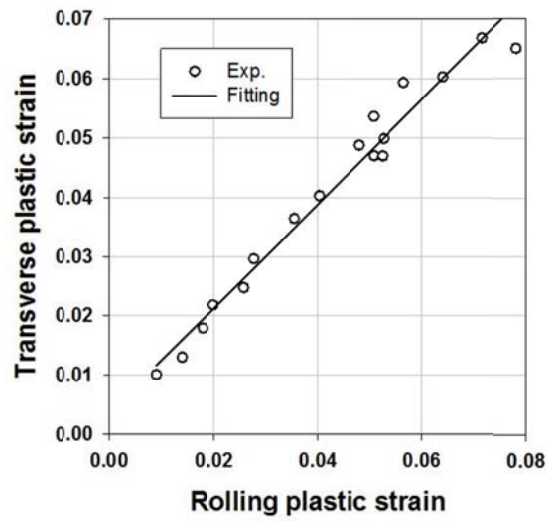
Figure 7 Strain rate sensitivity variation for four strain rates: (a) HB780 (b) DP780

### 3.1.2 Disk compression test

Disk compression tests (Xu L., 2008) were conducted to obtain R-value in the balanced biaxial stress mode,  $R_b$ , which is the ratio of the transverse strain increment with respect to the rolling direction strain increment. The disk compression test specimens were prepared by wire cutting with the diameter of 10 mm. Compression tests were conducted with loading from 75 to 90 kN with the increment of 2.5 kN. After compression test, diameters in the rolling direction and transverse direction were measured. The results were shown in Figure 8 and the measured R-values in the balanced biaxial stress mode for HB780 and DP780 were 0.8673 and 0.8796, respectively.



(a)



(b)

Figure 8 Measured R-values in the balanced biaxial stress mode: (a) HB780 (b) DP780

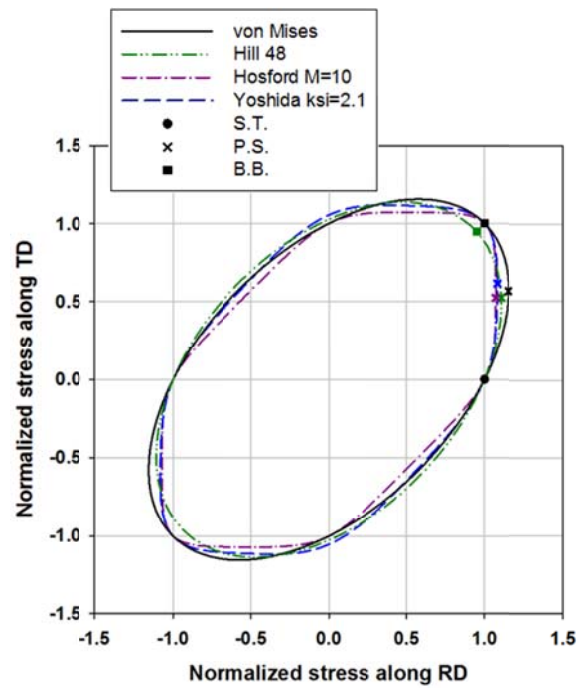
### 3.1.3 Yield function

Three yield functions, the quadratic anisotropic Hill1948, non-quadratic isotropic Hosford and non-quadratic anisotropic Yoshida yield functions, were calibrated. (Kim et al., 2016) Yield function shape significantly affects strain localization: As the yield function shape is more bulged out in the plane strain mode (between the simple tension and the balanced biaxial deformation modes), as the shape evolves from that of the Tresca to that of the von Mises yield function, strain localization delays (Chung et al., 2014a). For Hill1948, F, G, H, L, M and N which are anisotropic coefficients as listed in were calibrated using three R-values ( $R_0, R_{45}, R_{90}$ ) with assuming that  $L=M=1.5$ . As for the Hosford yield function, the M value was determined considering its performance in predicting strain localization in the hemispherical dome stretching test. The M-values for HB780 and DP780 were 10.0 and 6.0, respectively, as listed in Table 3, which will be further detailed later. With respect to the Yoshida yield function by considering its effect on strain localization in the biaxial stretching mode, the  $\xi_m$  value was determined based on its performance in predicting strain localization in the hemispherical dome stretching test as done for the M value of the Hosford yield function, while assuming that  $\xi_{m=1} = \xi_{m=2}$  for simplicity. The  $\xi_m$  values became 2.1 and -1.0 for HB780 and DP780, respectively, as listed in Table 3, which will be detailed later. The eight anisotropic coefficients,  $a_m, b_m, c_m$  and  $g_m$  (with  $m = 1, 2$ ), were calibrated using normalized uni-axial yield stresses, R-values listed in along with  $R_b$  and further assuming that  $\sigma_b = 1$ . The calibrated material parameters were listed in Table 3.

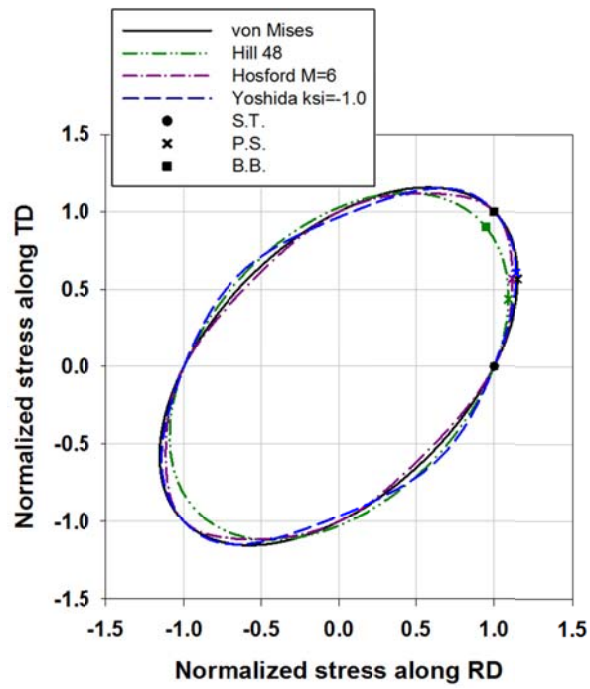
Table 3 Material parameters for three yield functions of HB780 and DP780

HB780						
Hill	F	G	H	L	M	N
	0.5304	0.5795	0.4205	1.5000	1.5000	1.9059
Hosford	M=10					
	C1	C2	C3	C4	C5	C6
	1.0000	0.8392	1.1571	1.3725	1.0646	0.6466
Yoshida	C7	C8	C9	C10	C11	C12
$\xi = 2.1$	0.7302	1.0424	1.1764	1.6556	1.0669	0.8301
	C13	C14	C15	C16		
	1.1712	2.1374	1.0806	1.7155		
DP780						
Hill	F	G	H	L	M	N
	0.5618	0.6088	0.3912	1.5000	1.5000	1.7682
Hosford	M=6					
	C1	C2	C3	C4	C5	C6
	1.0000	0.7823	0.5558	0.4298	0.6387	1.0164
DP780	C7	C8	C9	C10	C11	C12
$\xi = -1.0$	1.2380	1.1646	0.6849	0.5757	0.9017	1.1577
	C13	C14	C15	C16		
	1.0438	0.6887	1.1207	1.1050		

The three yield function contours were compared with the von Mises yield function in for the plane stress condition. The variations of uni-axial yield stresses and R-values calculated for the two anisotropic yield functions were compared with the measured values in and , which showed that the Yoshida function properly represented both the yield stress and R-value variations, while the Hill1948 function properly represented only the R-value variation.

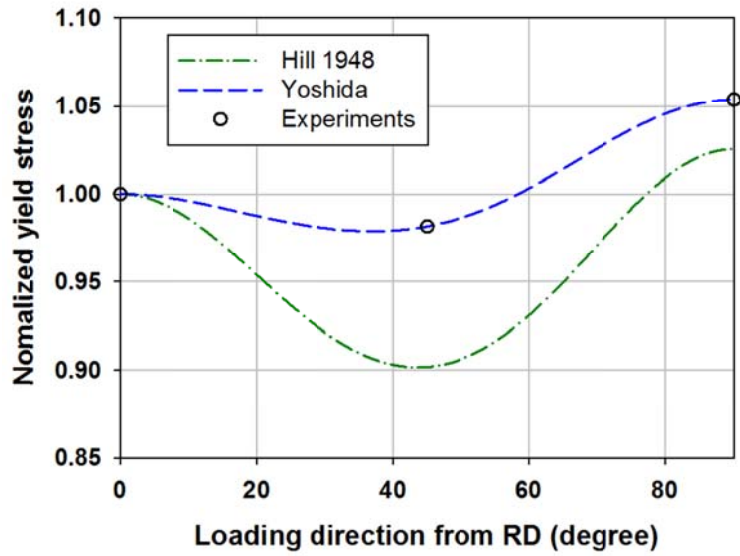


(a)

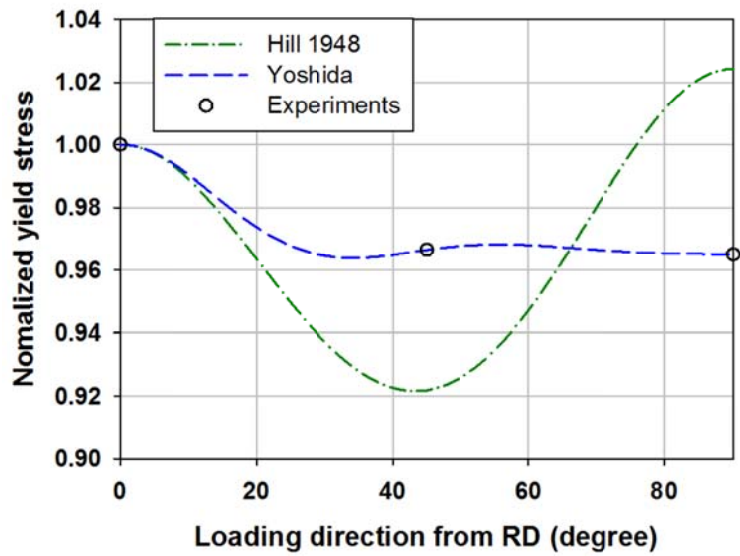


(b)

Figure 9 Comparison of Hill1948, Hosford and Yoshida yield functions: (a) HB780 (b) DP780

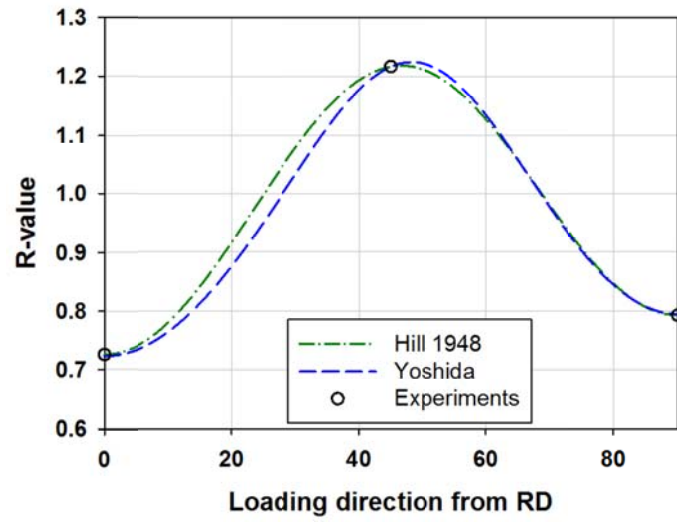


(a)

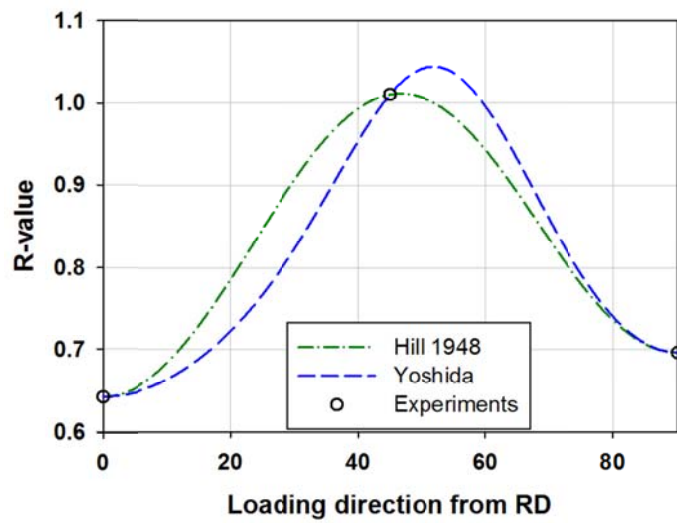


(b)

Figure 10 Variation of the normalized uni-axial yield stress with respect to the loading direction: (a) HB780 (b) DP780



(a)



(b)

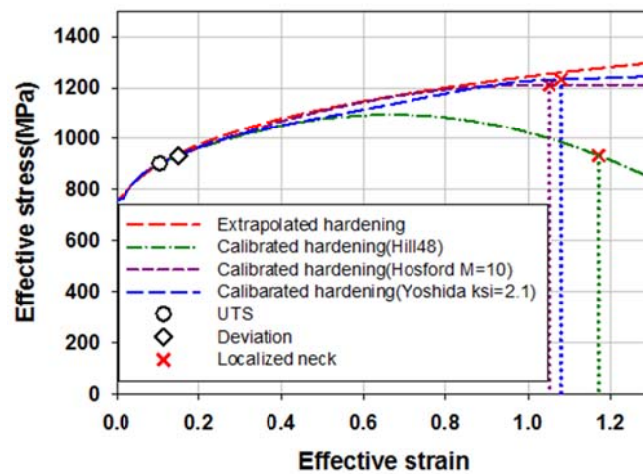
Figure 11 Variation of the R-value with respect to the loading direction: (a) HB780 (b) DP780

### **3.1.4 Inverse calibration of hardening deterioration with the simple tension**

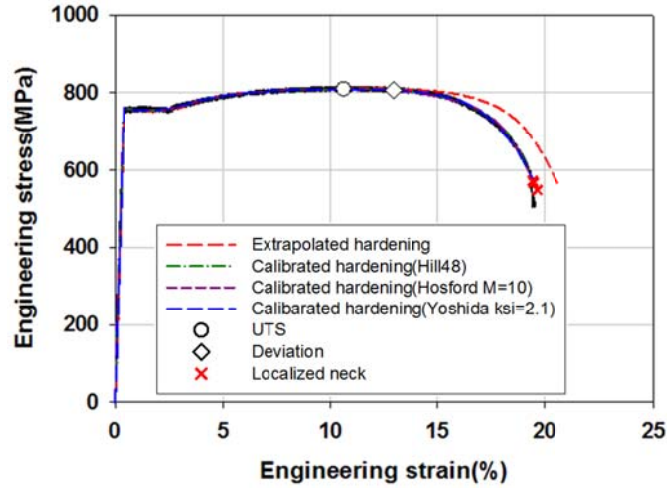
To characterize hardening behavior with its hardening deterioration beyond the uniform deformation limit before failure, the numerical inverse calibration method was conducted by performing iteratively the finite element analysis of the reference simple tension test (with strain rate 0.001 /s along the rolling direction) (Chung et al., 2011b). For numerical simulations, ABAQUS/Explicit (ABAQUS, 2007) was applied, utilizing the eight node 3-D continuum element (C3D8R). Numerical simulations were iterated with various hardening deterioration behavior until the simulated engineering stress and engineering strain data well matched with the experimental data with proper hardening deterioration. (Kim et al., 2016)

Since the strain rate sensitivity affects the strain localization, its values listed in Table 2 were utilized for the numerical simulations. Since the mesh size also affects strain localization, simulations were tried out with gradually smaller mesh size until the size did not affect the engineering stress and engineering strain result. The resulting mesh size was 0.2636 x 0.2636 x 0.2636 mm with eleven layers for 2.9 mm thickness for both samples. The hardening behavior calibrated beyond UTS for three yield functions of the two sample sheets and their performance in the engineering stress and engineering strain data were shown in Figure 12 and Figure 13. The inversely calibration simulation results well matched with measured engineering stress and engineering strain data. For both samples, the extrapolated hardening data without any deterioration over-predicted the engineering stress and engineering strain data. The

amount of hardening deterioration of HB780 was insignificant for the two non-quadratic yield functions but Hill's has some degree of deterioration. The hardening deterioration of DP780 was significant for all three yield functions. Note that initially when the non-quadratic parameters were unknown for Hosford and Yoshida yield functions, hardening deterioration was calibrated for those yield functions with various parameters and the proper parameters were ultimately finalized considering their performance in predicting strain localization in the hemispherical dome stretch test: simultaneous calibration of hardening deterioration and non-quadratic parameters based on the simple tension and hemispherical dome stretch tests. Hardening deterioration for the ultimately chosen parameters was shown here.

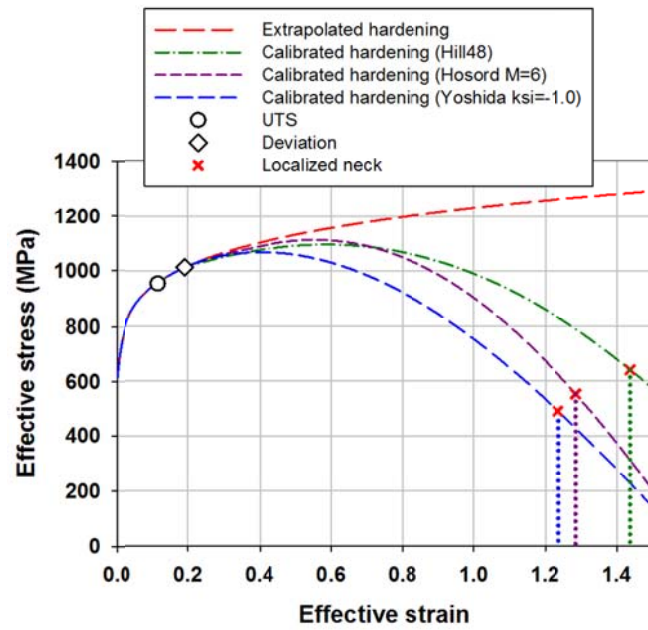


(a)

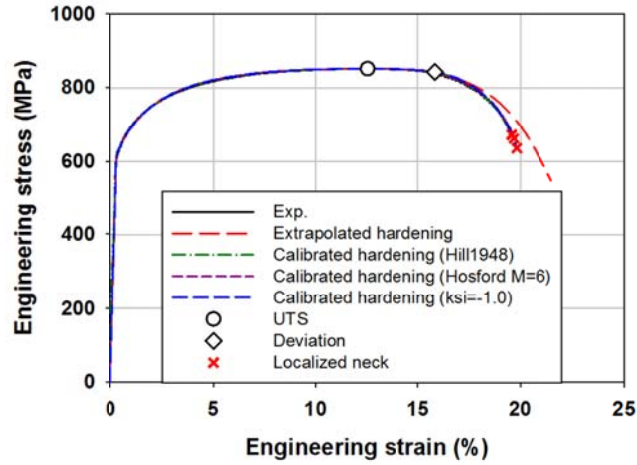


(b)

Figure 12 Comparison of hardening curves of HB780: (a) effective stress-effective plastic strain curves (b) engineering stress-engineering strain curves



(a)



(b)

Figure 13 Comparison of hardening curves of DP780: (a) effective stress-effective plastic strain curves (b) engineering stress-engineering strain curves

To determine the onset of failure by strain localization (or the localized necking), an element with the maximum accumulated effective plastic strain was identified as the critical element located at the center of the specimen and in the middle of thickness. As for its neighboring elements, two sets of 10 elements at the surface just above the critical element were considered, whose total length was approximately identical with the 2.5 mm diameter of a grid used in the simple tension as shown in Figure 14. The two sets, dubbed as Grid 1 and Grid 2, were utilized to identify the safe and failed grids at the moment of failure of the critical element by strain localization, respectively. Grids 1 and 2 consisted of the 3rd to 12th elements and the 2nd to 11th elements, which approximately composed 2.5 mm diameter of one grid in the rolling direction, respectively, as shown in Figure 14, while the element just above the critical element was considered the 1st element

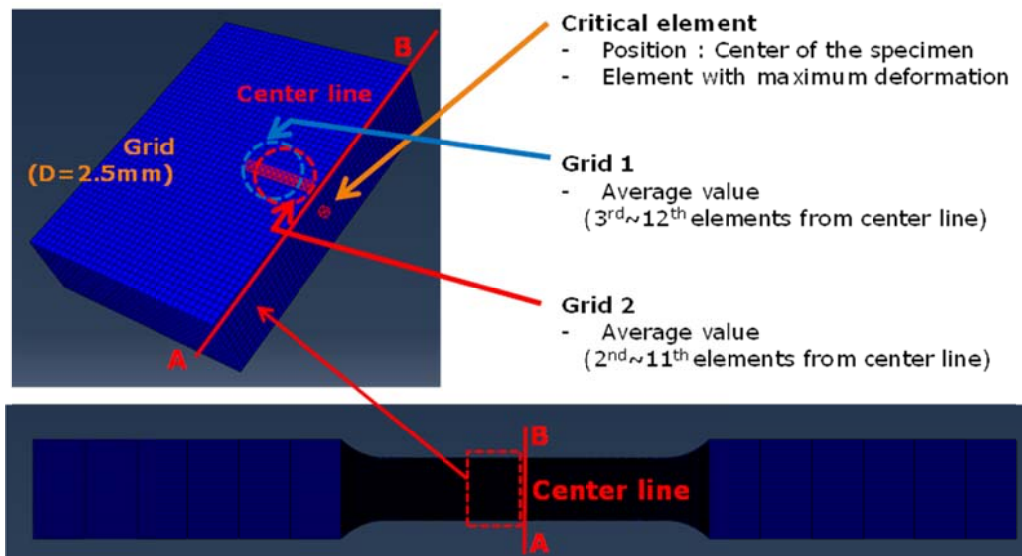
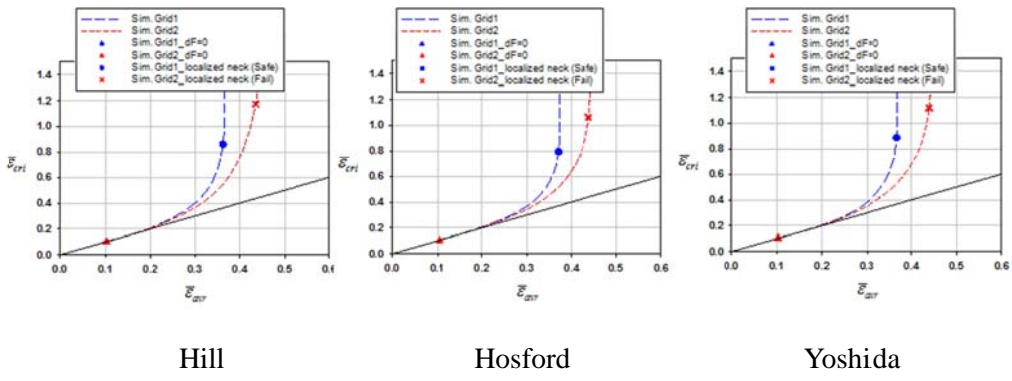
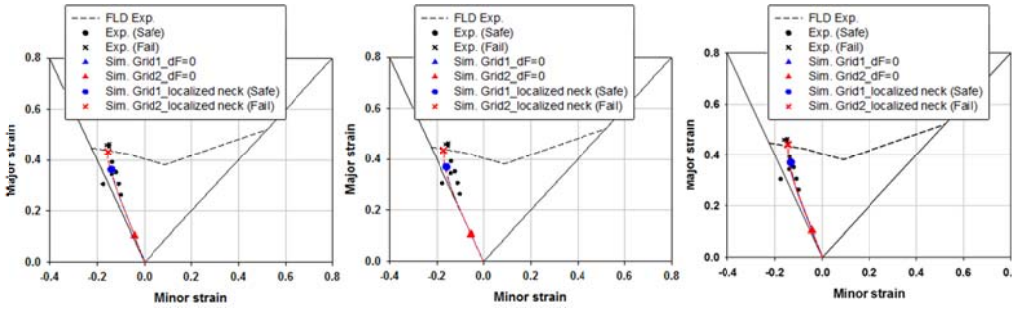


Figure 14 The critical and its neighboring elements for the simple tension test

To determine strain localization, the effective strain of the critical element and the average effective strains of Grids 1 and 2 were numerically monitored through the test as shown in Figure 15 and Figure 16. Those three strains were identical initially but diverged as strain was localized at the critical element. Failure by strain localization was identified when the ratio of the effective strain increment of the critical element and the average effective strain increment at Grid 2 was larger than 30.0 as shown in Figure 15 (a) and Figure 16 (a):  $d\bar{\epsilon}_{cri} / d\bar{\epsilon}_{avr} \geq 30.0$ . When the ratio reached this number, only the critical element deformed, while neighboring elements were virtually frozen (so that Grid 1 also satisfies the criterion). Note that the two hot-rolled steel sheets having rather thick thickness showed more gradual strain localization compared to the rather thin cold-rolled sheet (Chung et al., 2014b).

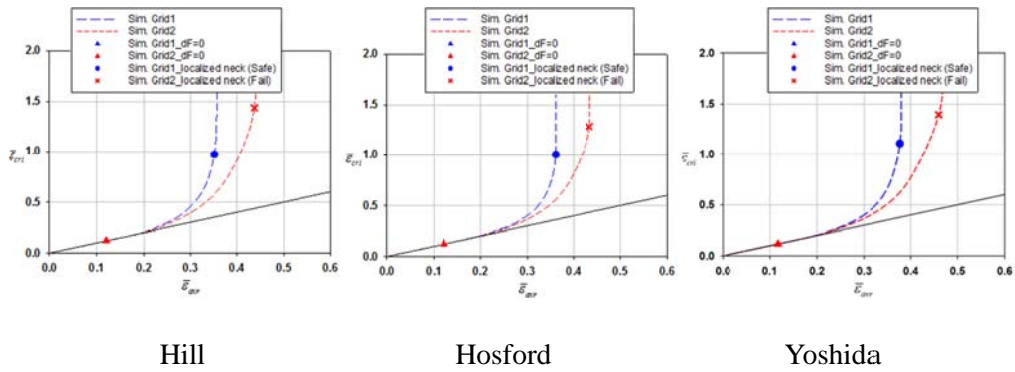


(a)

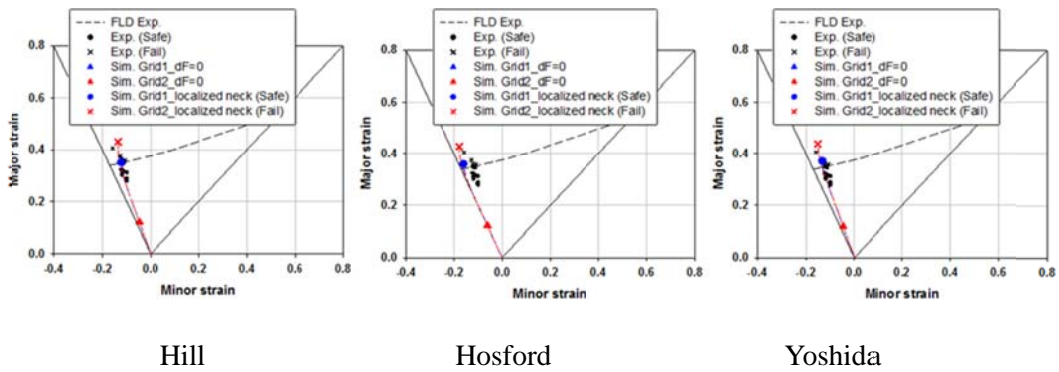


(b)

Figure 15 Simple tension simulation results of HB780: (a) effective strain ratio between the critical and neighboring elements (b) strain-based FLD



(a)



(b)

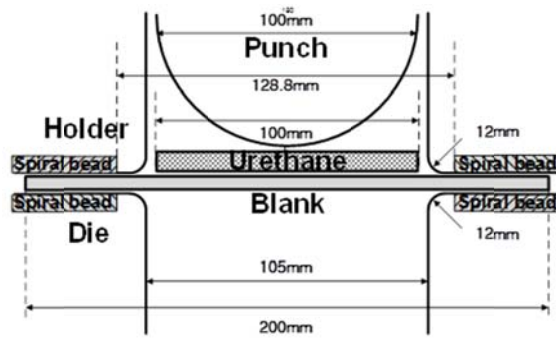
Figure 16 Simple tension simulation results of DP780: (a) effective strain ratio between the critical and neighboring elements (b) strain-based FLD

The failure points by strain localization were marked in the effective and engineering stress and strain curves in Figure 12 and Figure 13, respectively. Note that even though the average UTS and total strains for the gauge length were only around 10% and 20% (in engineering strain), respectively, for the simple tension test, critical elements deformed significantly beyond 1.0 in terms of the accumulative strain before failure for both samples. The numerically obtained strain-based forming limit of the simple

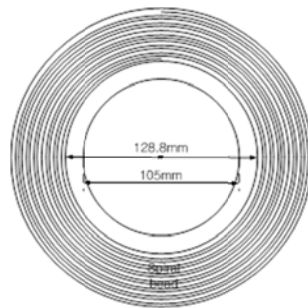
tension test was also plotted in Figure 15 (b) Figure 16 (b), which reasonably well matched with the measured FLD for all three yield functions of both samples. Since the performance of the three yield functions in addressing strain localization in the simple tension test was virtually the same, the proper yield function was determined based on the hemispherical dome stretching test, which is routinely applied to measure forming limit diagram.

### **3.1.5 Hemispherical dome stretching test**

The hemispherical dome stretching test was conducted using a 50 ton double action hydraulic press machine with spiral beads on the holder and the die to hold the blank without slippage, as shown in Figure 17. (Kim et al., 2016) The punch speed was 20 mm/min and the blank holding force was 450 kN. Between the punch and the blank, the urethane pad and the beef tallow were used for lubrication. Four shapes of specimens with the width of 25, 75, 130 and 200 mm (with the length of 200 mm aligned along the rolling direction) were prepared by the wire cutting process as shown in Figure 18 to cover various deformation modes near the simple tension, plane strain and balanced biaxial stretching modes. Circular grids with the diameter of 2.5 mm were etched on their surfaces using the laser grid to measure failure strains and the experimentally obtained strain-based FLD results were plotted in Figure 19.



(a)



(b)

Figure 17 Schematic view of the hemispherical dome stretching test with dimensions:

(a) tool geometry (b) the spiral bead

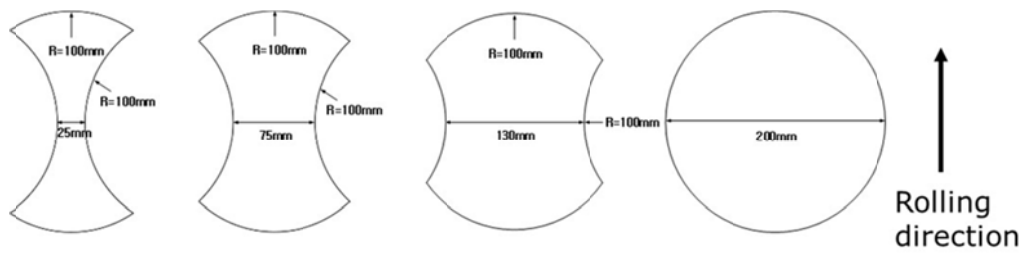
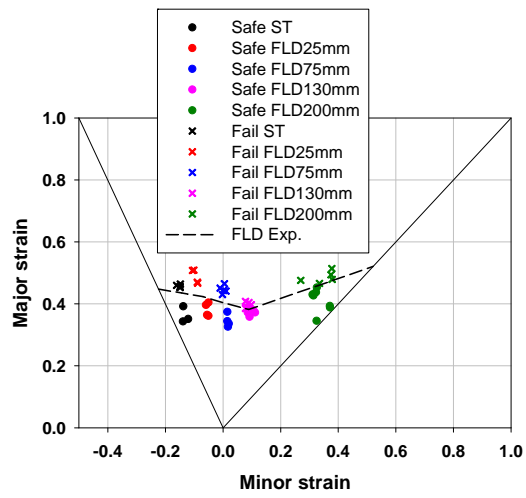
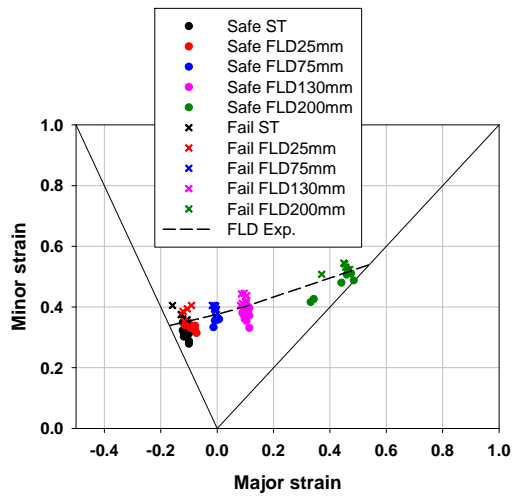


Figure 18 Specimen geometry of the hemispherical dome stretching test



(a)



(b)

Figure 19 Measured forming limit diagram: (a) HB780 (b) DP780

In order to evaluate whether specimens failed with strain localization or by fracture (without strain localization), the failed surfaces of specimens of the hemispherical dome stretching test were examined. For HB780, failure with strain localization was observed for all test specimens. As for DP780, surfaces for all specimens showed failure with strain localization except the 200 mm specimen (whose deformation mode is near the balanced biaxial stretching mode), for which the fractured surface showed less obvious failure by strain localization, suggesting that it may have failed by fracture without strain localization unlike all other cases. Note that failure of the 200 mm blank of both samples occurred in parallel with the rolling direction unlike all other cases with smaller widths.

Utilizing the mechanical properties characterized based on the simple tension test for both samples, the hemispherical dome stretching test was simulated using ABAQUS/Explicit (ABAQUS, 2007). As for the mechanical property of the urethane pad with the thickness of 2.0 mm, Ogden's isotropic hyperelastic material model (Ogden, 1972) was applied in this work, in which the strain energy density is expressed in terms of deviatoric principal stretches as

$$U = \sum_{i=1}^N \frac{2\mu_i}{\alpha_i^2} (\bar{\lambda}_1^{\alpha_i} + \bar{\lambda}_2^{\alpha_i} + \bar{\lambda}_3^{\alpha_i} - 3) + \sum_{i=1}^N \frac{1}{D_i} (J^{el} - 1)^{2i} \quad (3.1.2)$$

where  $\bar{\lambda}_i$  are the deviatoric principal stretches and  $J^{el} = \det \mathbf{F}^{el}$  with  $\mathbf{F}^{el}$  as the elastic deformation gradient. Here, the values of  $\mu_i$ ,  $\alpha_i$  and  $D_i$  with  $N=1$  listed in Table 4 were used in this work as suggested elsewhere (Chung et al., 2014b).

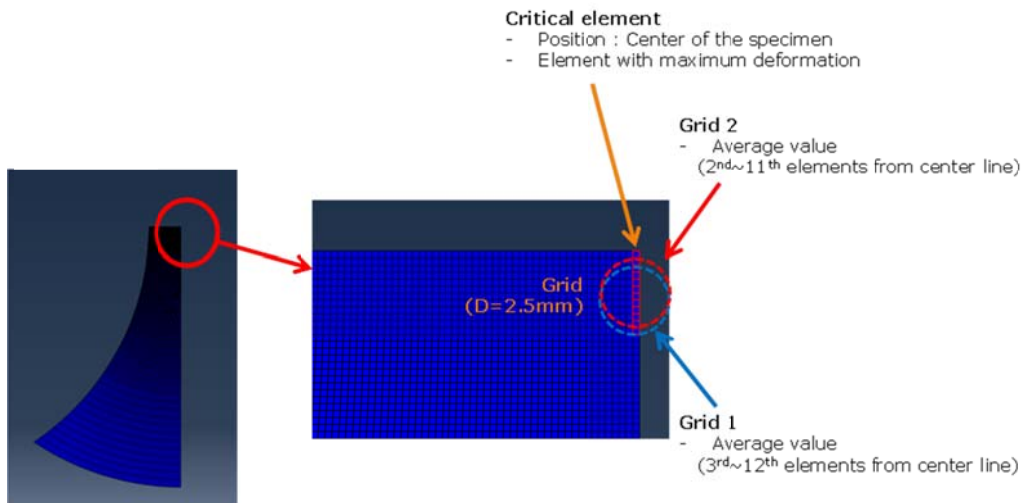
Table 4 The material parameters of the urethane pad

$N$	1
$\mu_1(MPa)$	3.7039
$\alpha_1$	3.2170
$D_1(MPa^{-1})$	1.0872

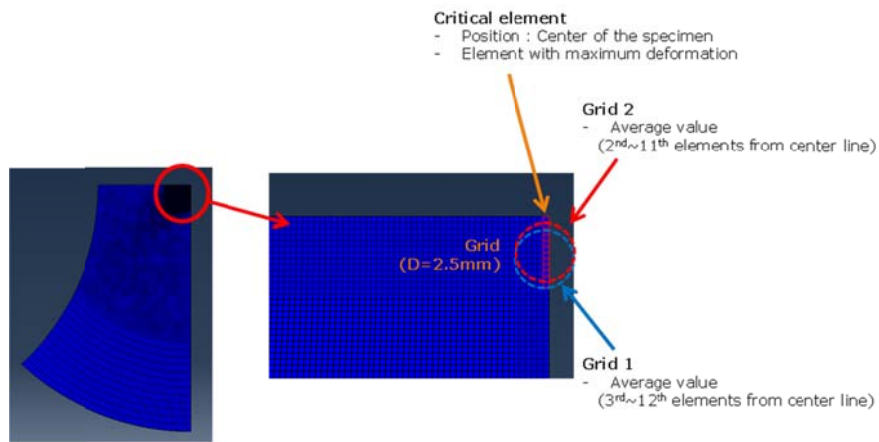
The eight node 3-D continuum element (C3D8R) with the size of 0.2636 x 0.2636 x 0.2636 mm were utilized in the center of blank where the failure occurred, while coarse meshes were used in the other regions. Eleven layers through the thickness of 2.9 mm were utilized for blanks as done for the simple tension test. As for the urethane pad, the eight node 3-D continuum element (C3D8R) with the size of 1.0 x 1.0 x 0.67 mm was employed with three layers through the thickness of 2.0 mm, while the rigid element (R3D4) was utilized for the tools. Simulations were performed only for a quarter of the blank considering symmetry, following the test conditions previously discussed. As for friction, two different friction coefficients were assumed for best fitting with the experiment results: 0.1 for the blank/urethane pad and the punch/urethane pad, while 0.8 for the blank/die and the blank/holder, considering spiral bids on the die and the holder.

To determine the onset of failure by strain localization (or the localized necking), deformations at the critical element, which deformed most in terms of the accumulated effective plastic strain, and its neighboring elements were monitored following the same procedure performed for the simple tension test, without referring to any forming

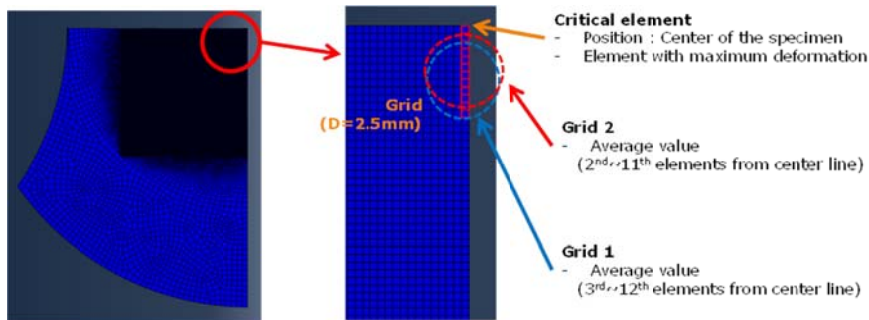
limit criterion. Note that all cases were simulated until failure occurred by strain localization, even for the FLD 200mm test of DP780, which may have failed without strain localization in experiment. The critical element was located at the top surface (the opposite side of tool contact) of the center of the specimen for all four blanks of both samples. As for its neighboring elements, two sets of 10 elements dubbed as Grid 1 and Grid 2 were utilized to identify the safe and failed grids at the moment of failure, which consisted of the 3<sup>rd</sup> to 12<sup>th</sup> elements and the 2<sup>nd</sup> to 11<sup>th</sup> elements, respectively, as shown in Figure 20, while the critical element was the 1<sup>st</sup>. Failure by severe strain localization was identified when the ratio of the effective strain increment of the critical element and the average effective strain increment of neighboring elements (of Grid 2) was 30.0, as shown in Figure 21 (a) - Figure 28 (a).



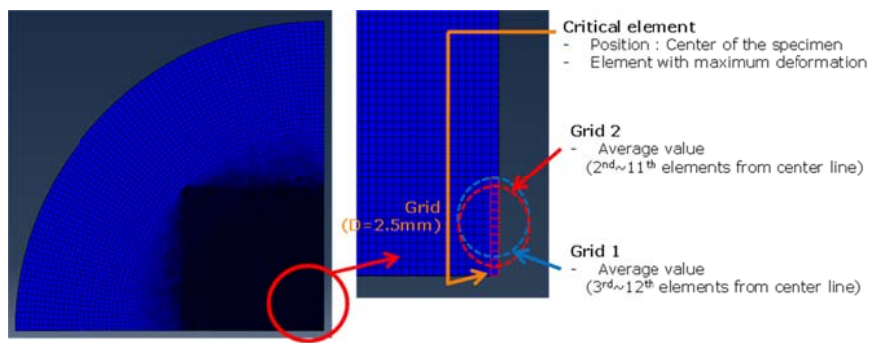
(a)



(b)

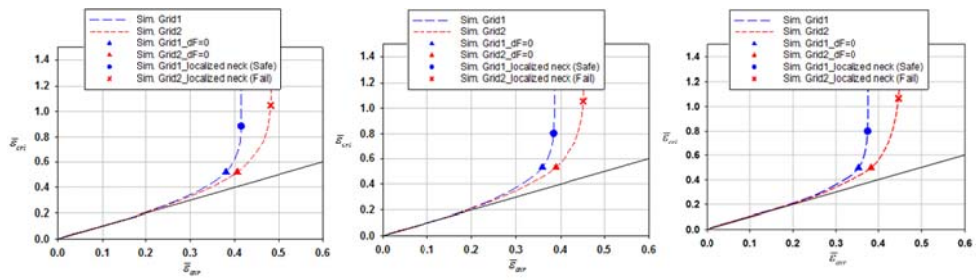


(c)



(d)

Figure 20 The critical and neighboring elements for the hemispherical dome stretching test of blanks with the width of (a) 25mm (b) 75mm (c) 130mm (d) 200mm

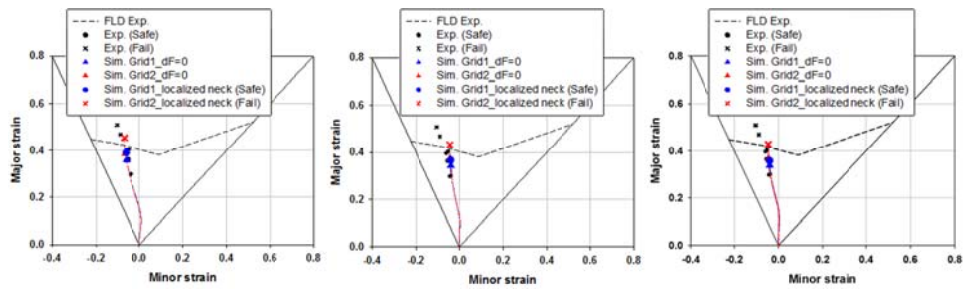


Hill

Hosford

Yoshida

(a)

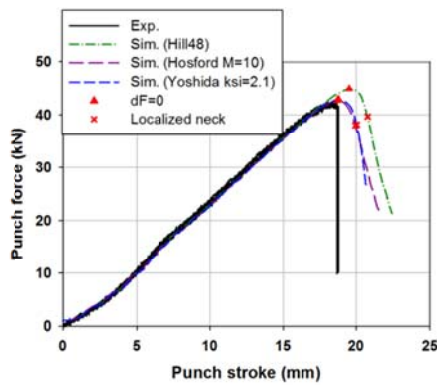


Hill

Hosford

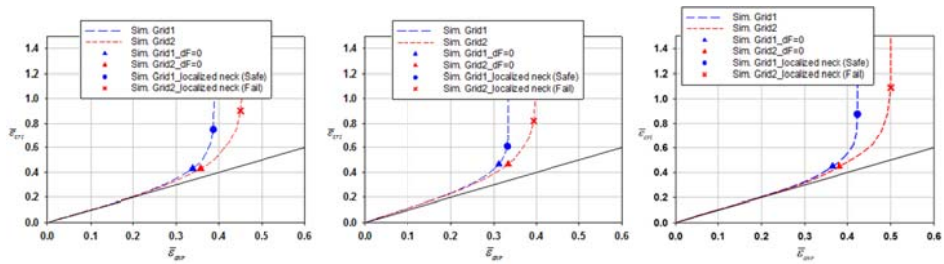
Yoshida

(b)



(c)

Figure 21 FLD simulation results of HB780 for the 25mm blank: (a) effective strain ratio between the critical and neighboring elements (b) strain-based FLD (c) force-displacement curve

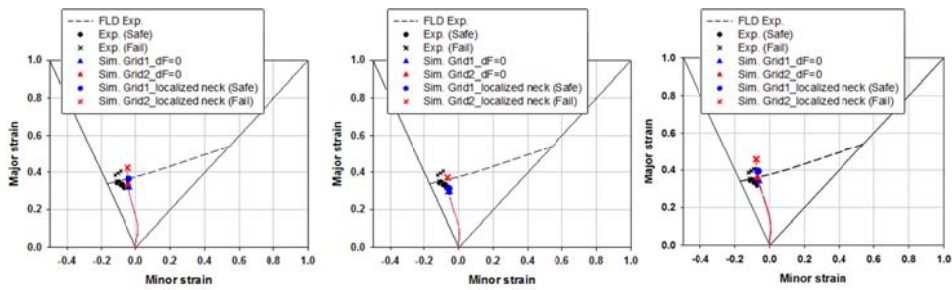


Hill

Hosford

Yoshida

(a)

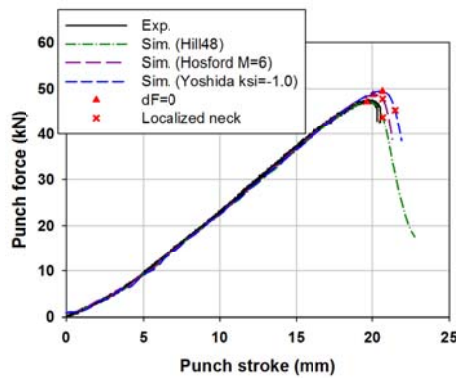


Hill

Hosford

Yoshida

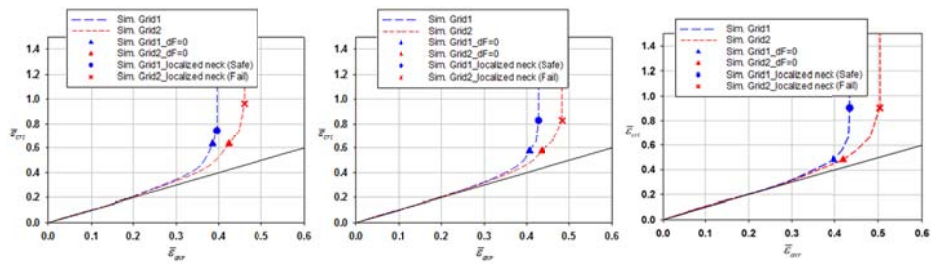
(b)



(c)

Figure 22 FLD simulation results of DP780 for the 25mm blank: (a) effective strain ratio between the critical and neighboring elements (b) strain-based FLD (c) force-displacement curve



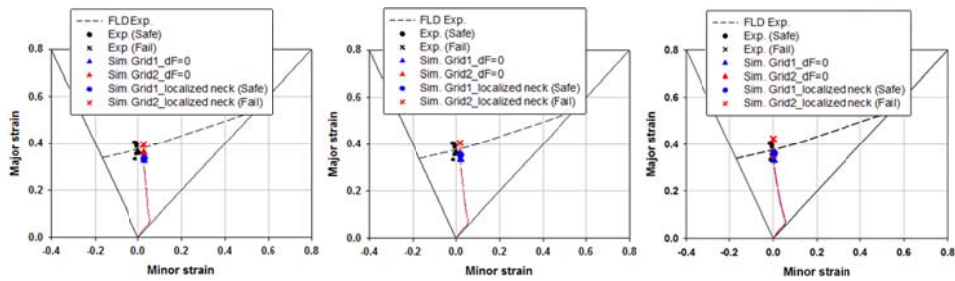


Hill

Hosford

Yoshida

(a)

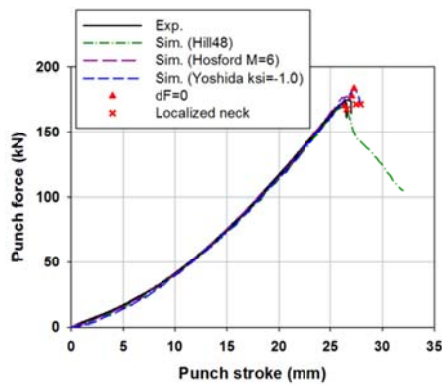


Hill

Hosford

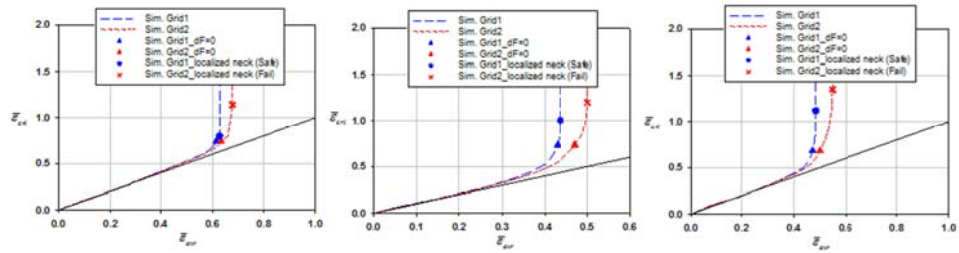
Yoshida

(b)



(c)

Figure 24 FLD simulation results of DP780 for the 75mm blank: (a) effective strain ratio between the critical and neighboring elements (b) strain-based FLD (c) force-displacement curve

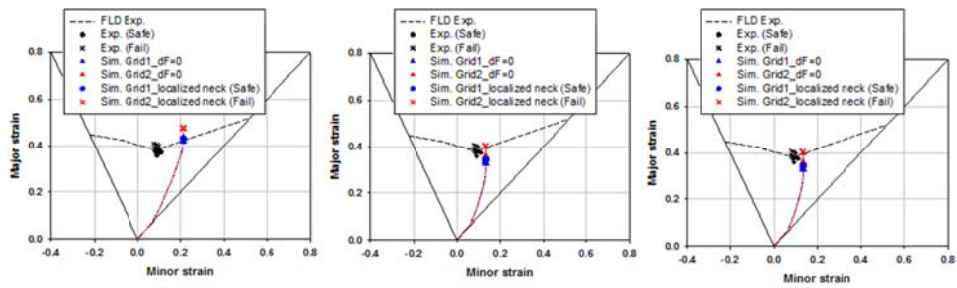


Hill

Hosford

Yoshida

(a)

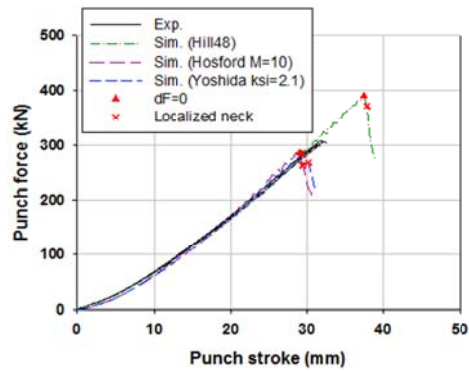


Hill

Hosford

Yoshida

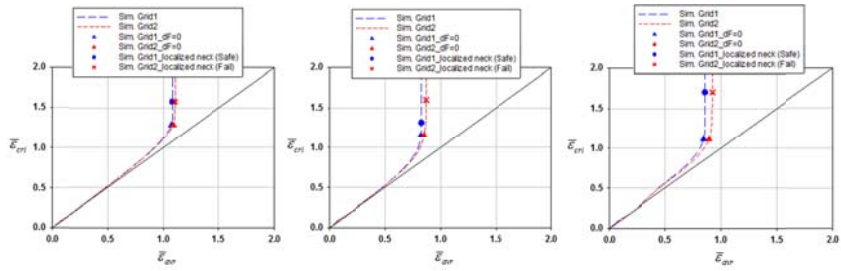
(b)



(c)

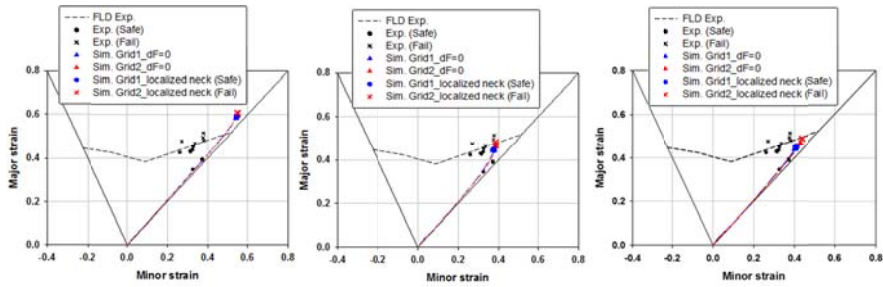
Figure 25 FLD simulation results of HB780 for the 130mm blank: (a) effective strain ratio between the critical and neighboring elements (b) strain-based FLD (c) force-displacement curve





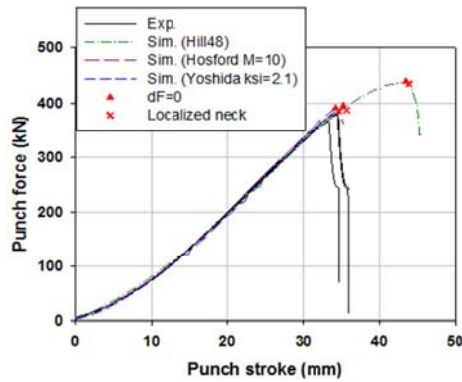
Hill                      Hosford                      Yoshida

(a)



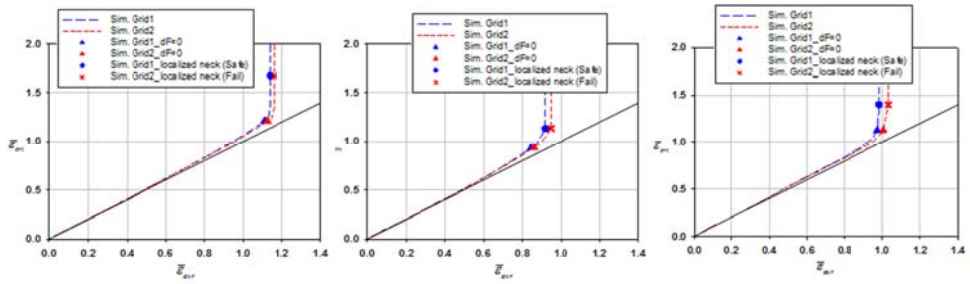
Hill                      Hosford                      Yoshida

(b)

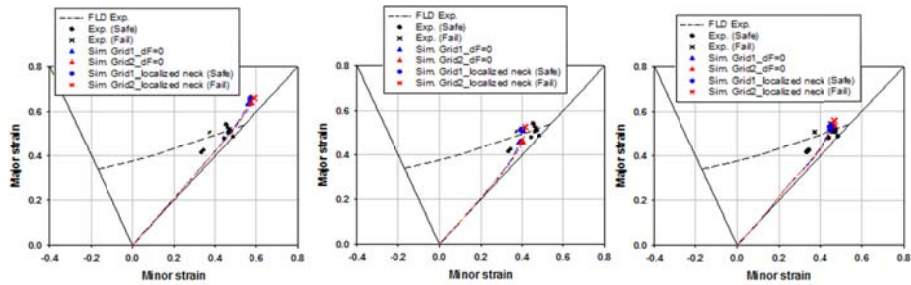


(c)

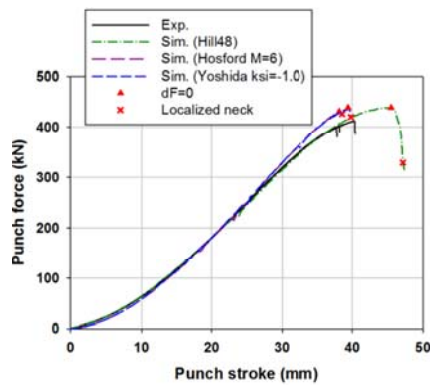
Figure 27 FLD simulation results of HB780 for the 200mm blank: (a) effective strain ratio between the critical and neighboring elements (b) strain-based FLD (c) force-displacement curve



Hill                      Hosford                      Yoshida  
(a)



Hill                      Hosford                      Yoshida  
(b)



(c)

Figure 28 FLD simulation results of DP780 for the 200mm blank: (a) effective strain ratio between the critical and neighboring elements (b) strain-based FLD (c) force-displacement curve

All the material parameters of the quadratic Hill1948 yield function were calibrated based on the simple tension test; however, the non-quadratic parameters of the Hosford and Yoshida yield functions were determined based on the hemispherical dome stretching test, since the performance of their various values in addressing strain localization in the simple tension test was virtually the same. Various  $M$  and  $\xi$  values of the Hosford and Yoshida yield functions (with their corresponding hardening deterioration behavior calibrated for the simple tension test) were tried out, respectively, until best fit with experiments were achieved for the hemispherical dome stretching test. The resulting  $M$ -values for HB780 and DP780 were 10.0 and 6.0, respectively, while the  $\xi$  values became 2.1 and -1.0 for HB780 and DP780, respectively, as listed Table 3. The  $M$  value in the Hosford yield function is commonly recommended as  $M=6$  and  $M=8$  for bcc and fcc materials, respectively, based on the crystal plasticity model, in which only the crystallographic texture and slip system in polycrystalline materials are considered. However, the empirically calibrated values here were different from the recommended values, which might be caused by the effects of grain shapes and sizes added in the empirical values.

Regarding the performance of the calibrated three yield functions, numerically obtained forming limit strains and force-displacement curves were reasonably well matched with experimental results for the 25 and 75 mm blanks for all three yield functions of both samples as shown in Figure 21 - Figure 24. However, for the 130 and 200 mm blanks, the results of the Hill1948 yield function showed delayed failure in forming limit strains and force-displacement curves for both samples, while the Hosford and Yoshida results showed reasonably good match with experiments as

shown in Figure 25 - Figure 28.

The different performance between the quadratic and non-quadratic yield functions might be related to their yield function shape difference shown in Figure 9. Since the shapes of three yield functions were similar between the simple tension and plane strain modes for both samples, the results for the 25 and 75 mm blanks were similar each other for all the three functions of both samples. However, the shapes between the plane strain and balanced biaxial stretching modes were similar for the Hosford and Yoshida yield functions and they were not so similar with that of the Hill function for both samples. Therefore, the Hosford and Yoshida yield function results were similar each other for the 130 and 200 mm blanks, while they differed from the Hill function result. The delayed strain localization of the Hill case was related to its more bulged out shape between the balanced biaxial stretching and plane strain modes for both samples. Consequently, the non-quadratic Hosford and Yoshida yield functions with their particular  $M$  and  $\xi$  values might be proper choices for the particular hot-rolled steel sheets considered here for the failure analysis of their sheet forming with strain localization. However, there is a major difference between the Hosford and Yoshida yield functions that the former is isotropic and the latter is anisotropic such that, even though both properly predicted failure patterns for specimens with smaller widths of both samples, only the anisotropic Yoshida yield function properly predicted failure lines aligned along the rolling direction of both samples as its simulation results.

As for the failure of the 200 mm blank of DP780, the reasonably well predicted failure using the Yoshida yield function suggests that it failed with strain localization. When

its strain localization shown in Figure 28 (a) is compared that of all other cases simulated by the Yoshida yield function, its strain localization was so abrupt and rapid that its fractured surface did not show obvious strain localization by visual inspection in experiment, unlike all other cases.

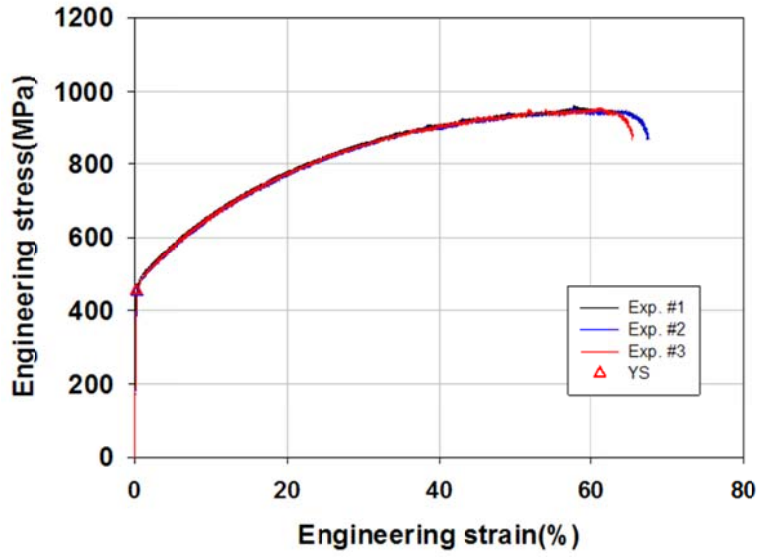
As for the failure lines aligned along the rolling direction of the FLD 200 mm blank of both samples, it was numerically confirmed that, when  $R_b > 1.0$ , its direction is aligned along the transverse direction for both samples, confirming that the measured  $R_b$  value affected the failure line direction of the FLD 200 mm case. The average (for Grid 2) and critical effective plastic strains at the moment of failure by strain localization were confirmed that critical elements deformed significantly near or beyond 1.0 in terms of the accumulative effective strain before failure by strain localization for all the FLD test cases of both samples.

## **3.2 Failure without strain localization**

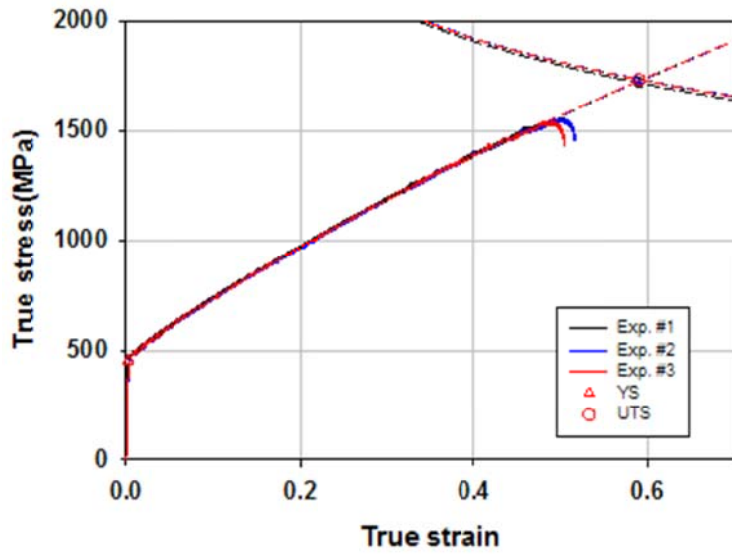
As for failure without strain localization, advanced high strength hot-rolled steel sheet TWIP980 (twinning induced plasticity) produced by POSCO with the thickness of 3.1 mm was considered. For mechanical properties, the simple tension for hardening behavior with strain rate sensitivity and fracture tests with various specimens for triaxially and strain rate dependent fracture criteria summarized here. Moreover, the numerical analysis was conducted based on the experimental results.

### **3.2.1 Simple tension test**

The simple tension tests were conducted utilizing the ASTM E8M standard specimen prepared by the wire cutting process along the rolling direction as shown in Figure 3. As for material anisotropy, simple tension tests were conducted along the rolling ( $0^\circ$ ), transverse ( $90^\circ$ ) and in-between ( $45^\circ$ ) directions. Tensile speed was 0.05 mm/s, which corresponds to the strain rate of approximately 0.001 /s when deformation is uniform within the gauge length of 50.0 mm. The particular strain rate was considered as the reference strain rate to describe the strain rate sensitivity. Figure 29-Figure 31 shows typical engineering stress-engineering strain and true stress-true strain measured for three directions. As shown in the figures, the uniform deformation limit was beyond the failure point, which means the failure without strain localization. The measured mechanical properties, averaged for three tests repeated per each direction, were summarized in Table 5.

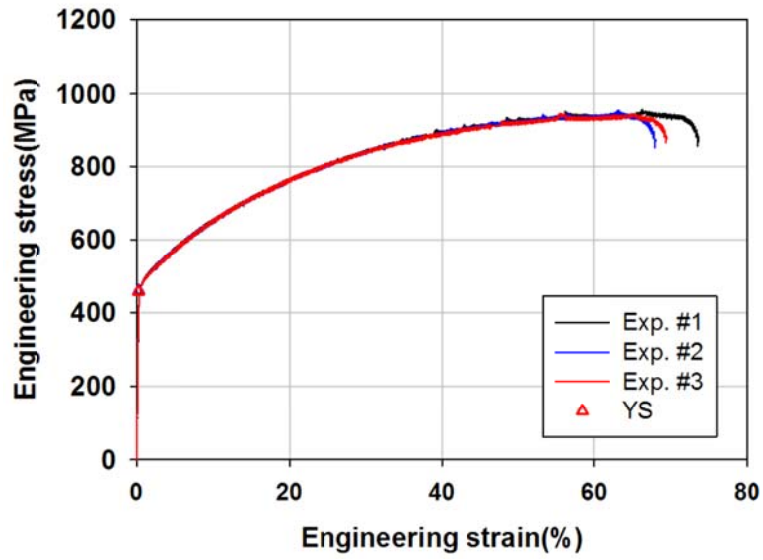


(a)

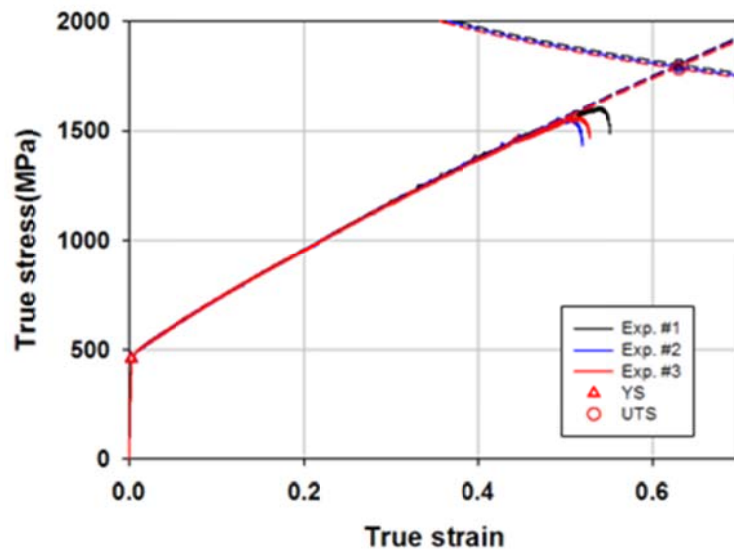


(b)

Figure 29 Engineering stress-engineering strain and true stress-true strain curves in the rolling direction ( $0^\circ$ )

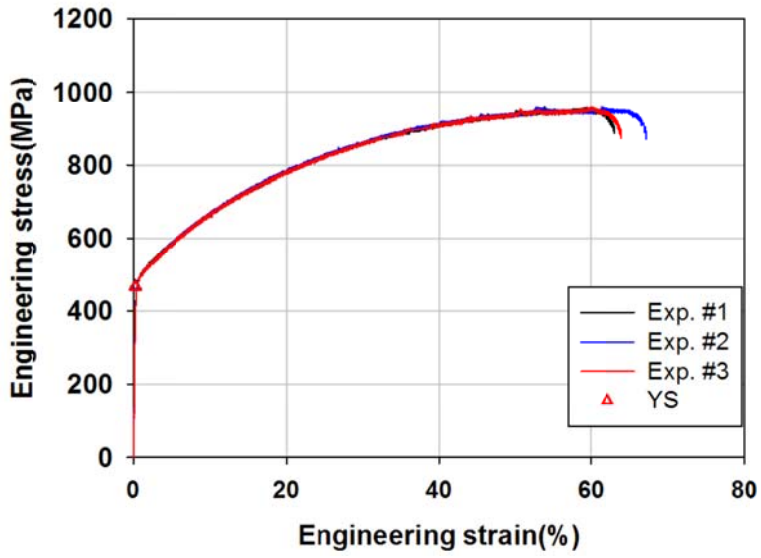


(a)

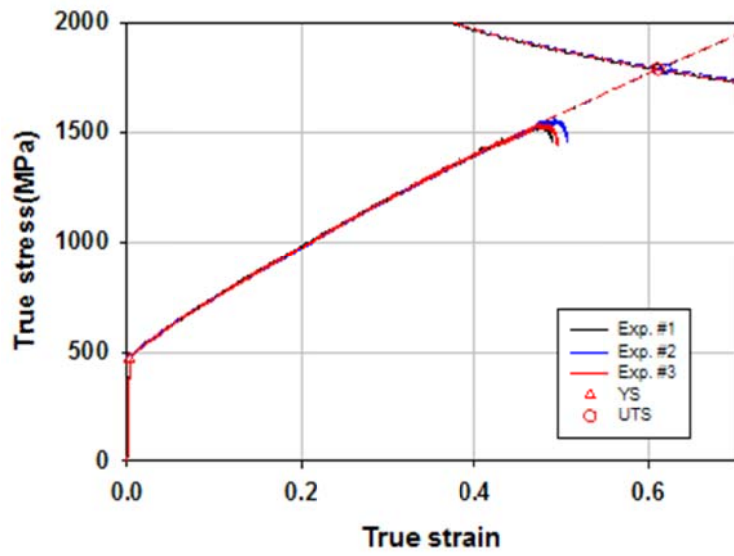


(b)

Figure 30 Engineering stress-engineering strain and true stress-true strain curves in-between direction ( $45^\circ$ )



(a)



(b)

Figure 31 Engineering stress-engineering strain and true stress-true strain curves in transverse direction ( $90^\circ$ )

Table 5 Mechanical (engineering) properties of TWIP980

	Direction	E (GPa)	YS (MPa)	UTS (MPa)	Elongation (%)		R-value
					Uniform	Total	
TWIP980	RD (0°)	183.6	451.9	947.5	59.2	66.93	0.831
	In-between (45°)	189.6	458.7	941.6	65.0	70.46	0.845
	TD (90°)	186.9	467.1	952.8	59.9	64.4	1.017

As for the hardening behavior, simple tension test data along the rolling direction was considered as the reference state for the isotropic hardening law. To describe the hardening behavior in the uniform deformation range below UTS, the Swift type fitting law was applied by utilizing the least square method and resulting fitting constants were listed in Table 6. The hardening fitting curves well matched with the experiments as shown in Figure 32.

Table 6 Hardening behavior with strain rate sensitivity

Swift type: $\bar{\sigma} = K(\bar{\varepsilon} + \bar{\varepsilon}_0)^n \left( \frac{\dot{\bar{\varepsilon}}}{\dot{\bar{\varepsilon}}_0} \right)^m$				
$K$	$\bar{\varepsilon}_0$	$n$	$\dot{\bar{\varepsilon}}_0$	$m$
(MPa)				
2254.0	0.1145	0.0048	0.001	-0.00343

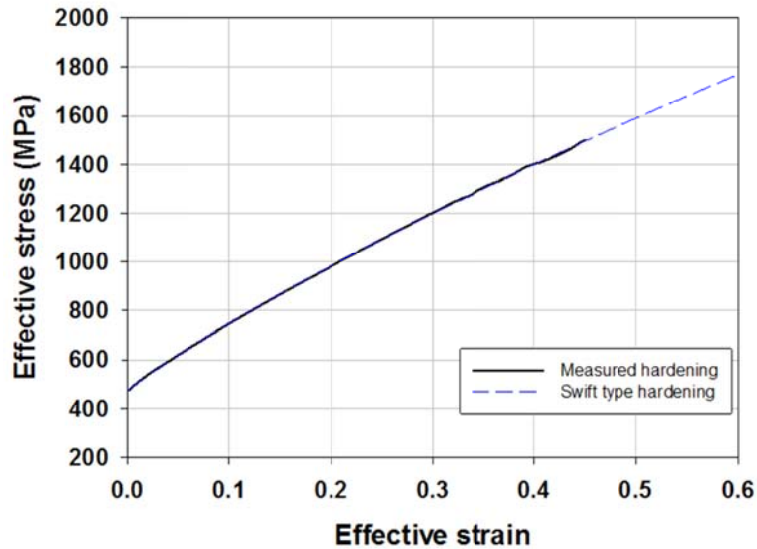


Figure 32 Comparison between hardening fitting curves and experiment results for TWIP980

To measure the R-value (the ratio of the transverse strain increment with respect to the thickness strain increment in simple tension), the transverse strain was measured using the strain gage attached perpendicular to the tensile direction in the simple tension test and the thickness strain was calculated assuming the constant volume condition. Measured R-values of the three directions were plotted in Figure 33 and summarized in Table 5. Based on the measured R-values ( $R_0$ ,  $R_{45}$ ,  $R_{90}$ ), quadratic anisotropic Hill1948 yield function was calibrated. F, G, H, L, M and N which are anisotropic coefficients as listed in were calibrated with assuming that  $L=M=1.5$ . The calibrated material parameters were listed in Table 7. The Hill yield function contour was compared with the von Mises yield function in Figure 34 for the plane stress condition.

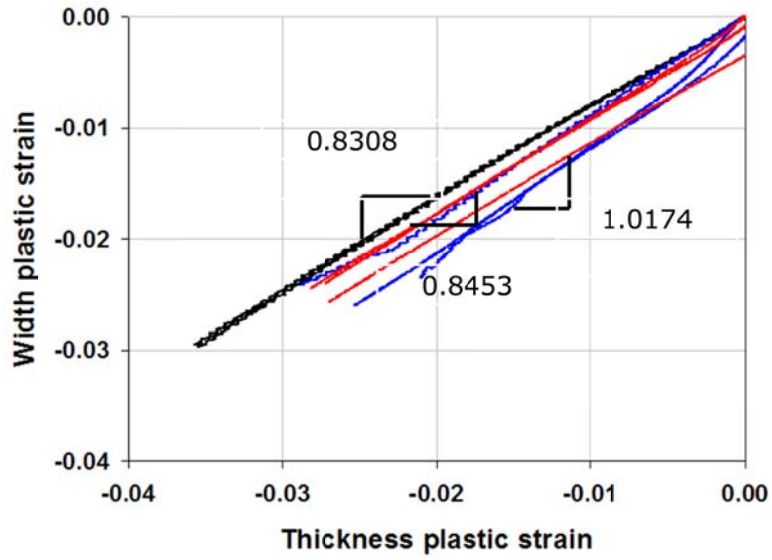


Figure 33 Measured R-values for TWIP980

Table 7 Material parameters for Hill 1948 yield function of TWIP980

TWIP980						
Hill	F	G	H	L	M	N
	0.4461	0.5462	0.4538	1.5000	1.5000	1.3349

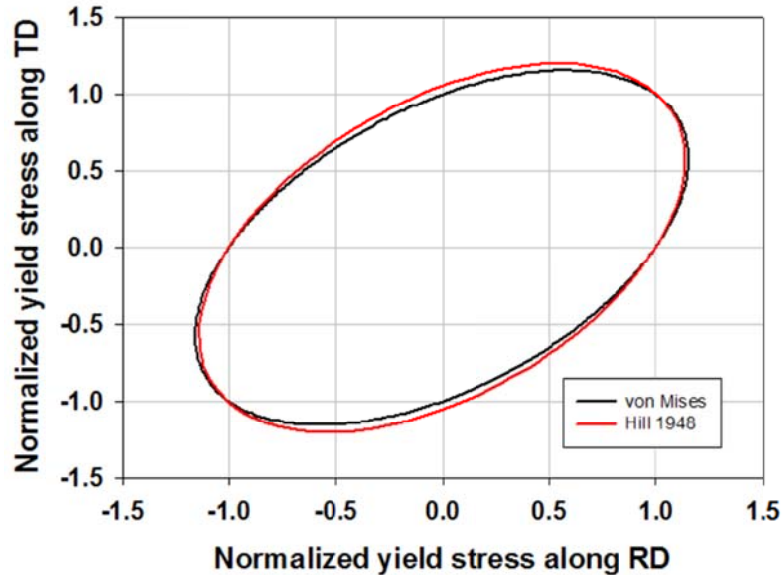


Figure 34 Comparison of Hill1948 and von Mises yield functions

### 3.2.2 Strain rate sensitivity

As for strain rate sensitivity, the strain rate sensitivity exponent (the average  $m$ -value) of the power law type was measured through the simple tension test along the rolling direction with four tensile speeds, 0.05, 0.5, 5.0 and 50.0 mm/s, which were approximately assumed to be strain rates of 0.001, 0.01, 0.1 and 1.0 /s, respectively, considering the 50.0 mm gage length. Based on measured hardening curves, the strain rate sensitivity exponent was calculated as (3.1.1). Strain rate sensitivity variations for the four strain rates were plotted in Figure 35 and the average strain rate sensitivity exponent was listed in Table 6. For TWIP980, it showed the average negative  $m$ -value in power law type unlike HB780 and DP780.

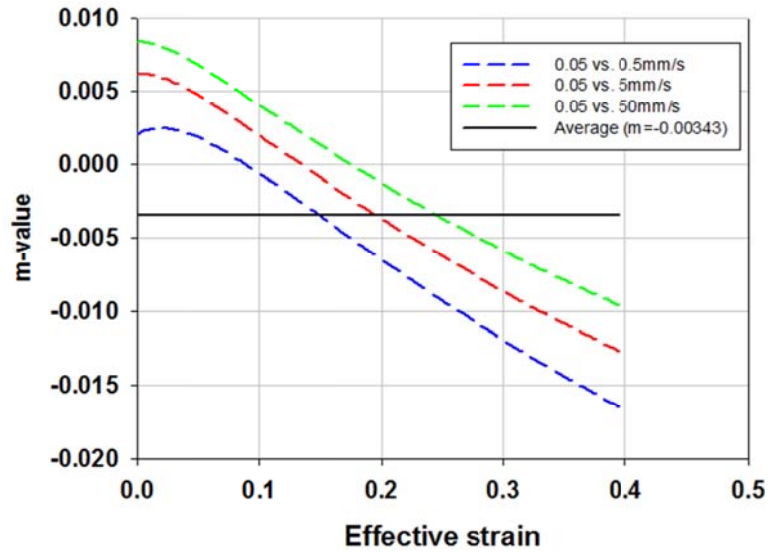


Figure 35 Strain rate sensitivity variation for four strain rates for TWIP980

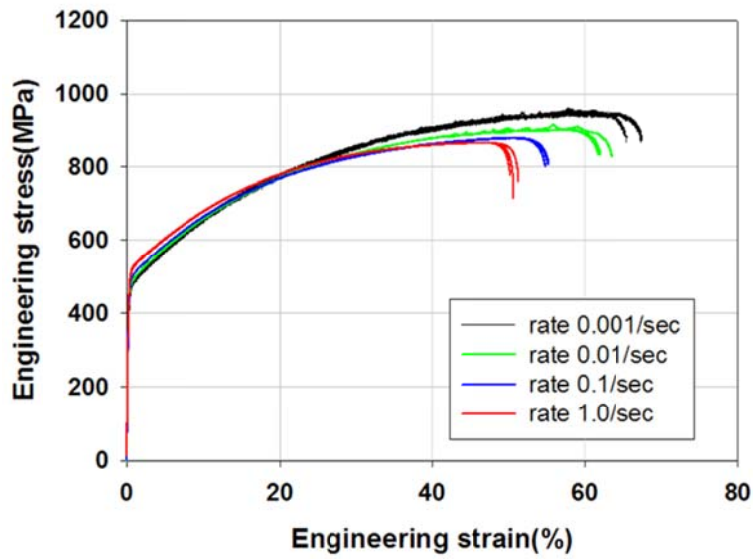


Figure 36 Engineering stress-engineering strain with four tensile speeds in the rolling direction ( $0^\circ$ ) for TWIP980

When the engineering stress-engineering strain curves with four tensile speeds in the rolling direction were compared as shown in Figure 36, the total elongation decreased considerably and the initial yield stress rose as the strain rate increased. The TWIP980 sheet showed poorer formability with increased strain rate, which the amount of decreased total elongation was almost 20 % by comparing between strain rates 0.001 and 1.0 /s. For more precise prediction of the formability of TWIP980, a new constitutive equation with strain rate sensitivity was developed. The new empirical constitutive equation of the following form was proposed:

$$\bar{\sigma} = f(\bar{\varepsilon}, \dot{\varepsilon})g(\dot{\varepsilon}) \quad (3.2.1)$$

where

$$f(\bar{\varepsilon}, \dot{\varepsilon}) = A_f (\bar{\varepsilon} + \bar{\varepsilon}_o)^n \quad (3.2.2)$$

$$\bar{\varepsilon}_o = B_f \exp\left(-C_f \left(\log_{10} \frac{\dot{\varepsilon}}{\dot{\varepsilon}_o}\right)^{D_f}\right) \quad (3.2.3)$$

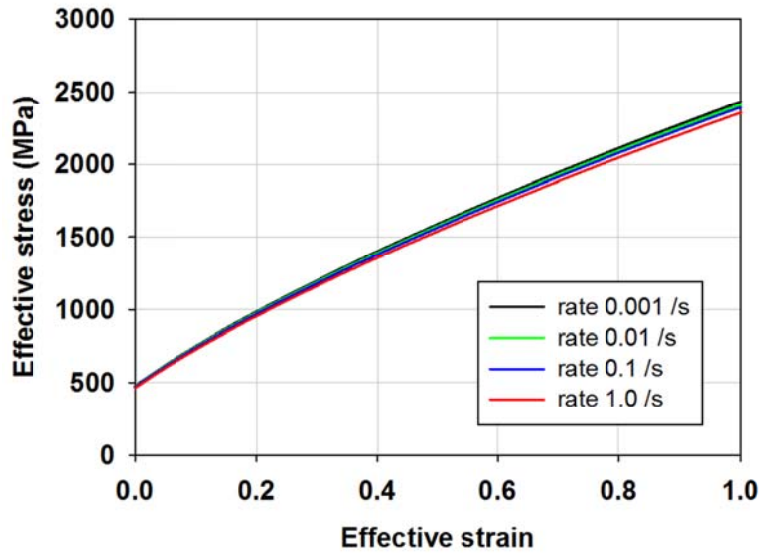
$$n = E_f \exp\left(-F_f \left(\log_{10} \frac{\dot{\varepsilon}}{\dot{\varepsilon}_o}\right)^{G_f}\right) \quad (3.2.4)$$

$$g(\dot{\varepsilon}) = \exp\left(A_g \left(\log_{10} \left(\frac{\dot{\varepsilon}}{\dot{\varepsilon}_o}\right)\right)^2 + B_g \log_{10} \left(\frac{\dot{\varepsilon}}{\dot{\varepsilon}_o}\right)\right) \quad (3.2.5)$$

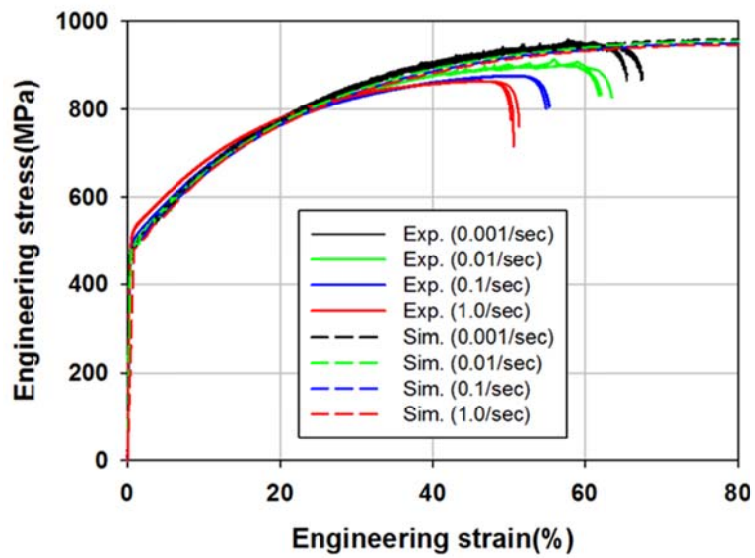
where  $A_f, B_f, C_f, D_f, E_f, F_f, A_g, B_g$  and  $C_g$  are hardening coefficients, which was listed in Table 8. The constitutive equation was utilized to numerical analysis for formability prediction. To validate the developed constitutive equation, numerical simulations were conducted for the simple tension test along the rolling direction with various strain rates utilizing the eight node 3-D continuum element (C3D8R) with the size of 0.2384 x 0.2384 x 0.2384 mm utilized in the center with Hill 1949 yield function. With the power law type hardening for each strain rate, the numerical simulation cannot describe the measured engineering stress-engineering strain data as shown in Figure 37. As for the new developed constitutive equation, its hardening curves with various strain rates describing the crossover curves well predicted the experimentally obtained hardening in Figure 38 (a) and the numerical simulation results showed good agreement with the experiment results as shown in Figure 38 (b).

Table 8 Hardening coefficients for the new developed empirical constitutive law

$A_f$	$A_f$	$A_f$	$A_f$	$A_f$	$A_f$
2253.0	01145	0.1195	0.6473	0.7164	0.1024
$A_g$	$B_g$	$C_g$			
0.7993	0.0097	-0.0768			

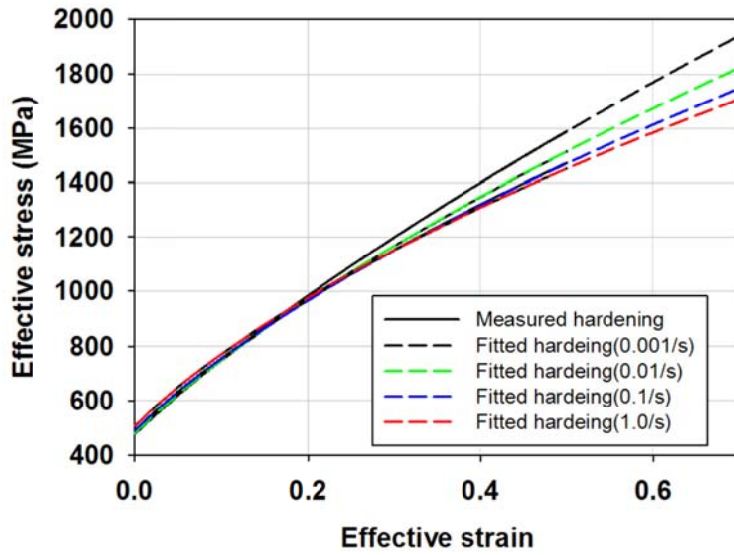


(a)

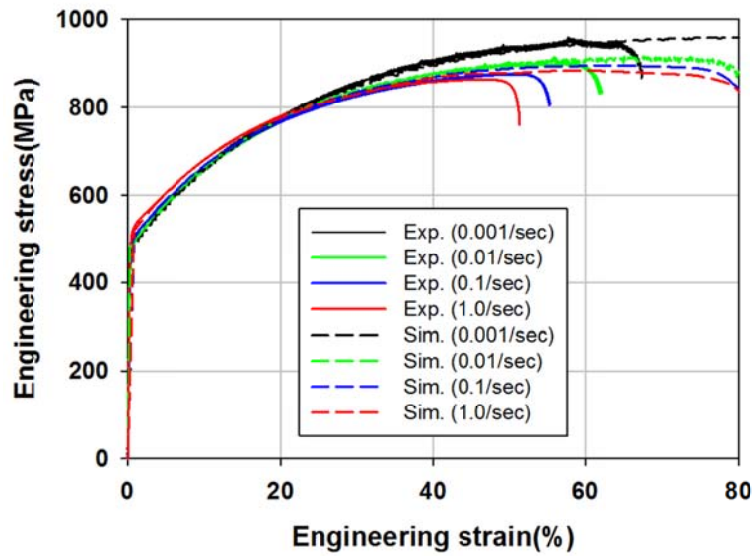


(b)

Figure 37 (a) The power law type hardening with various strain rates (b) comparison the experiment and simulation results



(a)



(b)

Figure 38 (a) The new developed hardening with various strain rates (b) comparison the experiment and simulation results

### 3.2.3 Fracture test

In this work, three different fracture specimens shapes developed by (Seok et al., 2015) as shown in Figure 39 were utilized to characterize the fracture criterion to obtain various deformation modes with the simple tension specimen. In (Seok et al., 2015), the developed characterization was focused on the non-negative stress triaxiality region with dealing with the thinning deformation mode which is important for failure in real part drawing. As done for the simple tension test, tensile tests for the two kinds of round notch and shear specimens were conducted using the universal testing machine (Instron 8801). Moreover, to characterize the strain rate dependent fracture criterion, all tensile tests were conducted with various strain rates. The tensile speeds for each specimen were determined by numerical simulation checking the strain rate of center element of specimen. As for the round notch I, for along the rolling direction with four tensile speeds, 0.02, 0.2, 2.0 and 20.0 mm/s were approximately assumed to be strain rates of 0.001, 0.01, 0.1 and 1.0 /s, respectively. Also, four tensile speeds, 0.01, 0.1, 1.0 and 10.0 mm/s for round notch II and 0.05, 0.5, 5.0 and 50.0 mm/s for shear were conducted, which were approximately assumed to be strain rates of 0.001, 0.01, 0.1 and 1.0 /s, respectively. The punch force-displacement results were shown in Figure 40 - Figure 42 and the specimens after failure were shown in Figure 43.

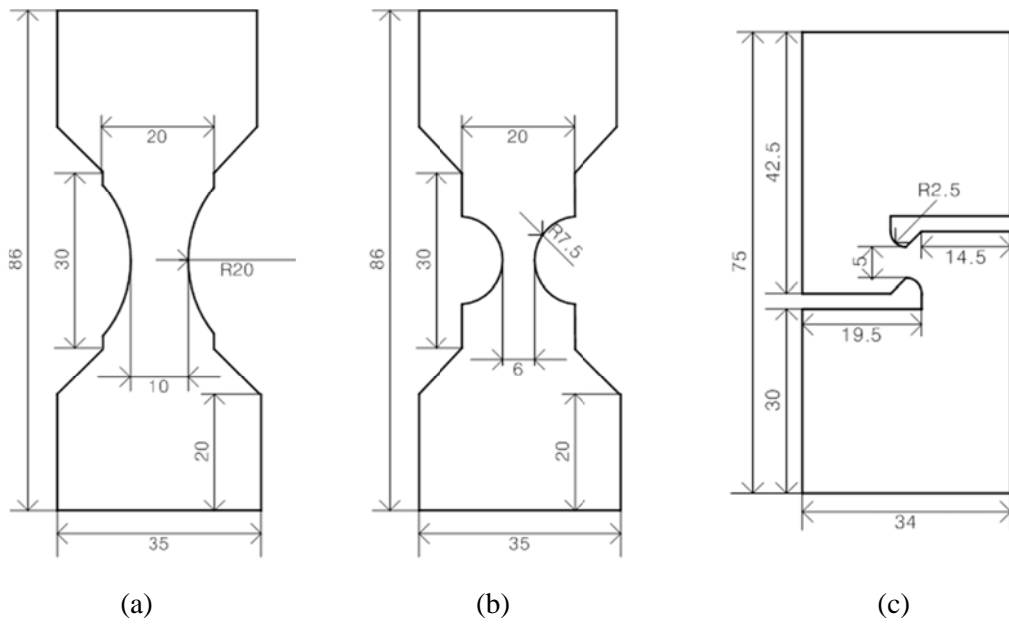


Figure 39 The dimension of specimens (unit: mm): (a) round notch I (b) round notch II (c) shear

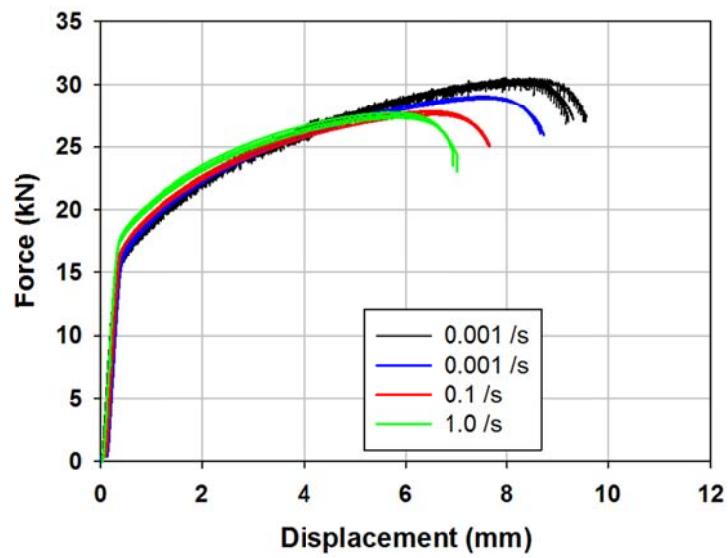


Figure 40 The experiment punch force and displacement data for round notch I

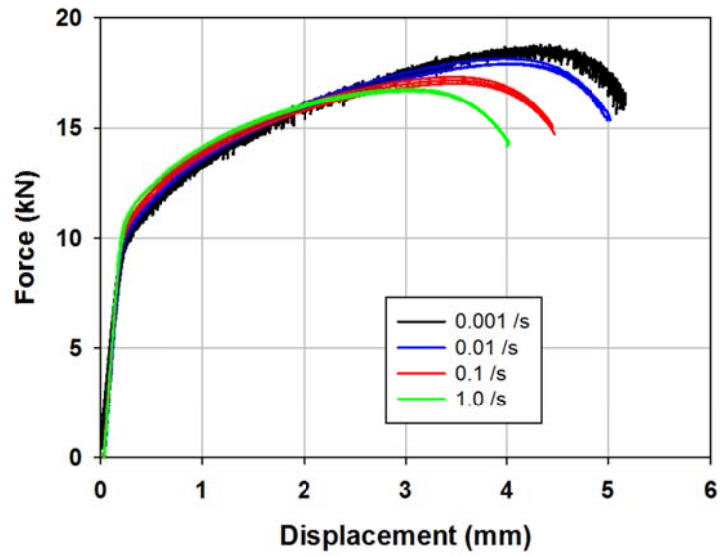


Figure 41 The experiment punch force and displacement data for round notch II

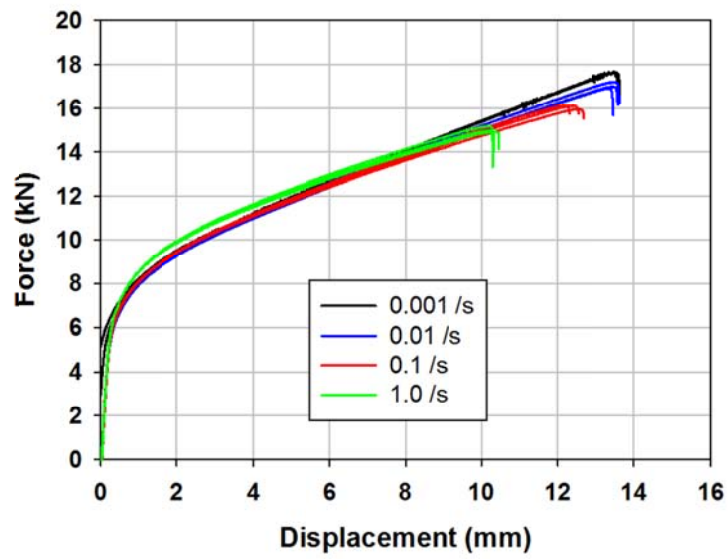


Figure 42 The experiment punch force and displacement data for shear

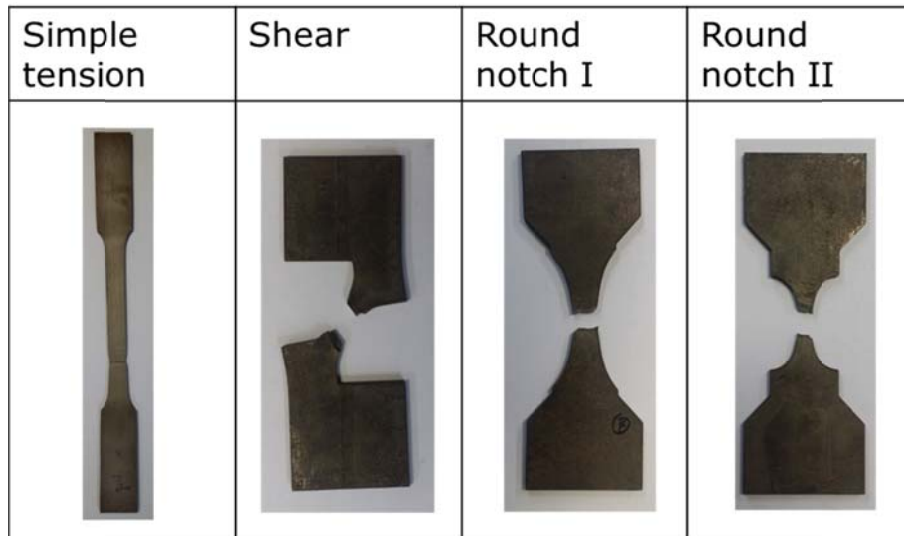
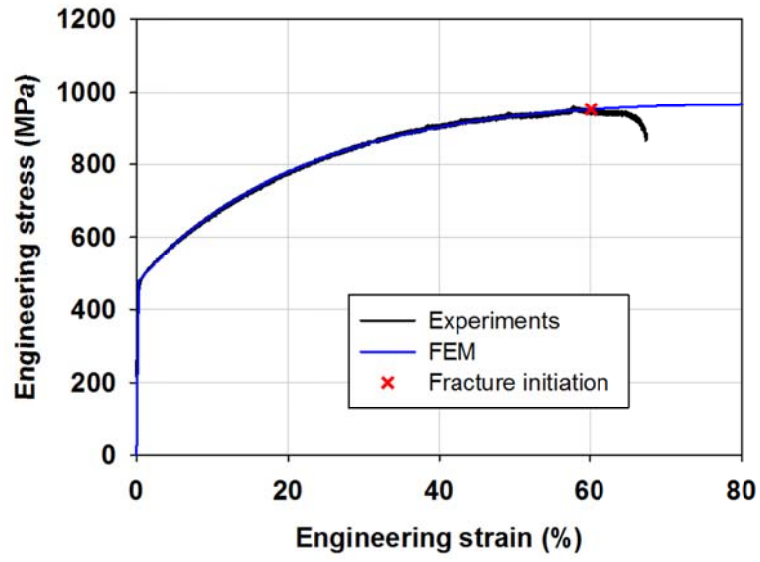


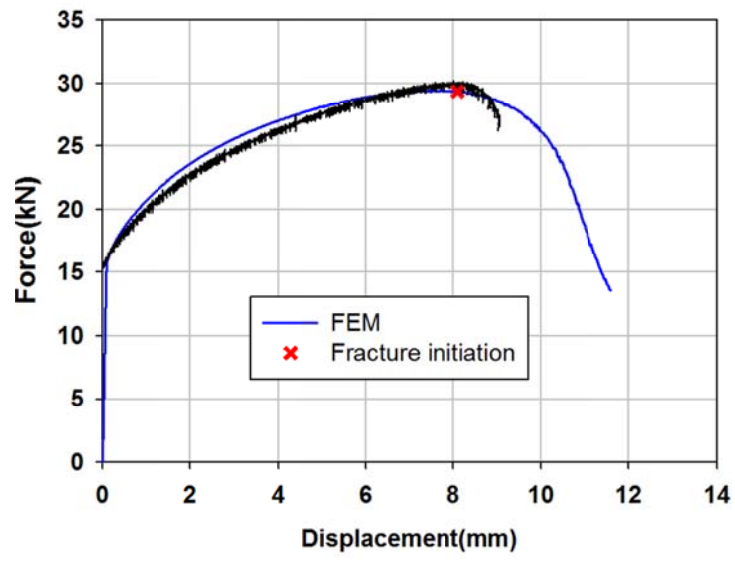
Figure 43 Fractured specimens

### 3.2.4 Triaxiality and strain rate dependent fracture criterion

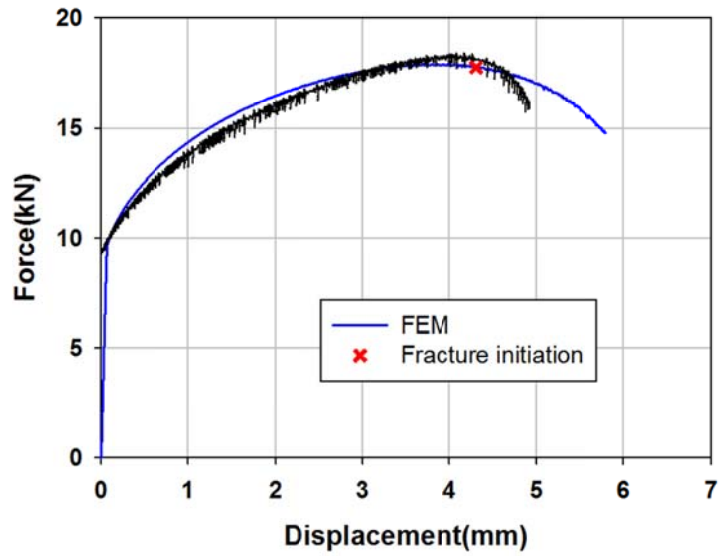
For the characterization of fracture criterion based on the experiments, the numerical analysis was conducted. For numerical simulations, ABAQUS/Explicit (ABAQUS, 2007) was applied, utilizing the eight node 3-D continuum element (C3D8R) with the size of 0.2384 x 0.2384 x 0.2384 mm in the center region which is the critical region for fracture. To save the computational time, the one eighth of the specimen model simulation was performed considering the symmetry of the specimen geometry, loading condition and material properties. Hill 1948 yield function with the new developed constitutive law obtained in previous sections was utilized in simulation. The simulation results with experimental results were shown in Figure 44 - Figure 47.



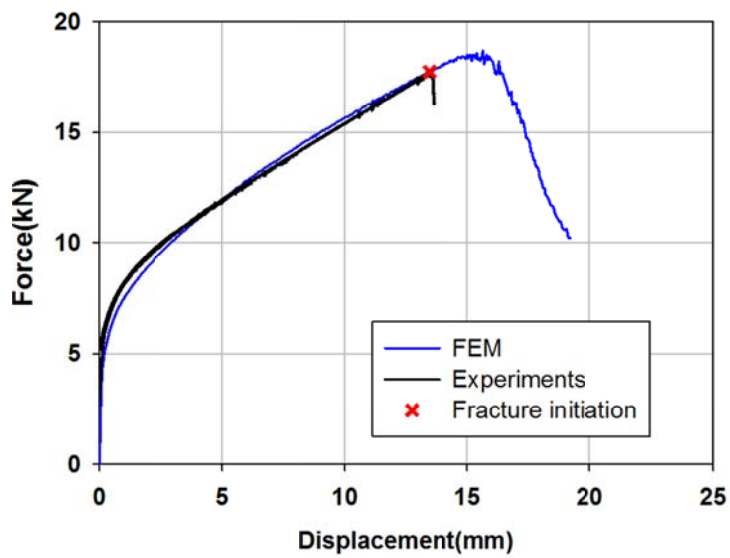
(a)



(b)

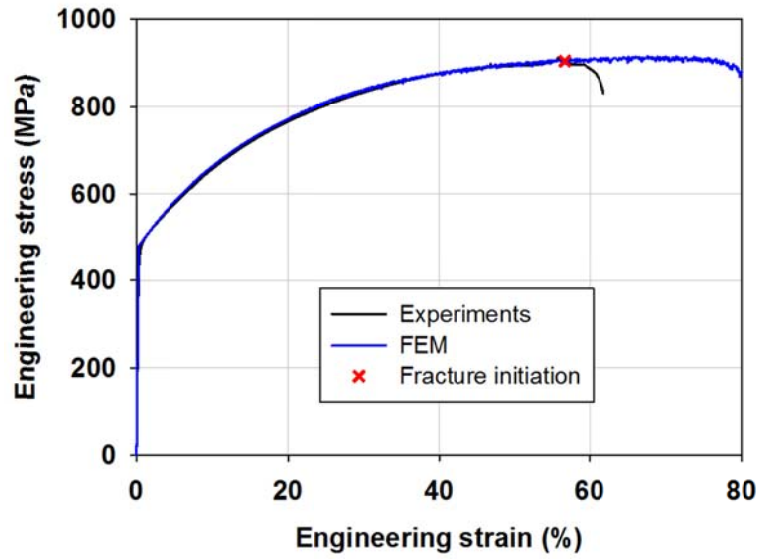


(c)

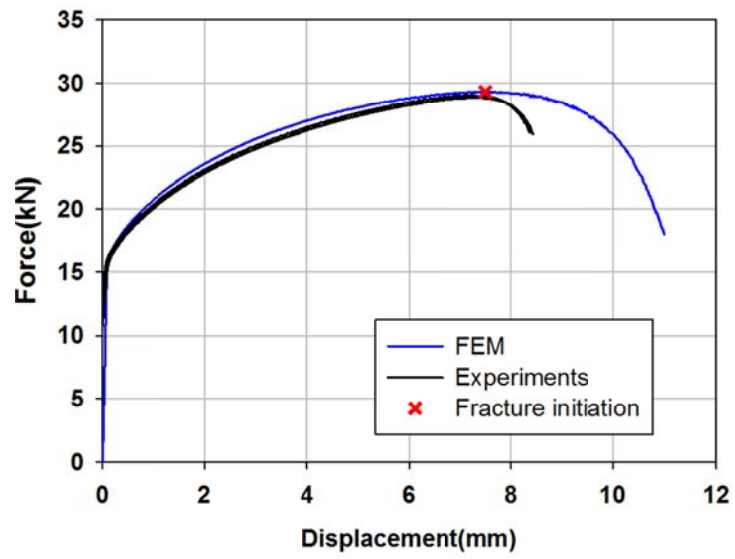


(d)

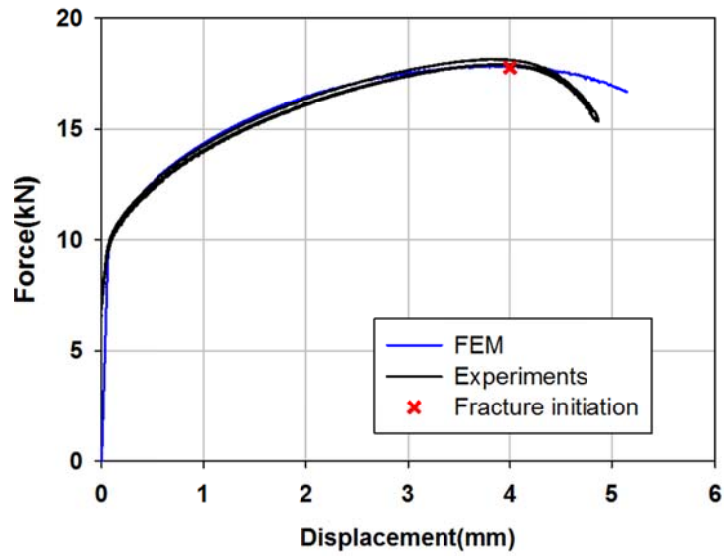
Figure 44 Punch force and displacement for four fracture tests at 0.001 /sec: (a) simple tension (b) round notch I (c) round notch II (d) shear



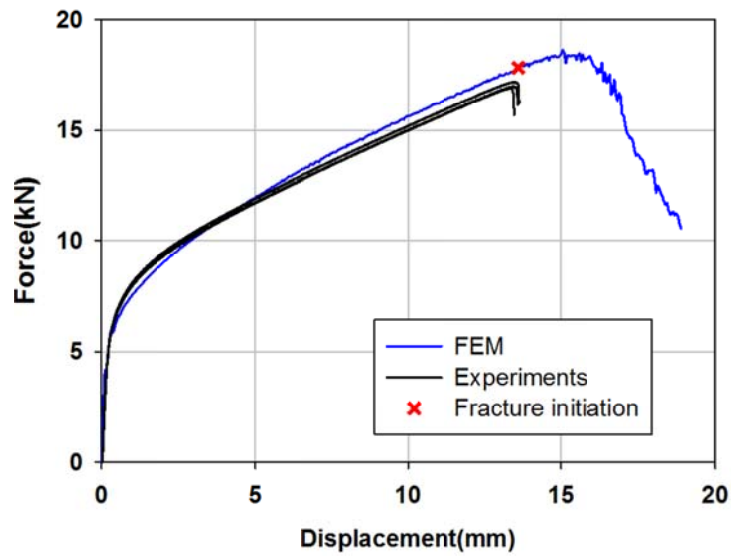
(a)



(b)

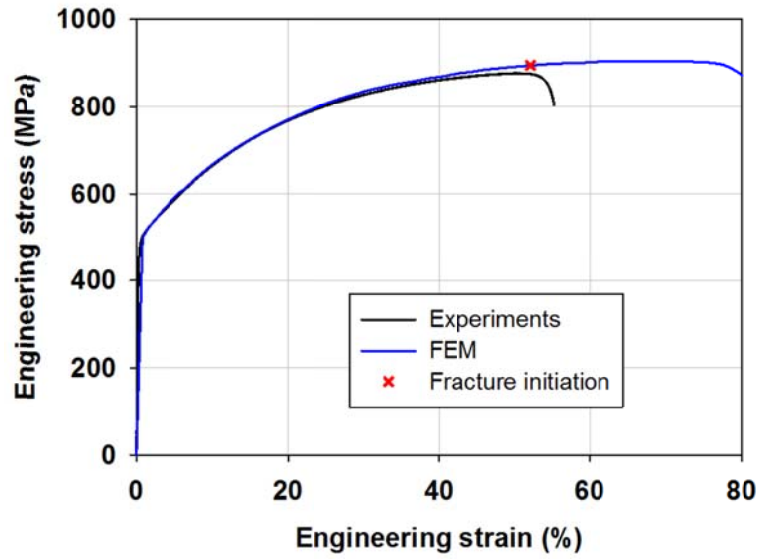


(c)

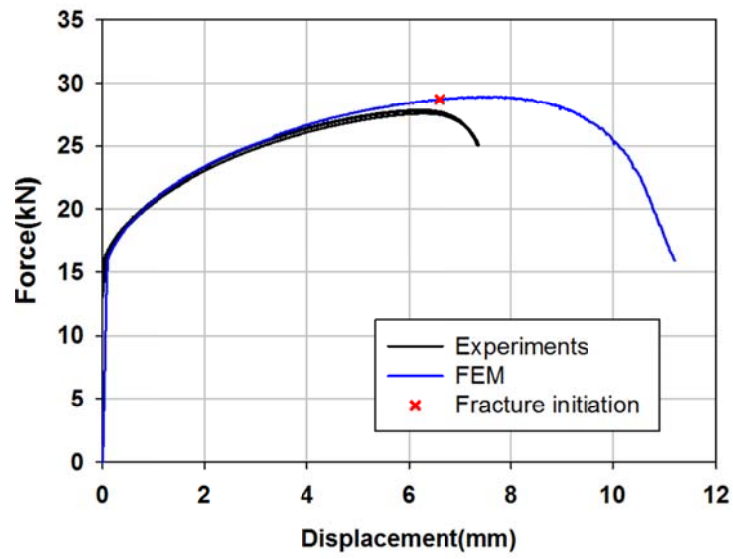


(d)

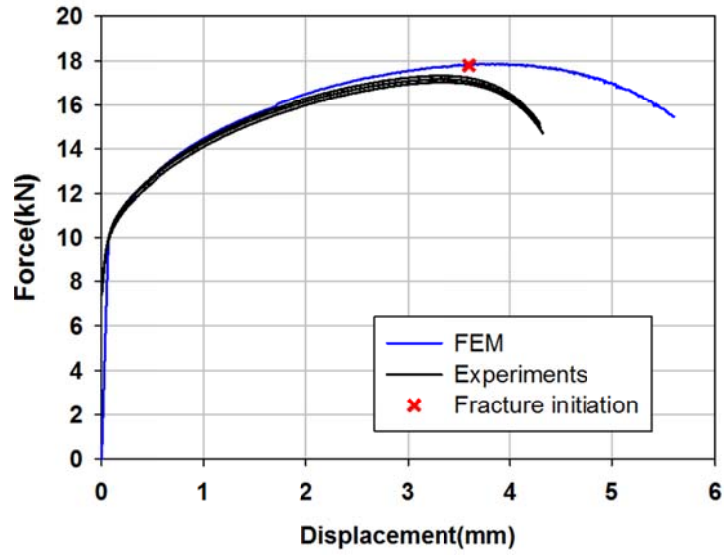
Figure 45 Punch force and displacement for four fracture tests at 0.01 /sec: (a) simple tension (b) round notch I (c) round notch II (d) shear



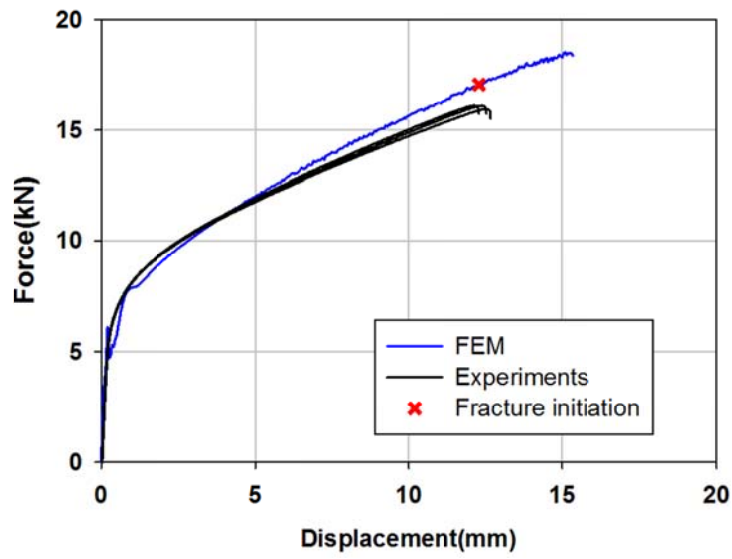
(a)



(b)

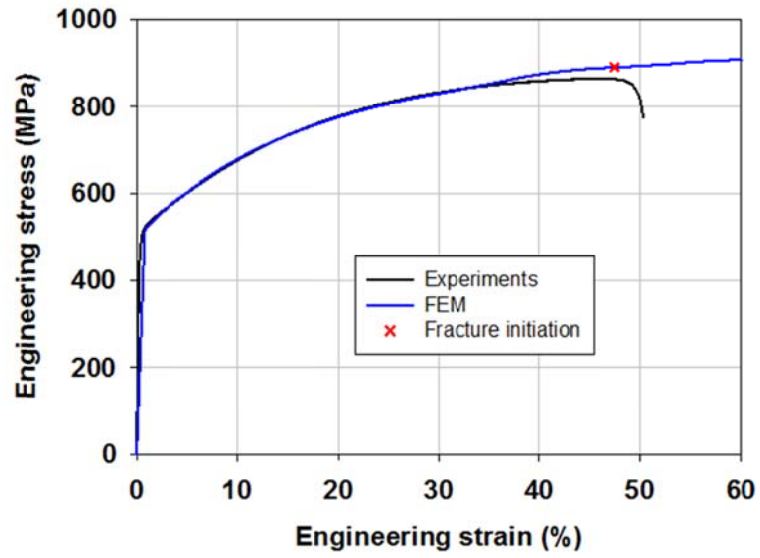


(c)

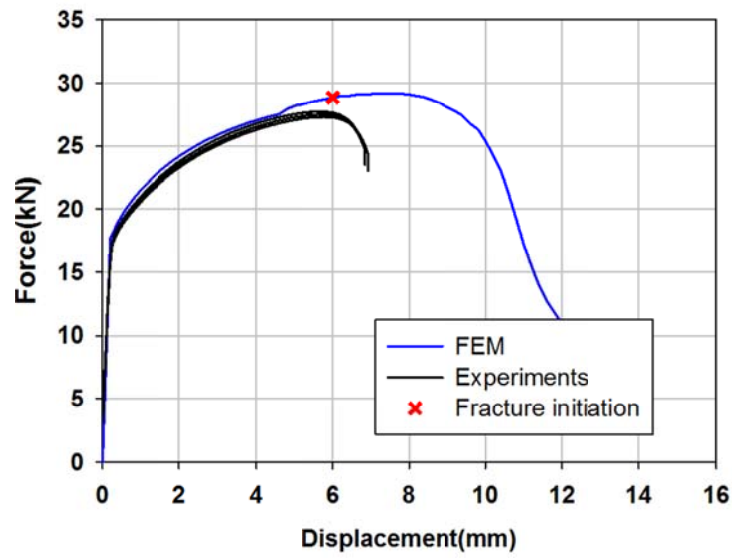


(d)

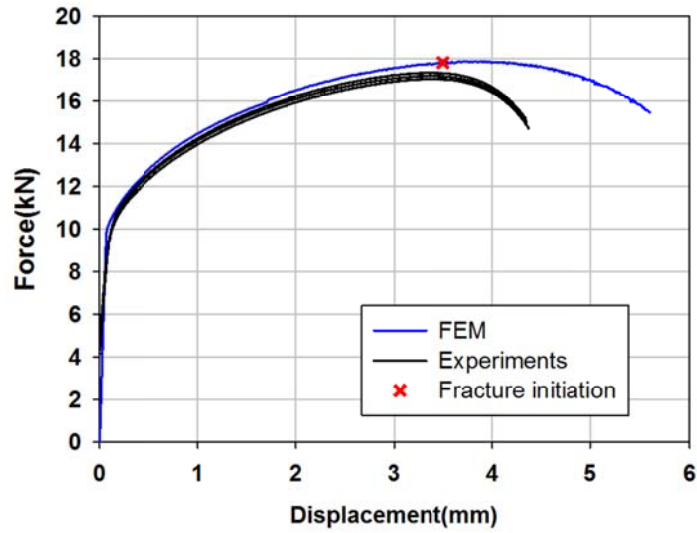
Figure 46 Punch force and displacement for four fracture tests at 0.1 /sec: (a) simple tension (b) round notch I (c) round notch II (d) shear



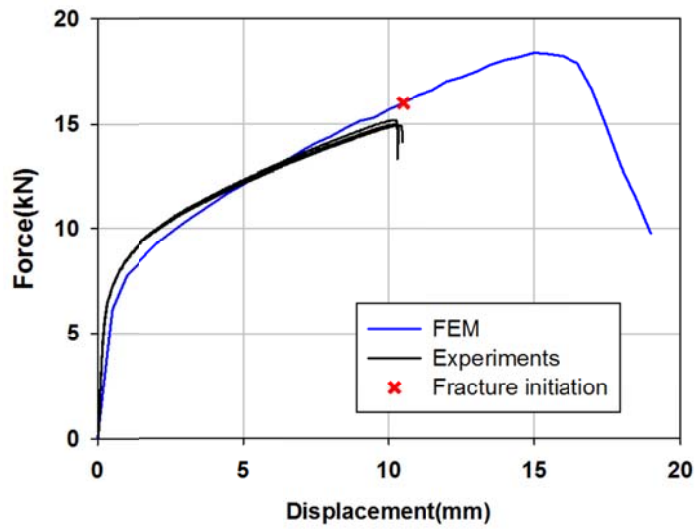
(a)



(b)



(c)



(d)

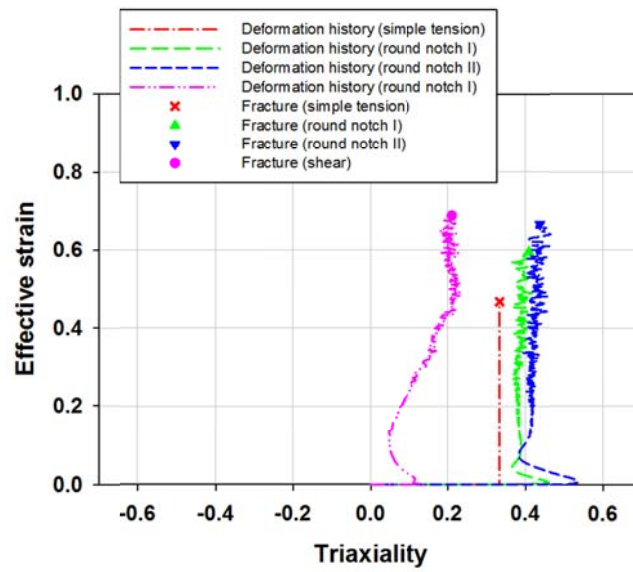
Figure 47 Punch force and displacement for four fracture tests at 1.0 /sec: (a) simple tension (b) round notch I (c) round notch II (d) shear

By conducting the simulation, the fracture initiation was determined by the maximum force condition in the experiment. The critical element, which was the center of the specimen and would have fracture with the largest effective strain, and the accumulative were identified for all fracture tests. The deformation history of stress triaxiality and the accumulative strain of the critical element for each test until the fracture were shown in Figure 48. The path of deformation in simple, round notch I and round notch II was changed moderately. Although the uniform path change of stress triaxiality for each test was well maintained except the shear test by fracture,  $\bar{\varepsilon}_F(\eta)$  for (2.1.10) was iteratively determined, assuming that

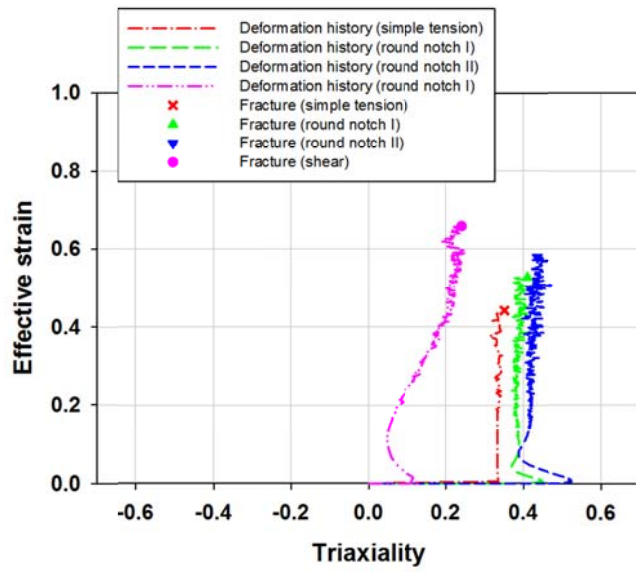
$$\bar{\varepsilon}_F(\eta) = \begin{cases} a\eta^2 + b\eta + c & \text{for } \eta \geq 1/3 \\ j(\eta - 1/3)^2 + k & \text{for } \eta \leq 1/3 \end{cases} \quad (3.2.6)$$

where a, b, c, j and k are constant coefficients for fracture criterion. To cover the various zones in the thinning mode assuming the plane stress condition, the stress triaxiality zone was divided into two zones. One is between the simple tension with  $\eta = 1/3$  and balanced biaxial stress states with  $\eta = 2/3$ , the other is between the simple tension with  $\eta = 1/3$  and the in-plane shear stress  $\eta = 0$ . The constant coefficients for fracture criterion in (3.2.6) were determined using the deformation history obtained by fracture tests in Figure 48. They were tried out iteratively until the fracture condition ( $\omega = 1$ ) was satisfied simultaneously in each zone. In addition, the continuity condition at  $\eta = 1/3$  was applied for the coefficients, j and k which were iteratively calibrated based on the deformation path of shear in Figure 48. The coefficients of fracture criterion were listed in Table 9. In Figure 49, the deformation

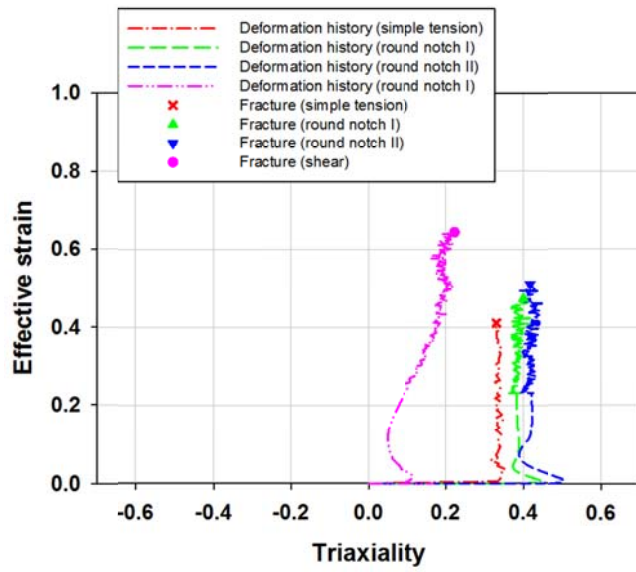
histories and the apparent effective fracture strains for the four tests were also plotted. For considering the strain rate dependency, based on the stress triaxiality fracture criterion with various strain rates obtained fracture tests, they were interpolated in terms of strain rate as shown in Figure 50.



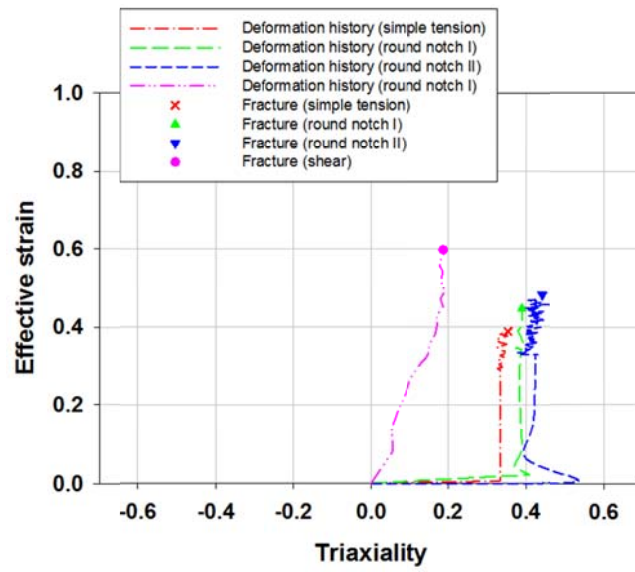
(a)



(b)

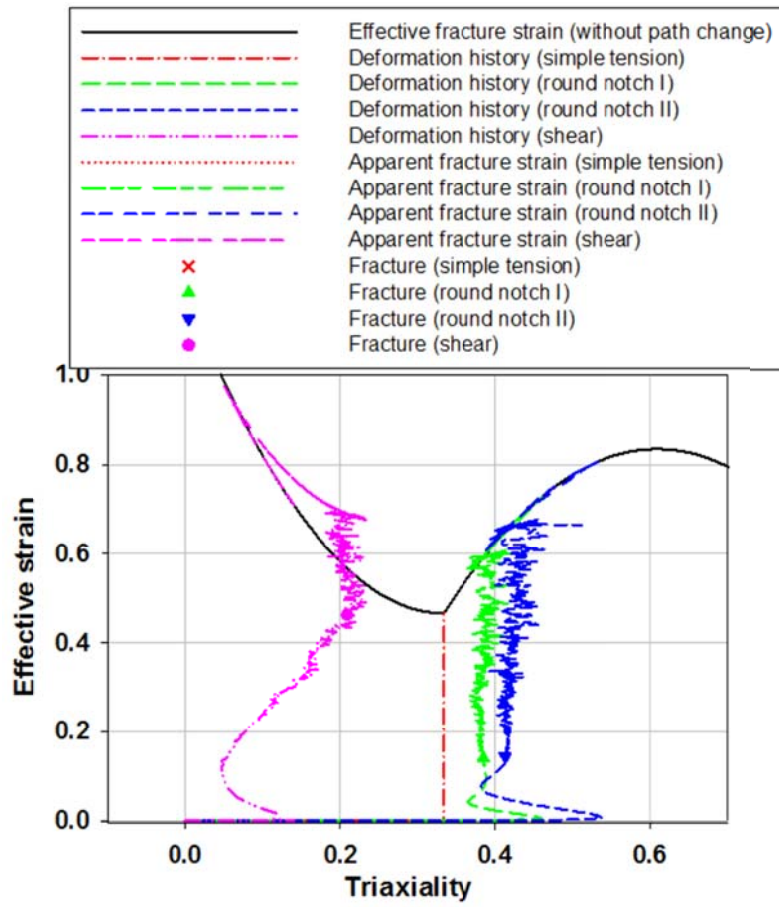


(c)

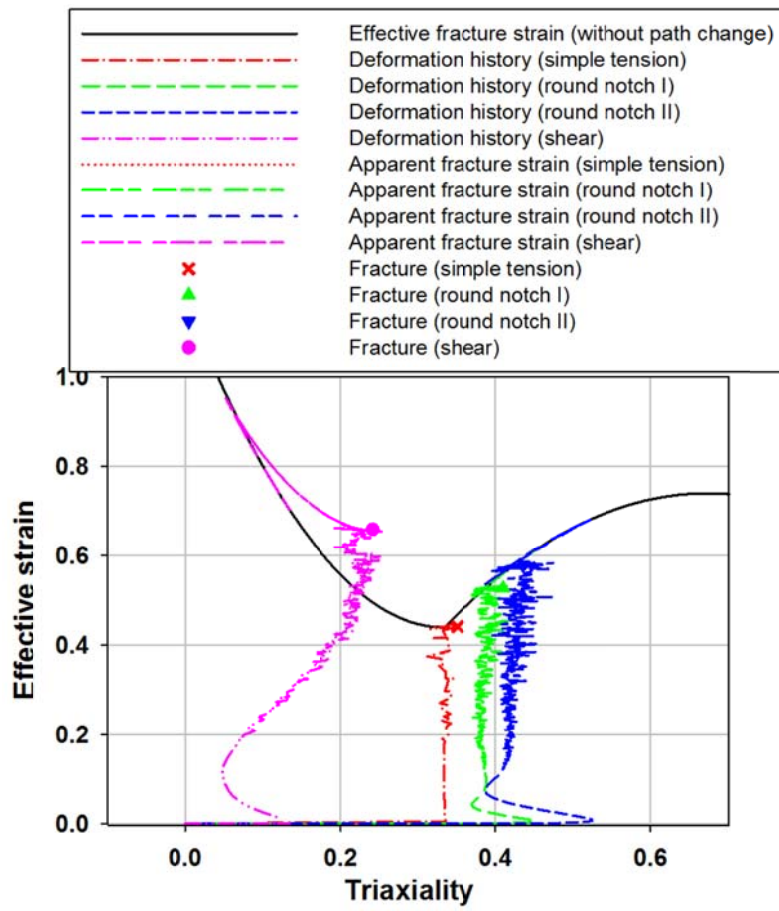


(d)

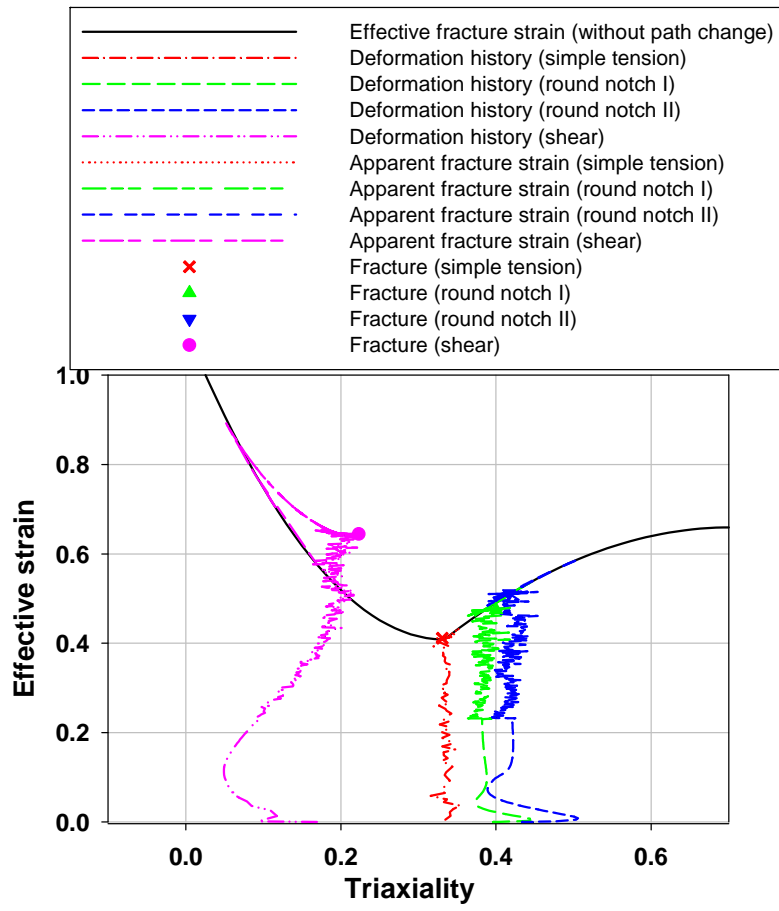
Figure 48 Deformation histories of critical elements for the fracture tests simulation:  
(a) 0.001/sec (b) 0.01/sec (c) 0.1/sec (d) 1.0/sec



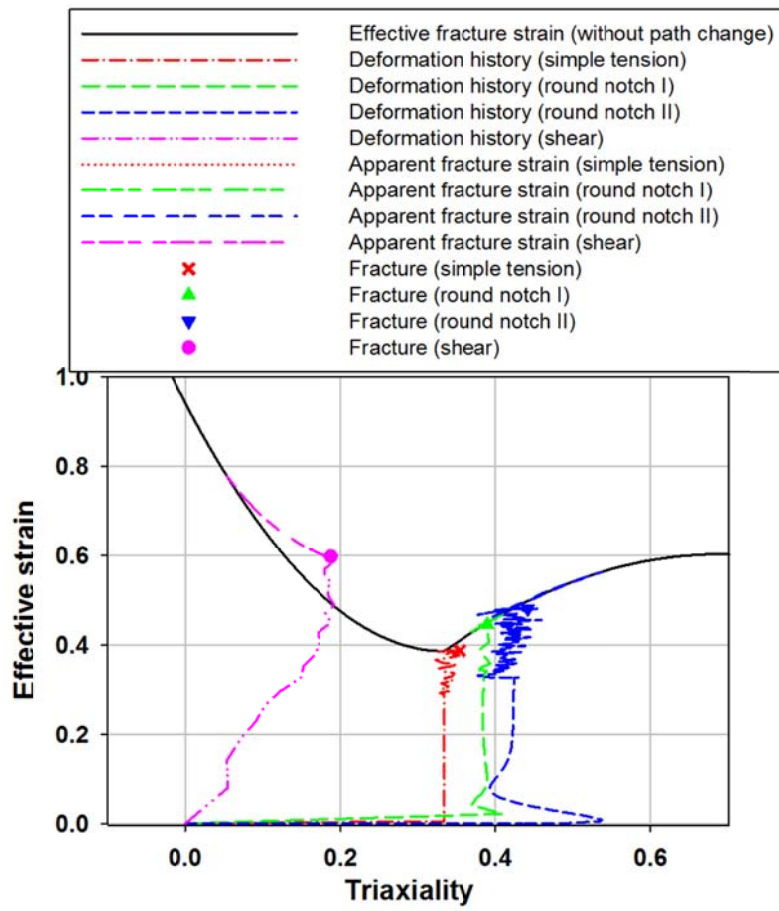
(a)



(b)



(c)



(d)

Figure 49 Stress triaxiality-dependent fracture criterion: (a) 0.001/sec (b) 0.01/sec (c) 0.1/sec (d) 1.0/sec

Table 9 Coefficients of the stress triaxiality dependent fracture criterion

Strain rate	a	b	c	j	k
0.001/sec	-4.8360	5.8936	-0.9612	6.4575	0.4660
0.01/sec	-2.6082	3.5103	-0.4412	6.6115	0.4391
0.1/sec	-0.3371	1.0373	0.1813	3.1929	0.4897
1.0/sec	-1.7133	2.3607	-0.2104	5.0067	0.3861

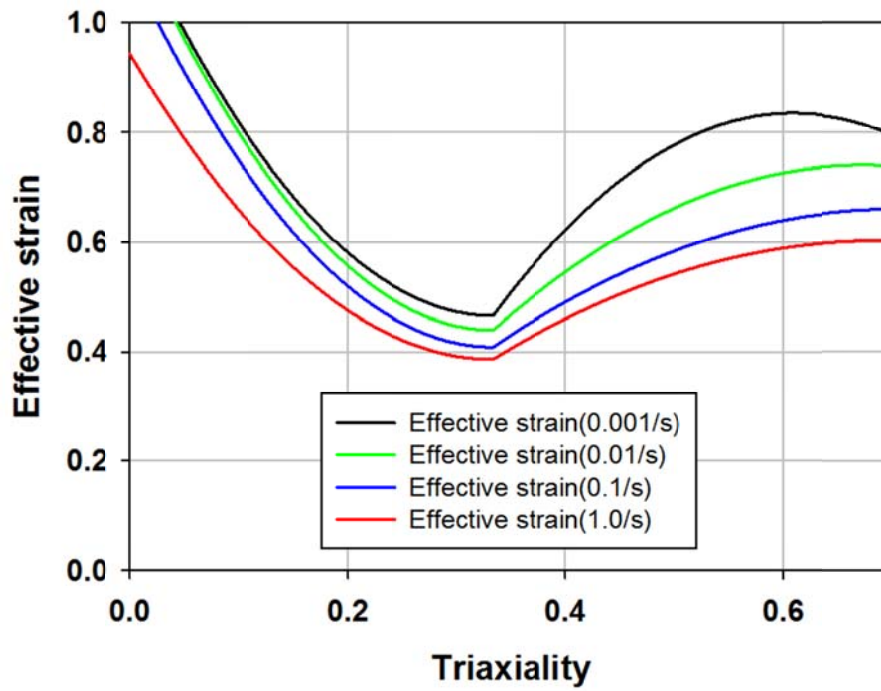


Figure 50 Stress triaxiality and strain dependent fracture criterion

## 4. Validation

For application and validation of the newly developed numerical procedure and material properties characterized for two advanced high strength hot-rolled steel sheets for failure with strain localization, experiments and numerical simulations were carried out for the circular cup drawing test for HB780 and DP780 (Kim et al., 2016). The test was performed using the 50 ton double action hydraulic type press as schematically shown in Figure 51. The punch speed was 108 mm/min and the blank holding force was 50 kN. The beef tallow was used as a lubricant to reduce the contact friction between the punch and the blank, while a lubricant was not utilized for the blank/die and the blank/holder. The circular cup drawing test specimens with 4 different diameters from 102.5 to 110.0 mm with the interval of 2.5 mm were prepared by wire cutting. When the diameter of specimens was 102.5 mm, forming was completed without failure for HB780 and DP780, but failure occurred on around the punch radius corner regardless of material directions for both samples with severe strain localization for all other cases as shown in Figure 52.

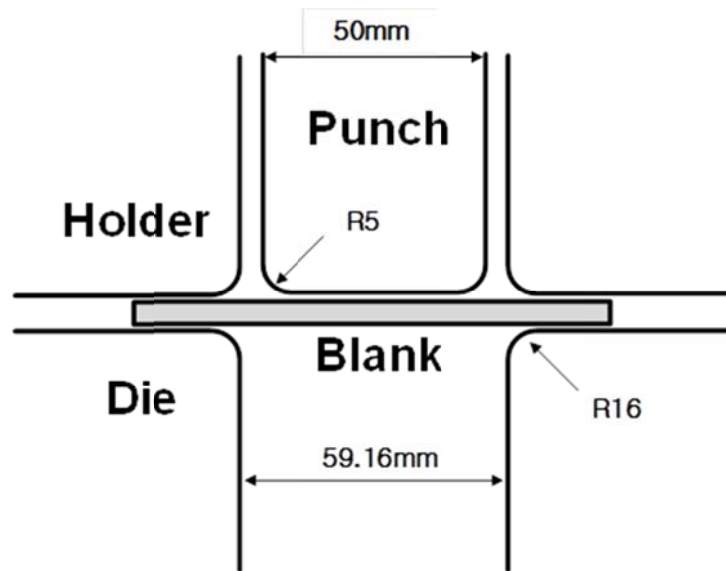


Figure 51 Schematic view of the cylindrical cup drawing test with dimensions



(a)



(b)

Figure 52 Circular cup drawing test results: (a) HB780 (b) DP780

Numerical simulations with properly calibrated hardening, strain rate sensitivity and non-quadratic yield functions without any formability criterion were carried out for the circular blank with the diameter of 102.5 and 105.0 mm. The eight node 3-D continuum element (C3D8R) with the cubic shape of 0.2636 x 0.2636 x 0.2636 mm was utilized in the blank except for the center region with coarse meshes. Eleven layers were utilized through the thickness of 2.9 mm for blanks. The rigid element (R3D4) was applied for the tools. As for friction, two friction coefficients were assumed: 0.1 for the blank/punch and 0.15 for the blank/die and the blank/holder. Simulations were carried out only for a quarter of the blank considering symmetry. Furthermore, for comparison purposes, the practice commonly applied for rather thin cold-rolled sheets was performed utilizing shell elements with the FLD criterion to determine failure, along with extrapolated hardening without rate sensitivity and the Hill quadratic anisotropic yield function. Note that, besides the strain-based forming limit diagram

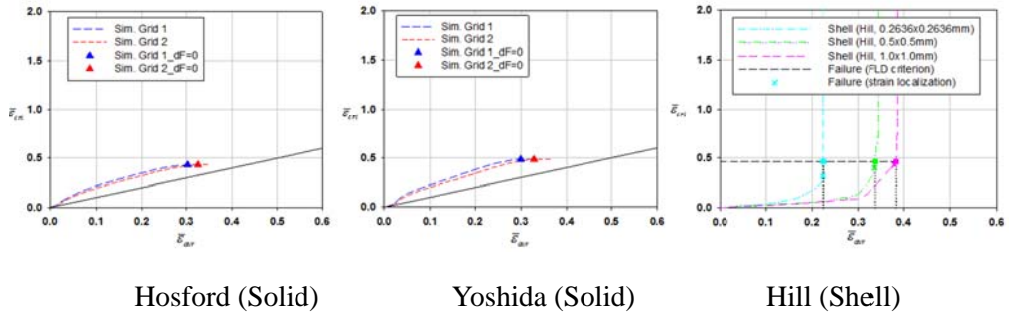
obtained from the FLD test and imposed to the critical element for its failure by strain localization, the new criterion to monitor strain localization was also applied for comparison. To understand the mesh size effect, three mesh sizes were tried out for shell elements: 0.2636 x 0.2636, 0.5 x 0.5 and 1.0 x 1.0 mm.

The simulated results of the Hosford and Yoshida yield functions showed that strain localization to induce failure did not develop for the 102.5 mm blank of both samples, complying with experimentally confirmed complete cup drawing without failure, and simulated force-displacement curves also well matched with experiments as shown in Figure 53 and Figure 54. The simulated results of both yield functions showed that failure with strain localization for the 105.0 mm blank of both samples, complying with experimentally confirmed cup drawing failure, and simulated force-displacement curves also well matched with experiments as shown in Figure 55 and Figure 56. Performance of the Hosford and Yoshida yield functions was virtually the same.

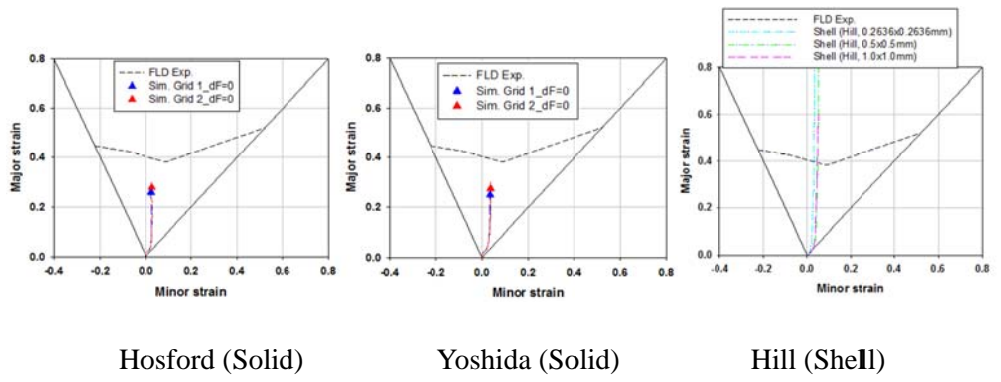
The shapes of the successfully completed cups having four ears for both samples were shown in Figure 57 for the experimental and simulation results, respectively. To examine the earing and cup height, the earing profiles of the simulation with the Hosford and Yoshida yield function after the cup drawing test were compared with the experiment, which was averaged for three tests, in Figure 58. In the simulation results of the anisotropic Yoshida yield function for both samples, the earing occurred in the direction of every 45 degrees with four ears, which were the same with the experimental results, while the isotropic Hosford yield function cannot account for the earing. In terms of the cup height, the earing profiles with the Yoshida yield function

showed good agreement with the experimental results for both samples. For the fracture site in case of the 105.0 mm diameter blanks for both samples, the simulation results with the Hosford and Yoshida function were in accordance with the experiments as shown in Figure 59.

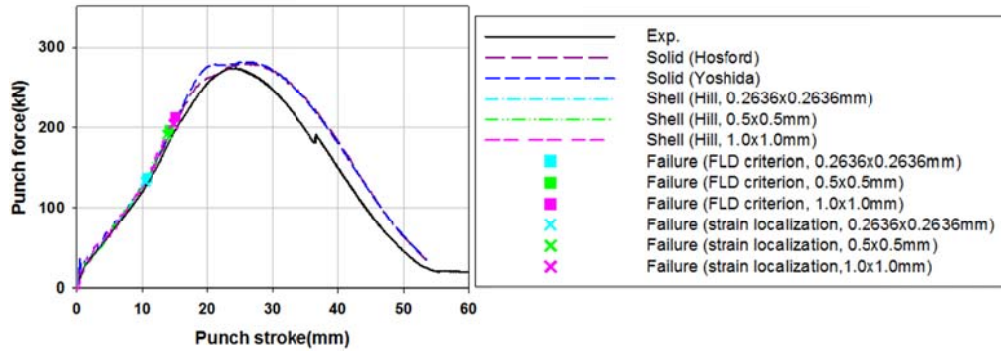
The common practice based on shells elements simulated failure with strain localization for both 102.5 and 105.0 mm blanks of both samples as shown in Figure 53-Figure 56, regardless of the failure criteria and mesh sizes applied, confirming that using shell elements promoted early strain localization for the hot-rolled sheets. As meshes of shell elements became coarser, strain localization was delayed but the typical coarse mesh size of the common practice with 1.0 x 1.0 mm still simulated failure by strain localization for both 102.5 and 105.0 mm blanks of both samples. As for the failure criterion effect, the new criterion monitoring strain localization and the FLD based criterion did not make difference in results because of the premature strain localization by shell elements.



(a)

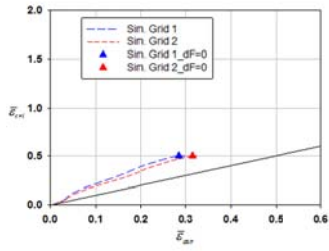


(b)

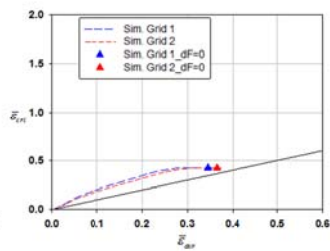


(c)

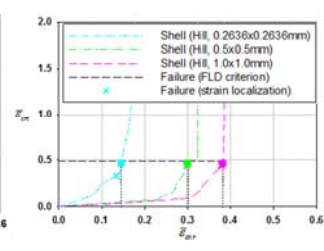
Figure 53 Circular cup drawing simulation results of HB780 with 102.5 mm diameter:  
 (a) effective strain ratio between the critical and neighboring elements (b) strain-based FLD (c) force-displacement curve



Hosford (Solid)

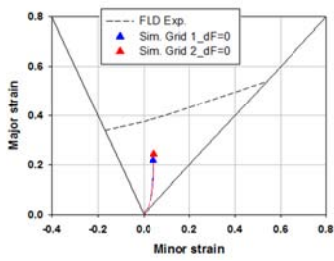


Yoshida (Solid)

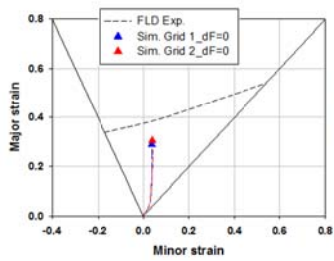


Hill (Shell)

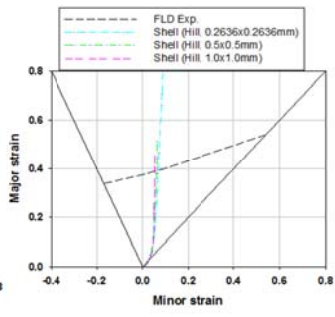
(a)



Hosford (Solid)

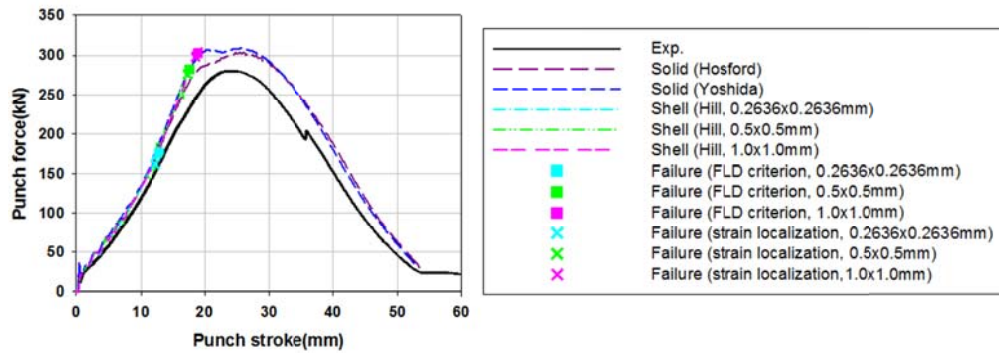


Yoshida (Solid)



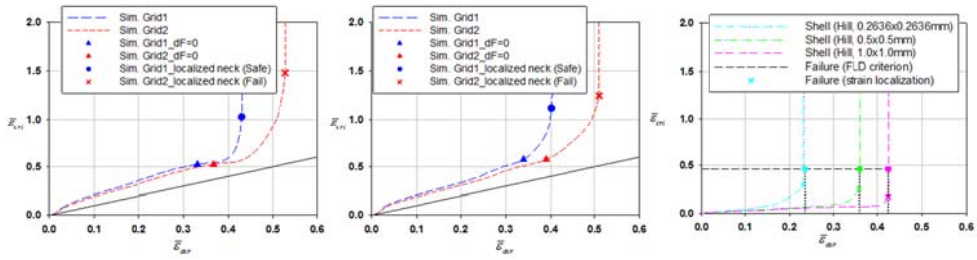
Hill (Shell)

(b)

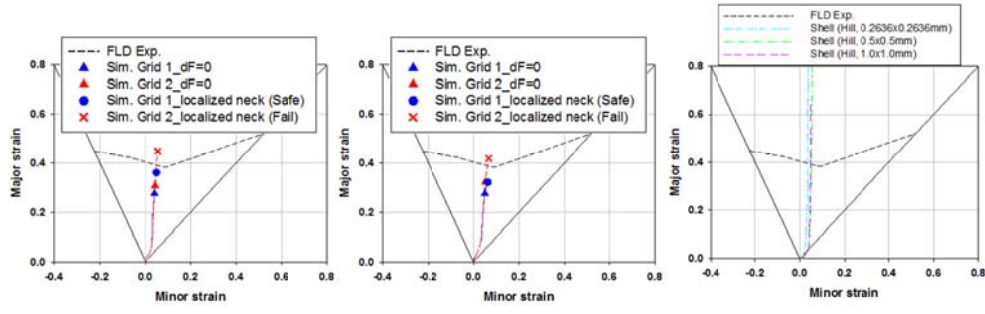


(c)

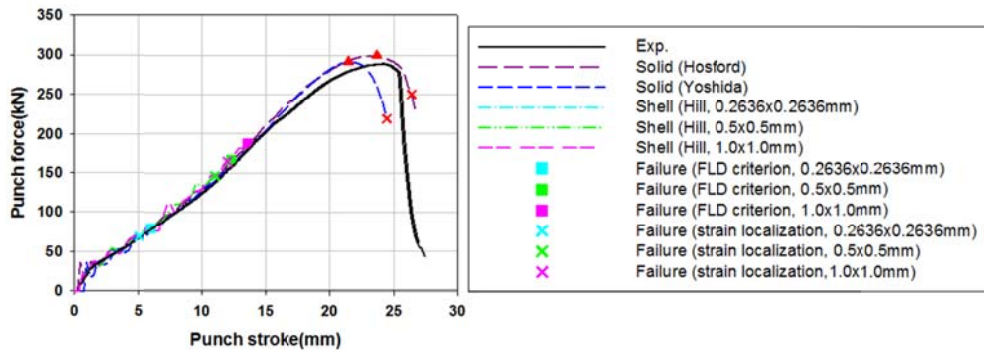
Figure 54 Circular cup drawing simulation results of DP780 with 102.5 mm diameter: (a) effective strain ratio between the critical and neighboring elements (b) strain-based FLD (c) force-displacement curve



(a)

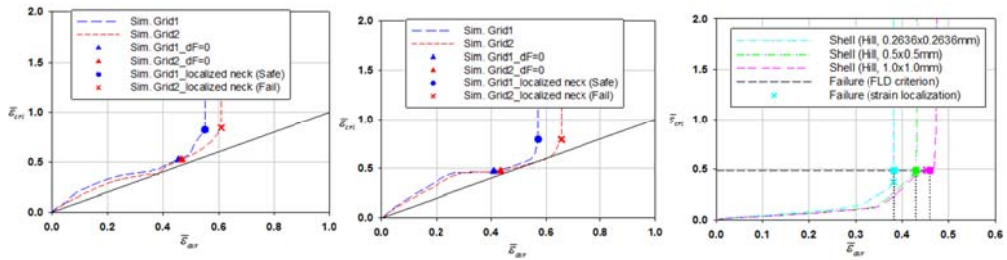


(b)



(c)

Figure 55 Circular cup drawing simulation results of HB780 with 105.0 mm diameter:  
 (a) effective strain ratio between the critical and neighboring elements (b) strain-based FLD (c) force-displacement curve

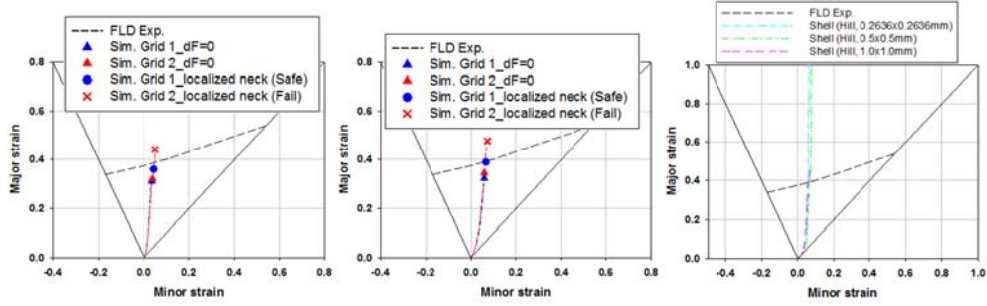


Hosford (Solid)

Yoshida (Solid)

Hill (Shell)

(a)

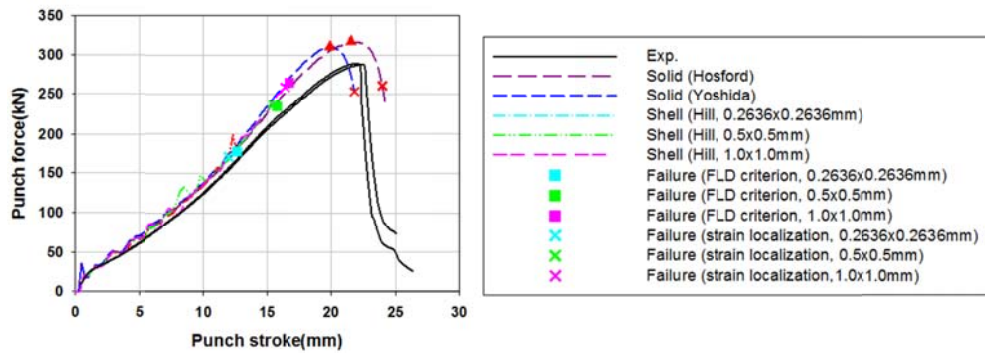


Hosford (Solid)

Yoshida (Solid)

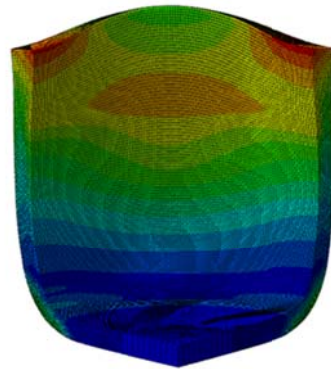
Hill (Shell)

(b)

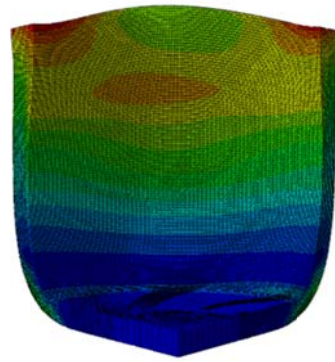


(c)

Figure 56 Circular cup drawing simulation results of DP780 with 105.0 mm diameter: (a) effective strain ratio between the critical and neighboring elements (b) strain-based FLD (c) force-displacement curve

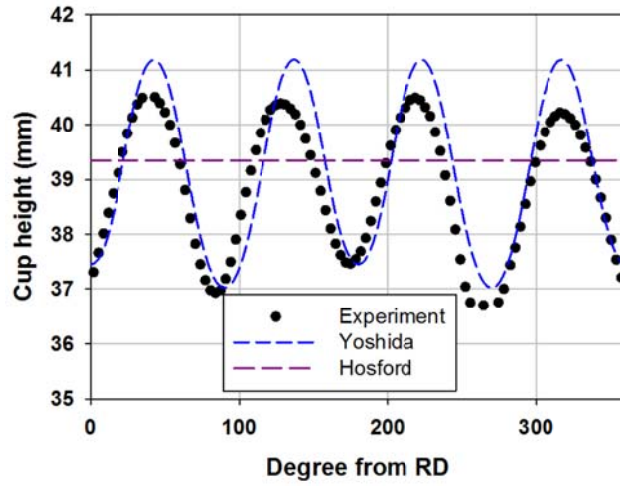


(a)

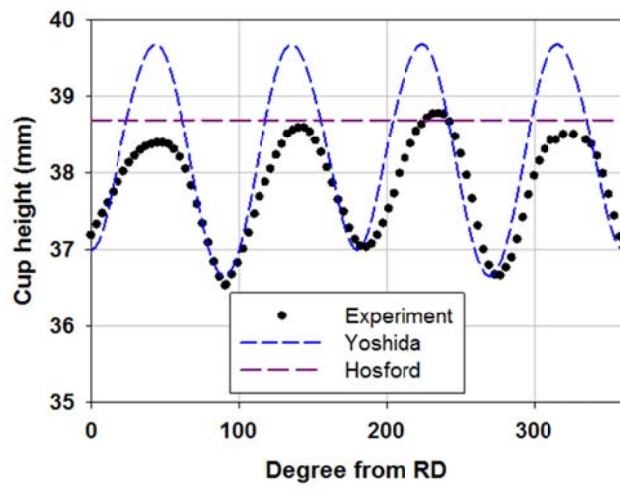


(b)

Figure 57 The experiment and simulation shapes of the successfully completed cups with 102.5 mm diameter: (a) HB780 (b) DP780

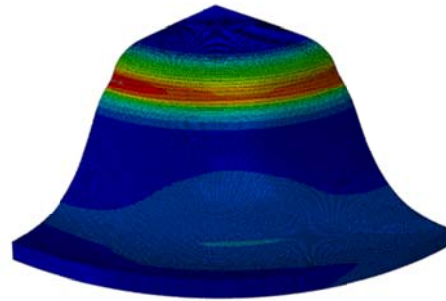


(a)

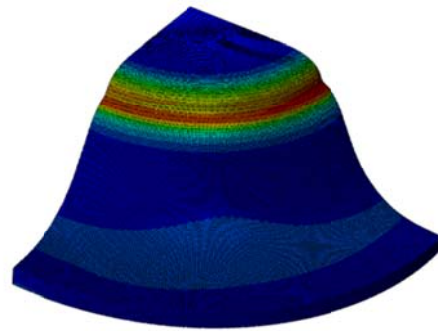


(b)

Figure 58 Comparison of the experiment and simulation earing profiles: (a) HB780 (b) DP780



(a)



(b)

Figure 59 The experiment and simulation shapes of the failed cups with 105.0 mm diameter: (a) HB780 (b) DP780

For application and validation of the newly developed constitutive equation, stress triaxiality and material properties characterized for advanced high strength hot-rolled TWIP steel sheets for failure without strain localization, experiments and numerical simulations were carried out for the circular cup drawing test. The test was performed using the 50 ton double action hydraulic type press as schematically shown in Figure 51. The punch speeds were 20, 100 and 170 mm/min and the blank holding force was 50 kN. The beef tallow was used as a lubricant to reduce the contact friction between the punch and the blank, while a lubricant was not utilized for the blank/die and the blank/holder. The circular cup drawing test specimens with different diameters were prepared by wire cutting. When the diameter of specimens was 112.5 mm, forming was completed without failure for 20 and 100 mm/min, but failure occurred on around the punch radius corner regardless of material directions in case of 115.0 mm diameter as shown in Figure 61 - Figure 64. For 170 mm/min, forming was completed without failure for the 110.0 mm diameter of specimen, but failure occurred in case of 112.5 mm as shown in Figure 65 - Figure 66.

Numerical simulations with properly calibrated hardening, strain rate sensitivity and fracture criterion were carried out for safe and fail of forming. The eight node 3-D continuum element (C3D8R) with the cubic shape of 0.2385 x 0.2385 x 0.2385 mm was utilized in the blank except for the center region with coarse meshes. Thirteen layers were utilized through the thickness of 3.1 mm for blanks. The rigid element (R3D4) was applied for the tools. As for friction, two friction coefficients were assumed: 0.08 for the blank/punch and 0.08 for the blank/die and the blank/holder. Simulations were carried out only for a quarter of the blank considering symmetry.

The simulated results with fracture criterion did not fail for the 112.5, 110.0 mm blank in case of 20, 100 mm/min and 170 mm/min, respectively, complying with experimentally confirmed complete cup drawing without failure, and simulated force-displacement curves also well matched with experiments as shown in Figure 61, Figure 63 and Figure 65. The simulated results showed the failure for the 115.0, 112.5 mm blank, complying with experimentally confirmed cup drawing failure, and simulated force-displacement curves also well matched with experiments as shown in Figure 62, Figure 64 and Figure 66.



(a)

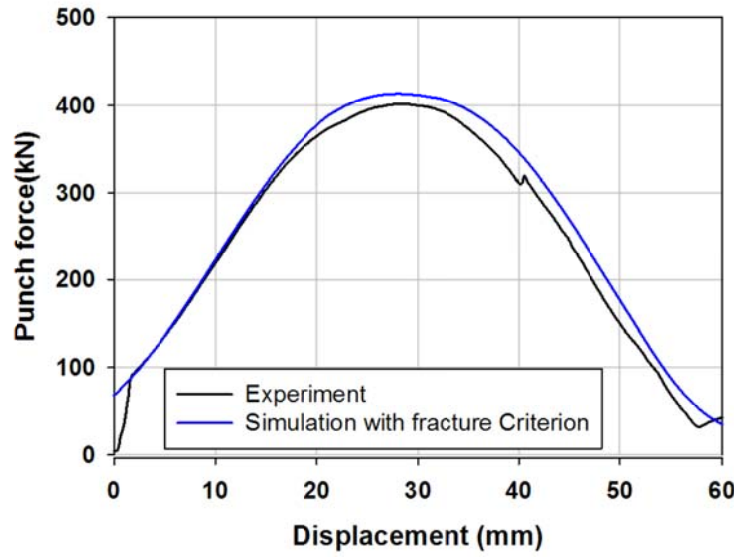


(b)

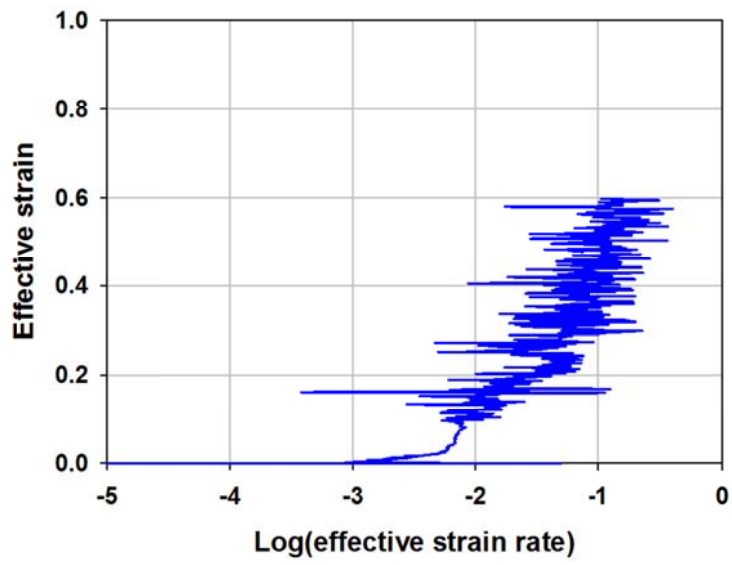


(c)

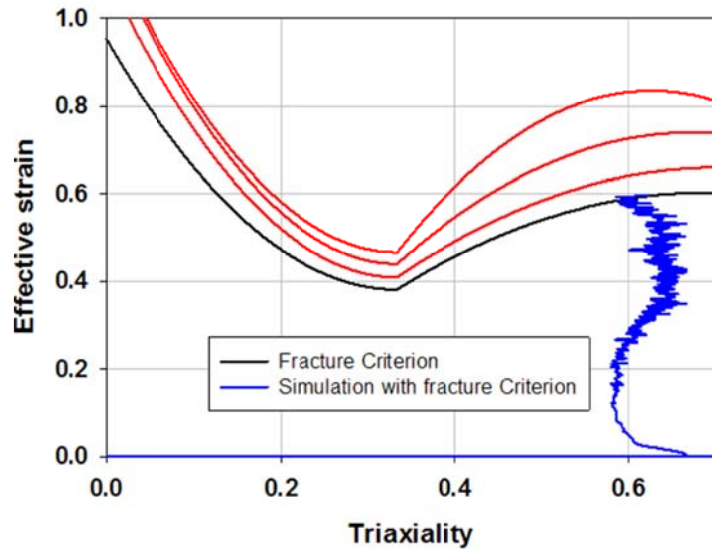
Figure 60 Circular cup drawing test results for TWIP980: (a) 20 mm/min (b) 100 mm/min (c) 170 mm/min



(a)

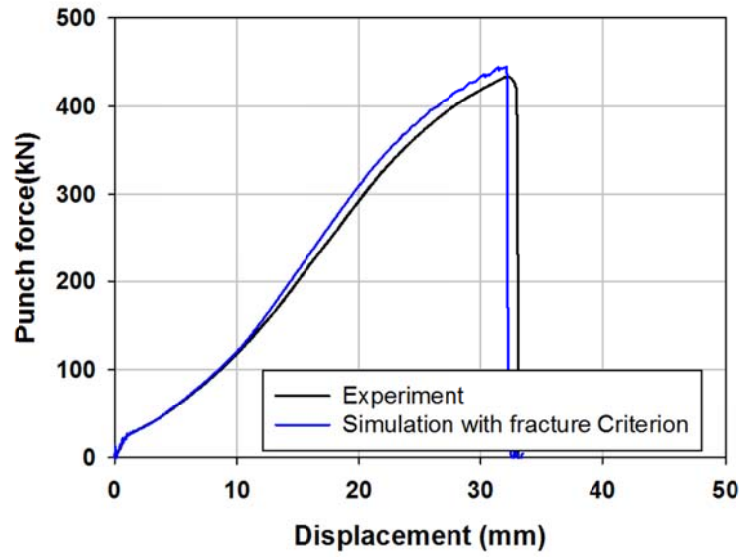


(b)

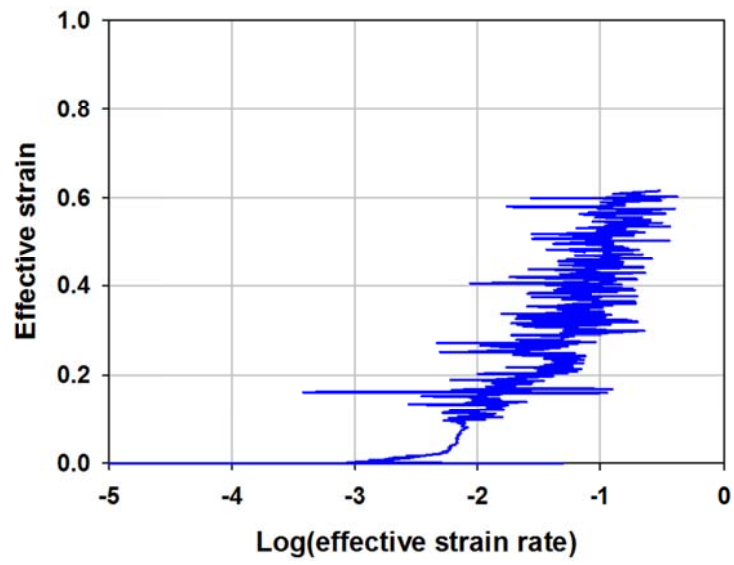


(c)

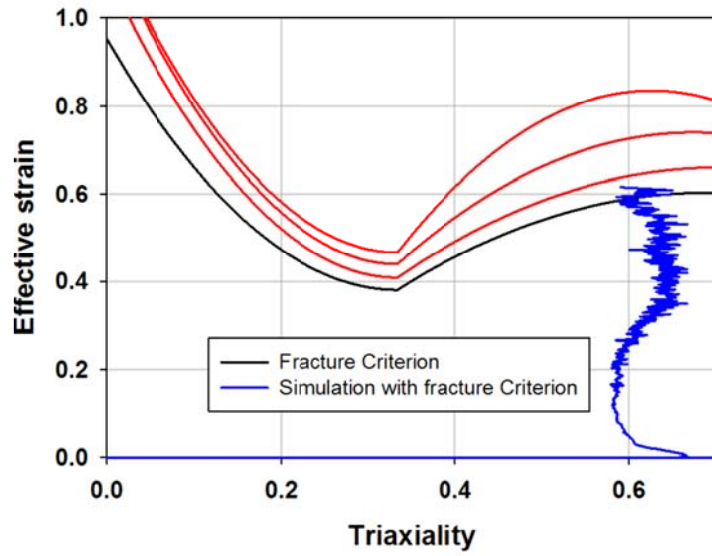
Figure 61 Simulation results for the 112.5 mm diameter with 20 mm/min punch speed:  
 (a) Punch force and displacement (b) Effective strain and effective strain rate in log scale (c) Fracture criterion and deformation history



(a)

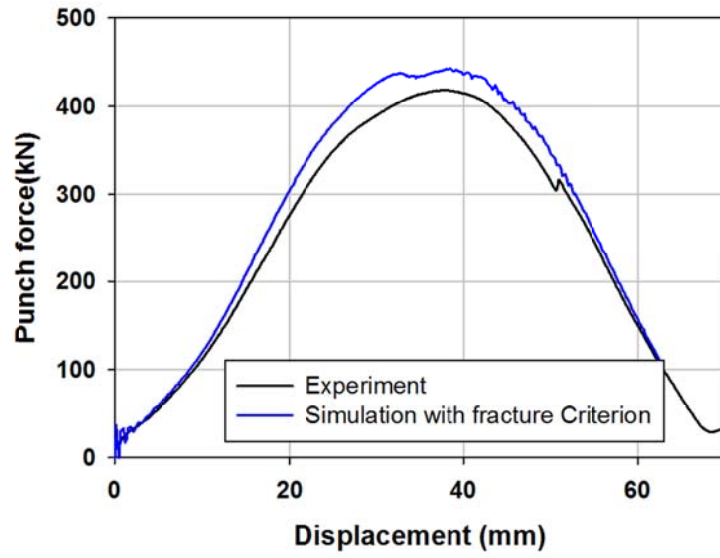


(b)

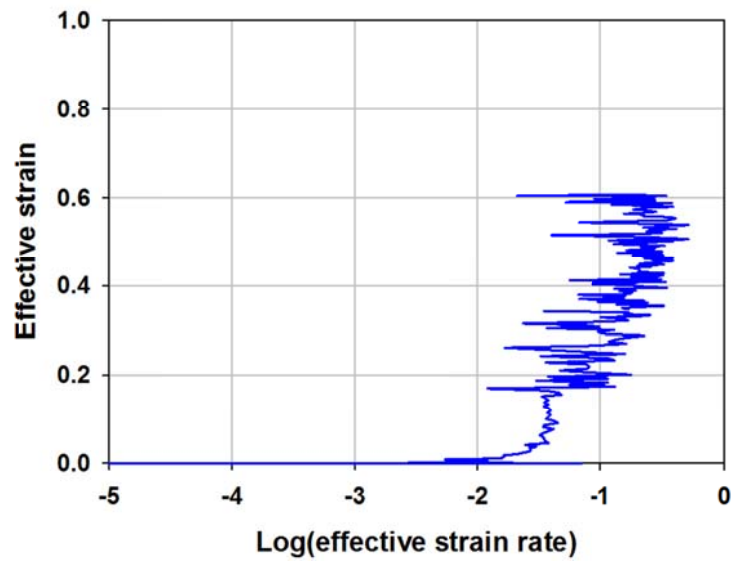


(c)

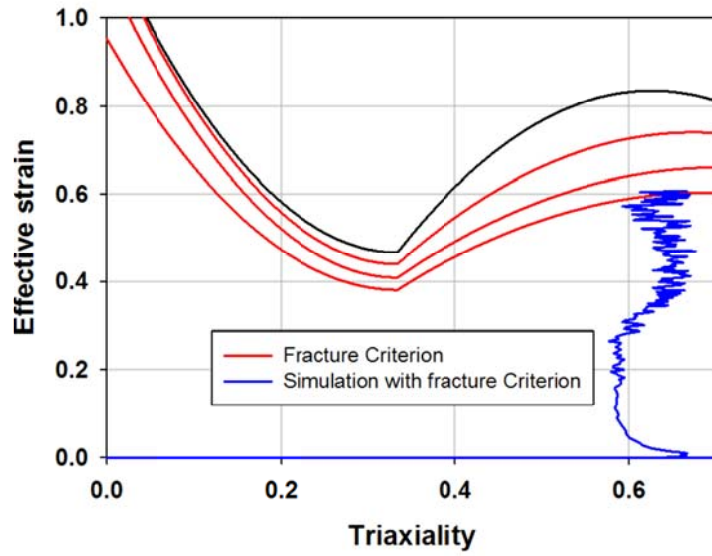
Figure 62 Simulation results for the 115.0 mm diameter with 20 mm/min punch speed:  
 (a) Punch force and displacement (b) Effective strain and effective strain rate in log scale (c) Fracture criterion and deformation history



(a)

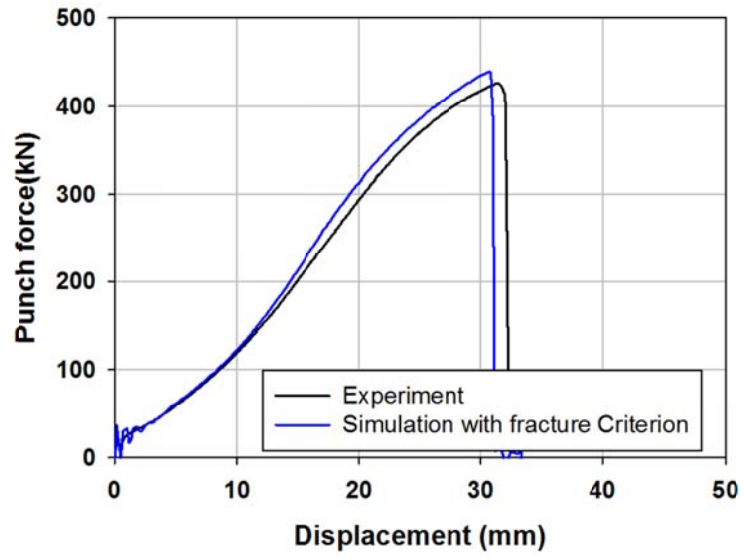


(b)

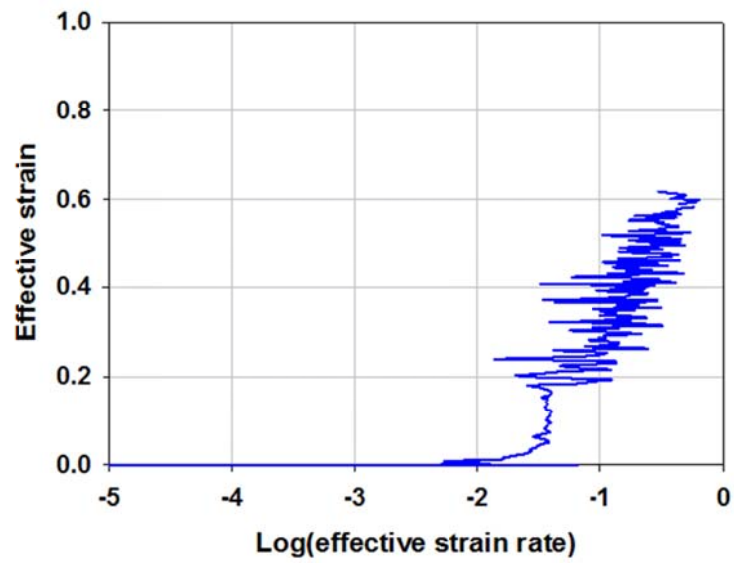


(c)

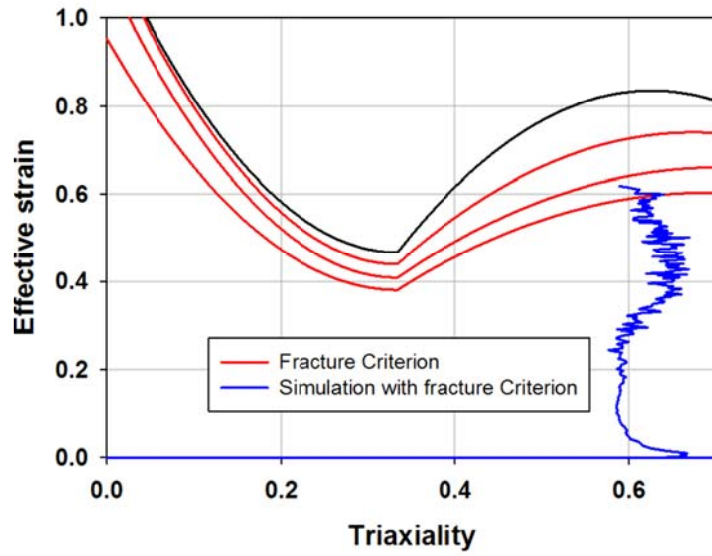
Figure 63 Simulation results for the 112.5 mm diameter with 100 mm/min punch speed: (a) Punch force and displacement (b) Effective strain and effective strain rate in log scale (c) Fracture criterion and deformation history



(a)

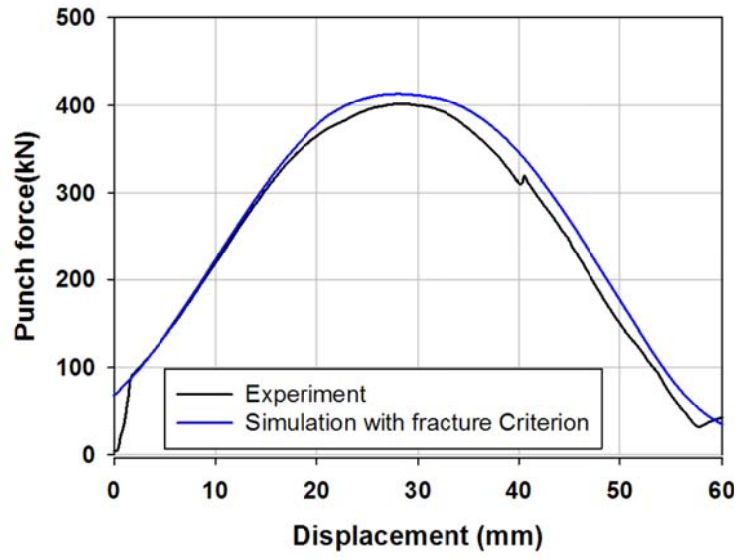


(b)

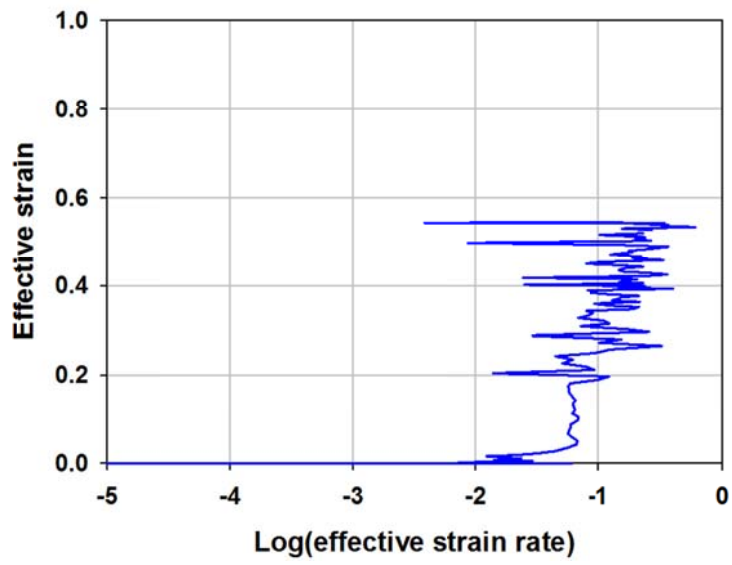


(c)

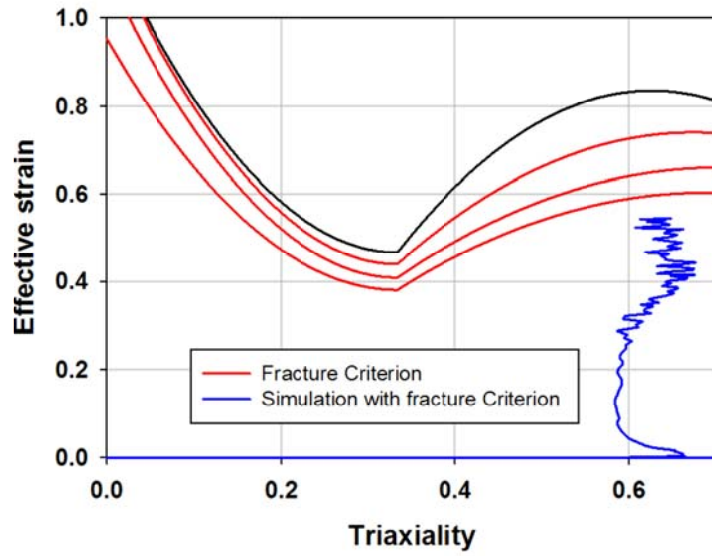
Figure 64 Simulation results for the 115.0 mm diameter with 100 mm/min punch speed: (a) Punch force and displacement (b) Effective strain and effective strain rate in log scale (c) Fracture criterion and deformation history



(a)

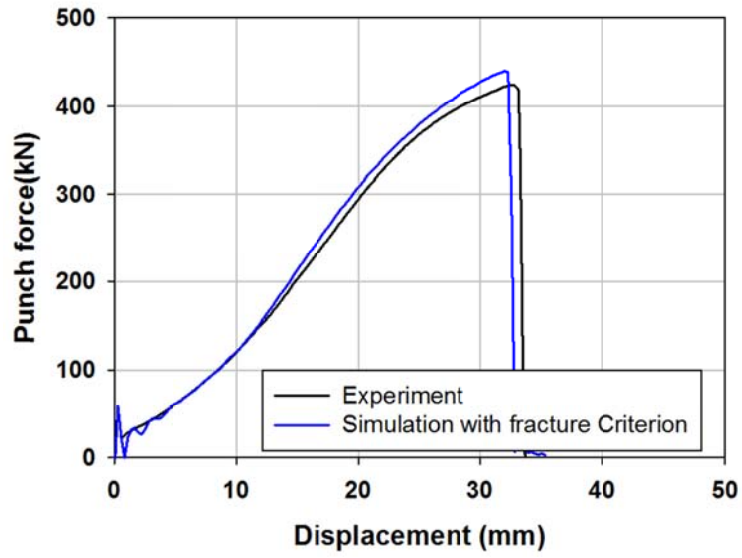


(b)

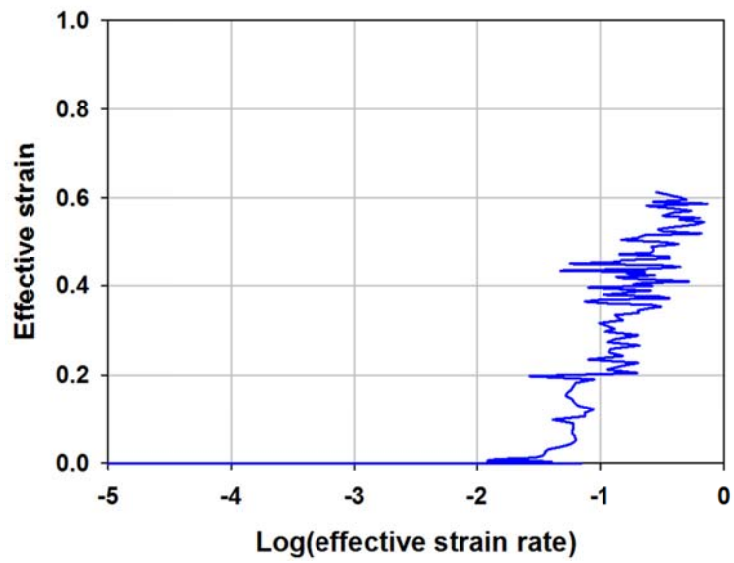


(c)

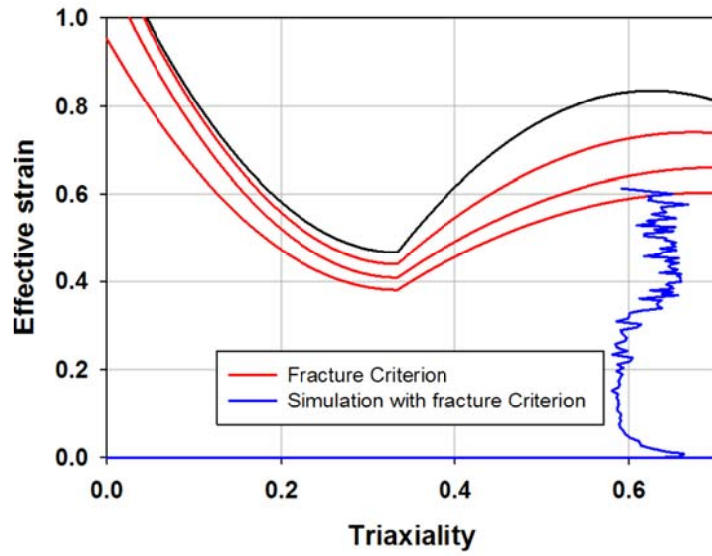
Figure 65 Simulation results for the 110.0 mm diameter with 170 mm/min punch speed: (a) Punch force and displacement (b) Effective strain and effective strain rate in log scale (c) Fracture criterion and deformation history



(a)



(b)



(c)

Figure 66 Simulation results for the 110.0 mm diameter with 170 mm/min punch speed: (a) Punch force and displacement (b) Effective strain and effective strain rate in log scale (c) Fracture criterion and deformation history

## 5. Conclusions

In this work, numerical analysis was performed to predict failure of rather thick advanced high strength hot-rolled steel sheets depending on the existence of strain localization. A numerical procedure to predict the failure with strain localization of advanced high strength hot-rolled steel sheets was developed. The main features of the procedure, which were different from those of the practice commonly applied for rather thin cold-rolled steel sheets, were employing 3-D continuum elements with fine meshes, non-quadratic yield functions such as Yoshida and Hosford yield functions and hardening with its deterioration beyond uniform deformation limit as well as directly monitoring strain localization numerically to determine failure, without employing any forming limit criterion. In these new procedures, 3-D continuum elements were employed mainly because shell elements promote premature strain localization even though forming of the hot-rolled sheets were approximately in the plane stress condition. Since strain localization is significantly affected by three material properties, hardening, strain rate sensitivity and yield surface shape, these were carefully characterized. More precisely, hardening with its deterioration beyond the uniform deformation limit was inversely characterized, considering anisotropy and strain rate sensitivity, based on the simple tension test. As for the yield function shape, non-quadratic isotropic Hosford and anisotropic Yoshida yield functions were applied and their key non-quadratic parameters to determine their shapes, the  $M$  and  $\xi$  values of the Hosford and Yoshida functions, were calibrated based on their simulation performance of the hemispherical dome stretching test: more precisely the simultaneous calibration of hardening deterioration and non-quadratic parameters

based on the simple tension and hemispherical dome stretch tests. Also, disk compression test was conducted to obtain R-value in the balanced biaxial stress mode, the  $R_b$  value, since it affects the failure pattern in the hemispherical dome stretching test for the square blank with the size of 200 mm. In all, the main mechanical properties for strain localization were characterized utilizing the simple tension, disk compression and hemispherical dome stretching test. As for the failure by strain localization, strain localization at the critical element was directly monitored numerically, imitating the experimental procedure based on the grid analysis.

As for the failure without strain localization, the fracture criterion was characterized for TWIP980 with 3.1 mm thickness considering stress triaxiality and strain rate sensitivity. As for mechanical properties, hardening behavior with strain rate sensitivity and Hill 1948 anisotropy yield function were characterized by conducting the simple tension test. To describe the strain rate sensitivity, a new constitutive equation was developed. Also, as for the fracture criterion, it was characterized based on tensile tests with different shape specimens to deal with the wide range of deformation mode. The effective strain of fracture criterion was dependent on stress triaxiality and deformation path. By conducting tensile tests with various strain rates, the strain rate dependency on fracture was examined.

For application and validation, advanced high strength hot-rolled steel sheets, HB780 and DP780 with the thickness of 2.9 mm for failure with strain localization and TWIP980 with the thickness of 3.1mm for failure without strain localization, were considered for the circular cup drawing test. The new procedure well performed to

predict failure in the circular cup drawing test, supporting its applicability for hot-rolled sheet forming analysis.

## Bibliography

- ABAQUS, 2007. User's Manual (Version 6.7). Hibbit, Karlsson & Sorensen Inc., USA.
- Allain, S., Chateau, J.P., Bouaziz, O., 2004. A physical model of the twinning-induced plasticity effect in a high manganese austenitic steel. *Materials Science and Engineering: A* 387–389, 143-147.
- Atkinson, M., 1997. Accurate determination of biaxial stress—strain relationships from hydraulic bulging tests of sheet metals. *International Journal of Mechanical Sciences* 39, 761-769.
- Bai, Y., Wierzbicki, T., 2008. A new model of metal plasticity and fracture with pressure and Lode dependence. *Int J Plasticity* 24, 1071-1096.
- Bai, Y., Wierzbicki, T., 2009. Application of extended Mohr–Coulomb criterion to ductile fracture. *International Journal of Fracture* 161, 1.
- Bao, Y., Wierzbicki, T., 2004. On fracture locus in the equivalent strain and stress triaxiality space. *International Journal of Mechanical Sciences* 46, 81-98.
- Bouaziz, O., Guelton, N., 2001. Modelling of TWIP effect on work-hardening. *Materials Science and Engineering: A* 319–321, 246-249.
- Cazacu, O., Barlat, F., 2001. Generalization of Drucker's yield criterion to orthotropy. *Mathematics and Mechanics of Solids* 6, 613-630.
- Chung, K., Ahn, K., Yoo, D.H., Chung, K.H., Seo, M.H., Park, S.H., 2011a. Formability of TWIP (twinning induced plasticity) automotive sheets. *Int J Plasticity* 27, 52-81.
- Chung, K., Kim, H., Lee, C., 2014a. Forming limit criterion for ductile anisotropic sheets as a material property and its deformation path insensitivity. Part I: Deformation path insensitive formula based on theoretical models. *Int J Plasticity* 58, 3-34.
- Chung, K., Lee, C., Kim, H., 2014b. Forming limit criterion for ductile anisotropic sheets as a material property and its deformation path insensitivity, Part II: Boundary

value problems. *Int J Plasticity* 58, 35-65.

Chung, K., Ma, N., Park, T., Kim, D., Yoo, D., Kim, C., 2011b. A modified damage model for advanced high strength steel sheets. *Int J Plasticity* 27, 1485-1511.

Date, P.P., Padmanabhan, K.A., 1992. On the Formability of 3.15 Mm Thick Low-Carbon Steel Sheets. *Journal of Materials Processing Technology* 35, 165-181.

Drucker, D.C., 1949. The Relation of Experiments to Mathematical Theories of Plasticity. *Journal of applied Mechanics* 16, 349-357.

Ghosh, A., Das, S., Chatterjee, S., 2005. Ultrahigh strength hot rolled microalloyed steel: microstructure and properties. *Materials science and technology* 21, 325-333.

Grässel, O., Krüger, L., Frommeyer, G., Meyer, L.W., 2000. High strength Fe–Mn–(Al, Si) TRIP/TWIP steels development — properties — application. *Int J Plasticity* 16, 1391-1409.

Gurson, A.L., 1977. Continuum Theory of Ductile Rupture by Void Nucleation and Growth: Part I—Yield Criteria and Flow Rules for Porous Ductile Media. *Journal of Engineering Materials and Technology* 99, 2-15.

Gutscher, G., Wu, H.-C., Ngaile, G., Altan, T., 2004. Determination of flow stress for sheet metal forming using the viscous pressure bulge (VPB) test. *Journal of Materials Processing Technology* 146, 1-7.

Hill, R., 1948. A theory of the yielding and plastic flow of anisotropic metals. *Proc. R. Soc. Lond*, 281.

Hosford, W., 1972. A generalized isotropic yield criterion. *Journal of Applied Mechanics* 39, 607-609.

Hosford, W.F., Caddell, R.M., 1983. *Metal forming: mechanics and metallurgy*. Cambridge University Press.

Jahazi, M., Egbali, B., 2000. The influence of hot rolling parameters on the microstructure and mechanical properties of an ultra-high strength steel. *Journal of Materials Processing Technology* 103, 276-279.

Kim, C.G.L., Tae-Ho LEE and Sunghak, 2000. Effects of coiling temperature on microstructure and mechanical properties of high-strength hot-rolled steel plates containing Cu, Cr and Ni. *ISIJ International* 40, 692-698.

- Kim, J.H., Sung, J.H., Piao, K., Wagoner, R.H., 2011. The shear fracture of dual-phase steel. *Int J Plasticity* 27, 1658-1676.
- Kim, W., Koh, Y., Kim, H., Chung, Y., Lee, M., Chung, K., 2016. Formability Evaluation for Hot-rolled HB780 Steel Sheet Based on 3-D Non-quadratic Yield Function (accepted). *Metals and Materials International* 23.
- Lemaitre, J., 1992. *A course on damage mechanics*, Springer-Verlag, Berlin.
- Mateo, A., Llanes, L., Akdut, N., Stolarz, J., Anglada, M., 2003. Anisotropy effects on the fatigue behaviour of rolled duplex stainless steels. *International Journal of Fatigue* 25, 481-488.
- Ogden, R.W., 1972. Large Deformation Isotropic Elasticity - On the Correlation of Theory and Experiment for Incompressible Rubberlike Solids. *Proceedings of the Royal Society of London. Series A, Mathematical and Physical Sciences* 326, 565-584.
- Rodrigues, P.C.M., Pereloma, E.V., Santos, D.B., 2000. Mechanical properties of an HSLA bainitic steel subjected to controlled rolling with accelerated cooling. *Materials Science and Engineering: A* 283, 136-143.
- Seok, D.-Y., Kim, D., Kim, S.-W., Bak, J., Lee, Y.-S., Chung, K., 2015. Fracture criterion for AZ31 Mg alloy plate at elevated temperature. *Metals and Materials International* 21, 54-71.
- Sung, J.H., Kim, J.H., Wagoner, R.H., 2010. A plastic constitutive equation incorporating strain, strain-rate, and temperature. *Int J Plasticity* 26, 1746-1771.
- Tresca, H., 1864. Mémoire sur l'écoulement des corps solides soumis à de fortes pressions. *C.R. Acad. Sci. Paris* 59, 754.
- Tvergaard, V., Needleman, A., 1984. Analysis of the cup-cone fracture in a round tensile bar. *Acta Metallurgica* 32, 157-169.
- Von-Mises, R., 1913. *Mechanik der festen Körper im plastisch deformablen Zustand*. *Gött. Nachr. Math. Phys Klasse* 1, 582-592.
- Wagoner, R.H., 1981. A new description of strain-rate sensitivity. *Scripta Metallurgica* 15, 1135-1137.
- Xu L., B.F., 2008. Disk compression testing and

constitutive modeling of TWIP sheet sample. In:Proceeding of 9th International Conference on Technology of Plasticity, 2312-2317.

Yoshida, F., Hamasaki, H., Uemori, T., 2013. A user-friendly 3D yield function to describe anisotropy of steel sheets. *Int J Plasticity* 45, 119-139.

Young, R., Bird, J., Duncan, J., 1981. An automated hydraulic bulge tester. *Journal of Applied Metalworking* 2, 11-18.

Zhang, P., Guo, Y.-h., Wang, Z.-d., Wang, G.-d., Liu, X.-h., 2010. Texture Evolution in Ferritic Rolled Ti-IF Steel During Cold Rolling. *Journal of Iron and Steel Research, International* 17, 44-58.

Zhao, H., Rama, S., Barber, G., Wang, Z., Wang, X., 2002. Experimental study of deep drawability of hot rolled IF steel. *Journal of Materials Processing Technology* 128, 73-79.

## 초 록

산업 현장의 판재 금속 성형 시 파단의 예측 또는 성형 공정의 최적화를 위하여 유한 요소 해석이 적용되고 있다. 상온 조건의 판재 성형 공정 시, 대부분 판재는 *thinning* 모드에서 변형률 집중을 동반한 파단이 발생한다. 이러한 변형률 집중은 경계 값 문제의 결과이며, 이는 경화 곡선, 항복 함수, 변형률 속도 민감도에 크게 영향을 받는다. 그러나, 몇몇 취성 재료의 경우 변형률을 동반하지 않은 파단이 발생한다. 따라서, 판재의 파단은 이러한 두 가지 성질의 경쟁적 관계에 의해 결정된다. 이 논문의 주요 목적은 파단을 변형률 집중 동반 유무에 따라 초고강도 열연 강판의 성형성을 판단하는 것이다. 변형률 집중을 동반한 경우, 이를 해석하기 위하여 기존 얇은 냉연 강재에 사용되는 방법과는 다른 새로운 유한 요소 해석 방법을 개발하였다. 이러한 방법은 3-D continuum 요소, 비이차 항복함수, 균일 연신 구간 이후의 연화 거동을 고려한 경화곡선을 고려하였고, 또한 성형 한계 조건 없이 변형률 집중을 수치적으로 직접 계산하였다. 물성화를 위하여 일축 인장, 디스크 압축, 반구 돔 장출 시험을 수행하였다. 변형률 집중을 동반하지 않은 파단의 경우, 변형률 속도 민감도와 변형률 속도 및 삼축 응력에 의존한 파단 모델을 고려하였다. 다양한 변형 모드를 위하여 다른 형상의 시편에 대한 인장 시험을 진행하였으며, 변형률 속도 의존성을 고려하기 위하여 다양한 인장 속도로 시험을 진행하고, 이를 통하여 파단 모델을 물성화 하였다. 변형률 집중을 동반한 파단의 경우, HB780과 DP780, 변형률 집중을 동반하지 않은 파단의 경우, TWIP980에 대하여 각각 원형 컵 드로잉 시험을 수행 및 검증하였다.

주요어: 초고강도 열연 강판, 판재 성형성, 비이차 항복함수, 파단 모델  
학 번: 2010-20585